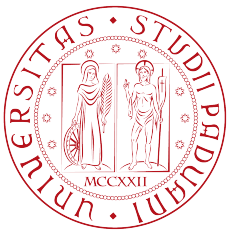

UNIVERSITÀ DEGLI STUDI DI PADOVA

DEPARTMENT OF INFORMATION ENGINEERING

Master Thesis in ELECTRONIC ENGINEERING

STUDY AND IMPLEMENTATION OF A DIGITAL CONTROL OF DUAL-GATED ELECTROLYTE-GATED ORGANIC FIELD-EFFECT TRANSISTORS FOR CELL STIMULATION AND RECORDING

Supervisor
PROF. ANDREA CESTER
UNIVERSITÀ DEGLI STUDI DI PADOVA

Co-supervisors
DOTT. NICOLÒ LAGO
UNIVERSITÀ DEGLI STUDI DI PADOVA
PROF. STEFANO CASALINI
UNIVERSITÀ DEGLI STUDI DI PADOVA

Master's candidate
ANDREA POLLESEL

14 APRIL 2022
ACADEMIC YEAR 2021/2022

"... eppure c'è luce ormai nei miei pensieri, ..."

Abstract

Organic electronics is becoming particularly attractive for biosensing applications, thanks to its advantages such as low-cost materials and fabrication processes, biocompatibility and high sensitivity. Electrolyte-Gated Organic Field Effect Transistors (EGOFETs) have been widely investigated in recent years in this field, due to their peculiar ability to operate at very low voltages, thanks to the high double-layer capacitance given by the interfaces with the electrolyte. However, the contact with oxygen and humidity in acqueous environment is detrimental for the functionality of the transistor, changing its electrical characteristics (threshold voltage shift) and degradating it.

This dissertation is focused on the stabilization of the operating point of the EGOFET, by means of the development of a digital control that exploits an additional gate to control the threshold voltage of the liquid-gated conduction channel. We built up a complete control system that allows to achieve a well-defined output signal for long term measurements. In particular, we targeted extracellular recording and stimulation, by testing different methods to detect and preserve hypothetical action potential signals. All the configurations have been tested by simulations and experimental evidences. The digital control includes autotuning tools to give robustness to the degradation of the devices properties. Several parameters of the control system can be tuned depending on the priorities we want to take into account. With regard to a future implementation with real cells, different coatings for cell seeding have been tried, in order to analyze their effect on the electrical properties. The coated devices stored in air showed a field-effect behaviour for approximately one month.

This thesis is part of a broader project called Project Proactive 2018 "Fully printed organic array of bidirectional reference-less sensors for neuronal interfacing", led by the Principal Investigator Prof. Andrea Cester, in collaboration with:

- *VIMM Veneto Institute of Molecular Medicine*
- *DiSC Dipartimento di Scienze Chimiche, UNIPD*
- *ICMAB Institut de Ciència de Materials de Barcelona*

Sommario

L'elettronica organica sta diventando particolarmente attraente per le applicazioni di biosensing, grazie ai suoi vantaggi come il basso costo dei materiali e dei processi di fabbricazione, la biocompatibilità e l'alta sensibilità. I transistor organici ad effetto di campo con gate elettrolitico (EGOFETs) sono stati ampiamente studiati negli ultimi anni in questo campo, per la loro peculiare abilità di operare a tensioni molto basse, grazie all'elevata capacità di double-layer che si ottiene all'interfaccia con l'elettrolita. Tuttavia, il contatto con l'ossigeno e l'umidità in soluzioni acquose è dannoso per le funzionalità del transistor, modificandone le caratteristiche elettriche (variazione della tensione di soglia) e degradandolo.

Questa tesi si concentra sulla stabilizzazione del punto operativo dell'EGOFET, attraverso lo sviluppo di un controllo digitale che sfrutta un gate aggiuntivo per controllare la tensione di soglia del canale di conduzione liquid-gated. Abbiamo costruito un sistema di controllo completo che permette di ottenere un segnale di uscita ben definito per misure a lungo termine. In particolare, abbiamo mirato alla registrazione e alla stimolazione di segnali extracellulari, testando diversi metodi per rilevare e preservare ipotetici segnali di potenziale d'azione. Tutte le configurazioni sono state testate da simulazioni e prove sperimentali. Il controllo digitale include strumenti di autotuning per fornire robustezza rispetto al degrado delle proprietà dei dispositivi. Diversi parametri del sistema di controllo possono essere tarati a seconda delle priorità che vogliamo prendere in considerazione. Per quanto riguarda una futura implementazione con cellule reali, sono stati provati diversi rivestimenti per la semina delle cellule, al fine di analizzare il loro effetto sulle proprietà elettriche. I dispositivi rivestiti conservati in aria hanno mostrato un comportamento a effetto campo per circa un mese.

Questa tesi fa parte di un progetto più ampio chiamato Project Proactive 2018 "Fully printed organic array of bidirectional reference-less sensors for neuronal interfacing", led by the Principal Investigator Prof. Andrea Cester, in collaborazione con:

- *VIMM Veneto Institute of Molecular Medicine*
- *DiSC Dipartimento di Scienze Chimiche, UNIPD*
- *ICMAB Institut de Ciència de Materials de Barcelona*

Contents

List of Figures

List of Tables

Introduction

Organic electronics has been extensively studied for several decades and in particular in the last twenty years, it has undergone an impressive growth thanks to the developements on the fields of organic light emitting diodes for display applications, organic thin film transistors for flexible circuitry and sensors, and organic photovoltaics for solar energy harvesting. Organic materials offer a lot of advantages, such as low cost, flexibility, easy fabrication, and biocompatibility. They offer the possibility of being tuned into their molecular structure and they can be processed at low temperature. These characteristics, combined with the high sensitivity and amplification properties of the field-effect transistors, make these devices a promising choice for biosensing applications.

One of the most challenging topics in this field is the development of systems capable of interactions with living cells and organisms. The information processing in neural tissue is based on ionic currents flowing through the membrane of neurons which lead to transient potential variations across it. These cellular activities can be recorded by means of a semiconductor in a transistor channel, which is capacitively coupled to the cell medium, acting as a liquid gate. A potential change in the region between the cell and the semiconductor surface, can be monitored from the Field-Effect Transistor (*FET*) current.
Despite organic thin film transistors technology will probably never compete with its inorganic counterpart in terms of performance and stability, this latter have some relevant drawbacks which cannot be neglected in this field. First of all, conventional silicon-based transistors have lower capacitive coupling, which can only be overcome by developing complex nanoscale architectures with prohibitive cost, expecially for disposable sensors. Moreover, they are not quite suitable for interfacing with living systems due to their limited biocompatibility and their issues about long-term stability in an aqueous environment.

From these perspectives, Electrolyte-Gated Organic Field-Effect Transistors (*EGOFET*) are particularly attractive for extracellular recording and stimulation because of their signal amplification, biological compatibility, mechanical and chemical flexibility, as well as the electrical double layer, that forms at the solid-liquid interface enabling fast device response and low voltage operation. Despite these advantages, one important issue that hinders widespread commercial introduction of these devices still remains: when they are operated, their electrical characteristics change with time. The threshold gate voltage at which the transistor switches on gradually shifts towards the applied gate bias voltage (bias-stress effect). This phenomenon results in a dynamic operating point and a distortion on the output signal. The aim of this dissertation is to study and develop a digital control to achieve a well-defined output signal, stabilizing the transistor operative point for general purpose and, specifically, to preserve a hypothetical cell signal (*e.g. action potential*), by exploiting an additional gate to control the threshold voltage of the liquid-gated conduction channel.

Thesis structure

The thesis is organized as follows:

- In chapter 1 the theoretical background needed about organic semiconductors and organic field effect transistors is presented, highlighting the differences with the inorganic counterpart . In particular, electrolyte-gated organic field effect transistors are analyzed in single and dual gate operation.

- In chapter 2 the device fabrication methods and layouts are shown, as well as the characterization procedures and the implemented instruments. Then, main characterization results about the devices are presented.

- In chapter 3 is discussed the development of the digital control used to stabilyze EGOFETs. First, the definition of the problem and the modelization of the system. Then, the details about the PI control implemented.

- In chapter 4, the algorithm and the preliminary simulations are presented. Finally, experimental results are shown and discussed, including the performance of the digital control regards the consistency with simulations, the efficiency of the autotuning implemented, the extracellular recording and the long term stability.

- In chapter 5, conclusions and future perspectives are reported.

Chapter 1

Organic Semiconductors

In organic semiconductors the fundaments of materials structure are organic molecules, which are based on carbon, hydrogen and some sporadic heteroatoms as sulphur, oxygen, and nitrogen. To better understand the semiconductive properties of these molecules and the differences with respect to inorganic semiconductors, it is significant to start to analyze them from the molecular level.

1.1 From carbon atom to molecular solid

Organic molecules are carbon compounds in which the main structure consists of one or more carbon atoms, bounded by a single, double or triple bond, depending on the configuration of each atom.
Carbon atom has six electrons and its standard ground state configuration is the following (Fig.1.1-a):

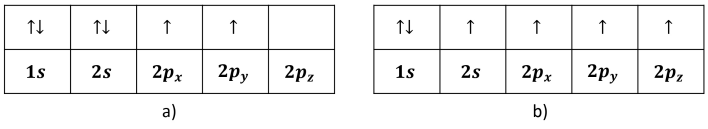

Figure 1.1: *a) Ground state carbon electrons configuration; b) Hybridization of carbon atom.*

However, carbon commonly forms four bonds, due to the fact that orbitals 2s and 2p have similar energy (Fig.1.1-b). The amount of energy needed to promote an electron to the higher orbital 2p is compensated by the energy released from the additional bindings between atoms. This phenomenon, called hybridization, leads to new isoenergetic hybrid orbitals in which the energy of the system is minimized.

In the case of carbon, there can be three kinds of hybridization:

- **sp^3**: four hybrid orbitals, respectively three p combined with one s, arranged in a tetrahedral shape with angles of 109°.
- **sp^2**: three hybrid orbitals made by the combination of p_x, p_y and s, lying in a plane with angles of 120°. $2p_z$ is perpendicular to this plane.
- **sp**: superimposition of s and p_x generates two hybrid orbitals at 180° each other, ortogonal to the remaining p orbitals.

Typically, organic semiconductors are made by double bounded sp^2 hybridization. The stronger bound originated by the superimposition of two sp^2 is called σ, whereas the weaker one, between two p orbitals is defined π. Moreover, the combination of atomic orbital wave functions may be in-phase, leading to constructive interference, or out-of-phase, leading to destructive interference. In-phase combination leads to a lower energy molecular orbital, closer to the nuclei (bonding orbital σ π), whereas the out-of-phase combination leads to a higher energy molecular orbital (antibonding orbitals σ^* π^*).

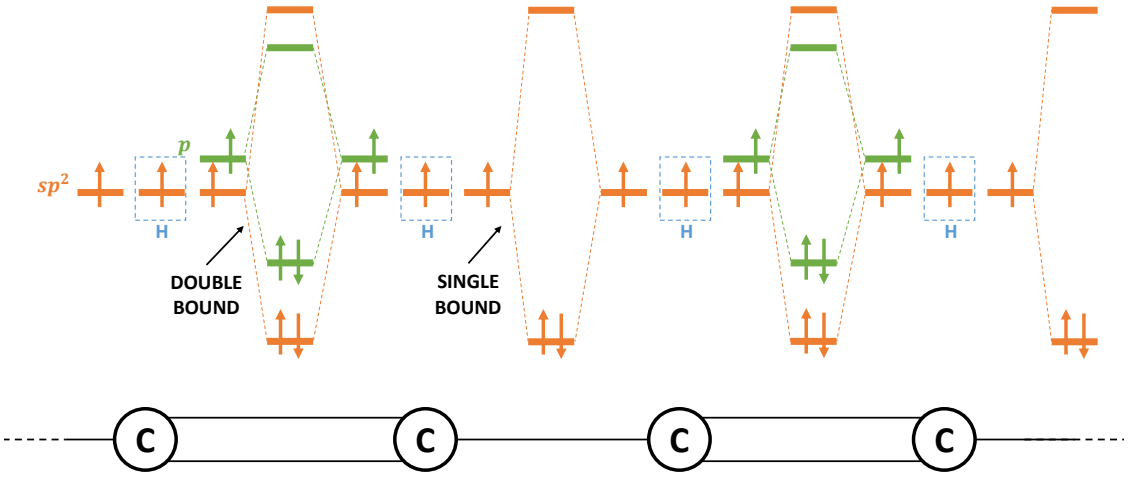

Figure 1.2: *Carbon based conjugated system.*

A conjugated system is a set of atoms bonded together by double and single covalent bonds in an organic molecule. Electrons inside the orbitals of these molecules are delocalized along all the chain or ring (Fig.1.2). Referring to the energy level band diagram, the difference between the highest occupied molecular orbital (HOMO) and the lowest unoccupied molecular orbital (LUMO) defines the energy gap of a conjugated system. The energy gap is the needed energy to excite an electron in the molecule. Lower energy gaps are present when frontiers orbitals are π orbitals. The low distance between π and π^* is

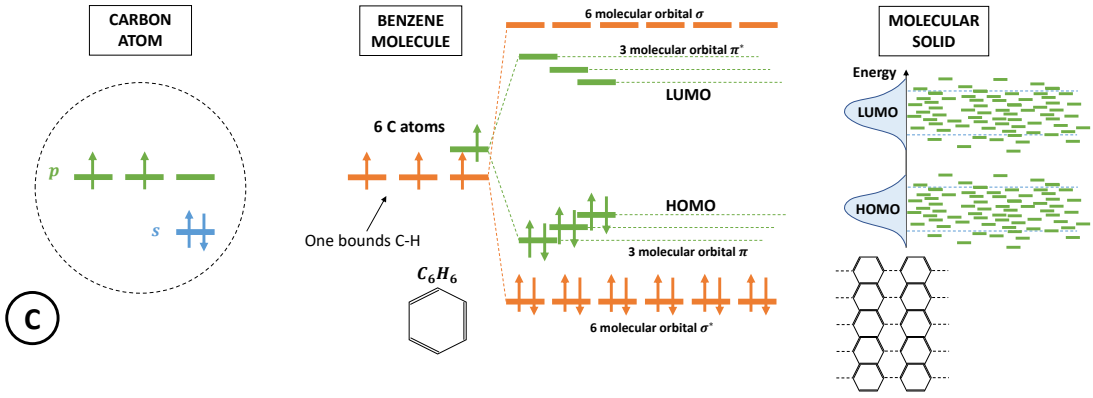

Figure 1.3: *From Carbon atom to molecular solid.*

the key element of the conductive capabilities in organic semiconductors. The amplitude of the levels bands π and π^* depends on the number of Carbon atoms that constitute the molecule. When conjugated molecules form a molecular solid, the interactions between neighbouring molecular orbitals, by means of van der Waals forces, lower the energy gaps. Since organics compounds are amorphous or polycrystalline, the perturbations are not constant and the HOMO and LUMO band gaps are almost randomly localized around average values (Fig.1.3).

1.2 Charge transport

In organic compounds, differently form Silicon based semiconductors, the lattice main elements are groups of molecules or polymers, bounded each other by weak van der Waals forces. Charge transport is led by polarons, which move so slow to deformate the lattice of the corresponding and nearest molecules. Two phenomena contribute to the charge transport:

- **Intramolecular transport:** carrier motion inside a single molecule
- **Intermolecular transport:** carrier motion between different moleculas

The first phenomenon is assimilable to charge transport in crystal lattice structures, with motion similar to a traditional semiconductor. The latter is based on intermolecular hopping transport between localized states. Carriers move following a sequence of jumps through a percolative path of states at different energies, by means of tunnelling effect and phonon emission/absorption. The probability of displacement depends on temperature, barrier height, the distance between the molecules and the occupation of a state. Single electron that

moves from energy level E_1 to E_2 constitutes a density of current equal to:

$$j = q \cdot R \cdot \omega_0 \cdot (P_{1\to2} - P_{2\to1}) \tag{1.2.1}$$

where q is the elemental charge, R is the distance between two energy levels, ω_0 is the frequency factor (rate of collisions inside a potential well) $P_{1\to2}$, $P_{2\to1}$ respectively the probabilities of jump $E_1 \to E_2$, $E_2 \to E_1$. By expressing these probabilities, it can be shown that the current can be approximated to:

$$j(E) \simeq \frac{q^2 R^2 \omega_0 F}{kT} f(E) e^{-2\alpha R - \frac{\Delta E}{kT}} \tag{1.2.2}$$

F Faraday constant, k Boltzmann constant, $f(E) = e^{-\frac{E-E_F}{kT}}$ probability of occupation of energy level E w.r.t. Fermi level E_F, α parameter relater to the barrier height, ΔE average energy gap between consecutive energy levels.

Considering the analogy with the inorganic band model, where $J = qn\mu F$, with an estimation of the mean value of ΔE, the mobility can be described as:

$$\mu = \mu_0 exp\left(-\frac{2\alpha}{\sqrt[3]{N_s}} - \frac{4\sigma^2}{9(kT)^2} \right) \qquad \mu_0 = \frac{qR^2\omega_0}{kT} \tag{1.2.3}$$

In organic semiconductors, the mobility increases with temperature, with the number of free states and with electric field.

Band diagram

Despite inorganic semiconductors, HOMO and LUMO do not have a well defined energy gap where energy levels are not allowed. Nevertheless, valence E_V and conduction E_C band can be established with regard to the mobility, since it depends on the states distribution $g(E)$.

$$g(E) = \frac{N_s}{\sqrt{2\pi\sigma}} e^{-\frac{(E-E_{MAX})^2}{2\sigma^2}} \tag{1.2.4}$$

where N_s is the density of states, E_{MAX} is the value of energy at which the density is higher and σ is the distribution amplitude.
Energy levels closer to HOMO and LUMO are at high mobility, respectively for holes and electrons, due to the high density of states denoted by the gaussian distribution. Towards the middle of the energy gap, the density is smaller, lowering the mobility. E_V and E_C can be defined as mobility threshold energy limits, by separating energy states in which carriers are free to move, from energy levels that act as trapping levels.

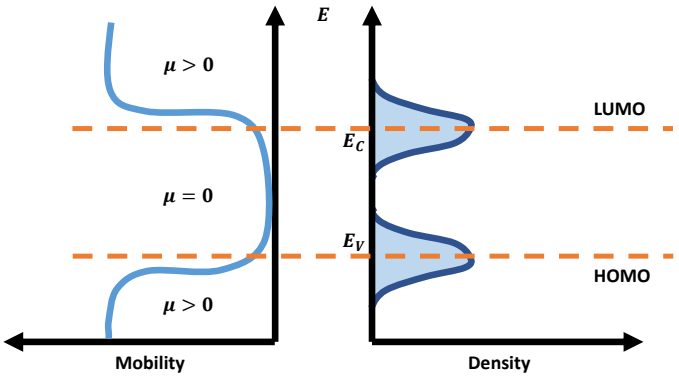

Figure 1.4: *Band diagram and mobility thresholds.*

1.3 MIM junctions and current in organic film

In organic semiconductors, the potential profile is mainly determined by defects distribution D_T, differently from inorganics, where ionized dopants are the key element. Considering a metal-semiconductor interface, the potential profile can be described as:

$$\Phi(x) = \Phi_i e^{-\frac{x}{\lambda}} \qquad \lambda = \sqrt{\frac{\varepsilon}{q^2 D_T}} \tag{1.3.1}$$

Assuming defects distribution of $D_T \sim 10^{17} defects/cm^2 eV$, with $\varepsilon = 3\varepsilon_0$ dielectric constant of the material, it results $\lambda = 40nm$, that is the typical value of thickness in organic semiconductors. Since the perturbation occurs along all the film, it is more realistic to consider the potential profile along a metal-insulator-metal system (*MIM*), where the OSC acts as an insulator:

$$\Phi(x) = \Phi_i \frac{\cosh\left(\frac{x}{\lambda}\right)}{\cosh\left(\frac{t_s}{2\lambda}\right)} \tag{1.3.2}$$

where t_s is the film thickness and $x = 0$ is in the middle of the system. The effect of the metal electrodes is along all the film, with a minimum band bending, acting as a doping that imposes the Fermi level.

Considering a MIM system with a difference of potential applied between the electrodes, the electric current that can be measured consists of two mechanisms:

- **Charge injection:**

  if the potential barrier is sufficiently high ($e.g. 0.3eV$), the charge injection is limited and it is described by tunnelling and thermionic emission.

Potential barriers lower than $0.3eV$ are considered ohmic contacts and the current is limited by semiconductor properties.

- **Charge transport between contacts:**

  since organic semiconductors are comparable with insulators, the main contribute to the current is given by injected carriers and the typical conduction regime is *Space Charge Limited* (SCL). Considering negligible intrinsic carriers and defects, with no doping and mobility indipendent from electric field, it is possible to get the Mott-Gurney current equation:

$$J = \frac{9}{8}\mu\varepsilon\frac{V_D^2}{L^3} \tag{1.3.3}$$

  where V_D is the applied voltage. If surface defects are taken into account, the current is *Trapped Charge Limited* (TCL) and the equation becomes:

$$J = \frac{9}{8}\frac{\theta}{1+\theta}\mu\varepsilon\frac{V_D^2}{L^3} \tag{1.3.4}$$

  where θ represents the surface defects and lowers the effective mobility. With deeper defects, the equation depends on the defects distribution D_T.

1.4 MOSFET and OFET

Field-effect transistors (*FET*) are key electronic components used for signal amplification and logical applications. Devices are based on three terminals: source (S), drain (D) and gate (G) on a substrate of a semiconductor material (e.g. silicon). In *MOSFET* devices (Metal-Oxide-Semiconductor-Field-Effect-Transistor), a thin layer of silicon dioxide insulates the gate electrode from the semiconductor. The operating principle is based on modulation of the current between source and drain by applying a voltage to the gate. Different regimes of conduction are possible, according to the bias applied and the threshold voltage of the transistor. Their high sensitivity results optimal in biosensing applications, however their costs in terms of fabrication and miniaturization lower their appeal in this market. Organic Field Effect Transistors (*OFETs*), can overcome this issues, since they are characterised by an organic semiconductor as the active layer, with simpler fabrication processes. Moreover, their organic compositon enhances biological compatibility and mechanical and chemical flexibility. Typical configurations are presented in Fig.1.5.

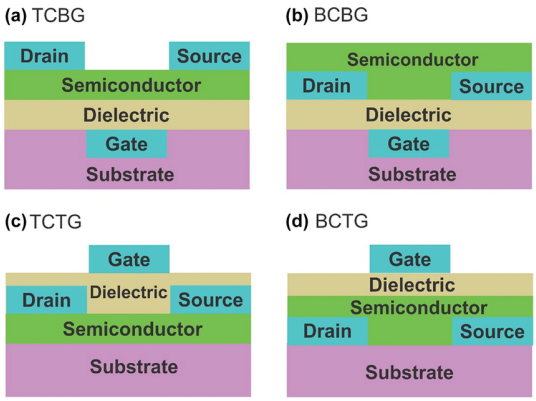

Figure 1.5: *a) Top Contact Bottom Gate b) Bottom Contact Bottom Gate c) Top Contact Top Gate d) Bottom Contact Top Gate.*

The main difference with MOSFETs is in the working mechanism of the conduction. In fact, they operate in inversion mode, with p-channel in n-type semiconductor, whereas the OFETs operate in accumulation mode. In a p-type semiconductor, positive charges are attracted to the insulator interface, in the channel region, when a negative gate bias is applied. More precisely, considering MIS interface, when a voltage $|V_G| > |V_{FB}|$ is applied, (V_{FB} is the flat band voltage of the interface), the bands start to bend. The insulator presents a linear voltage drop. In the semiconductor, close to the interface with insulator, the bands bend below the Fermi level, accumulating fixed charges trapped into defects. Increasing the value of V_G, defects will be filled and the free carriers will grow predominantly w.r.t. the fixed charge. The equivalence between the free charge and the fixed charge can be used to get the threshold voltage of the transistor:

$$V_{th} = V_{FB} + \Phi_{C/V}\left(1 + \frac{C_s}{C_i}\right) \tag{1.4.1}$$

where $\Phi_{C/V}$ is the potential at the interface under conditions of accumulation in conduction/valence band, C_s is the capacitance related to the fixed charge region and C_i is the insulator capacitance.
Another difference w.r.t. the inorganic devices is in the principle of modulation of the current. In fact, if we consider n as the number of free carriers and n_T as the trapped carriers, the average mobility can be defined as:

$$\mu = \mu_0 \frac{1}{1 + \frac{n_T}{n}} \tag{1.4.2}$$

Therefore, the gate modulation on the drain-to-source current has the effect to modulate the mobility of the carriers. This relationship can be written as:

$$\mu_{FET} = k\left(V_G - V_{th}\right)^{\alpha} = \mu_0\left(\frac{Q_n}{C_i V_0}\right)^{\alpha} \qquad k = \frac{\mu_0}{V_0^{\alpha}} \tag{1.4.3}$$

where V_0 and α are esperimental values, Q_n is the free charge.

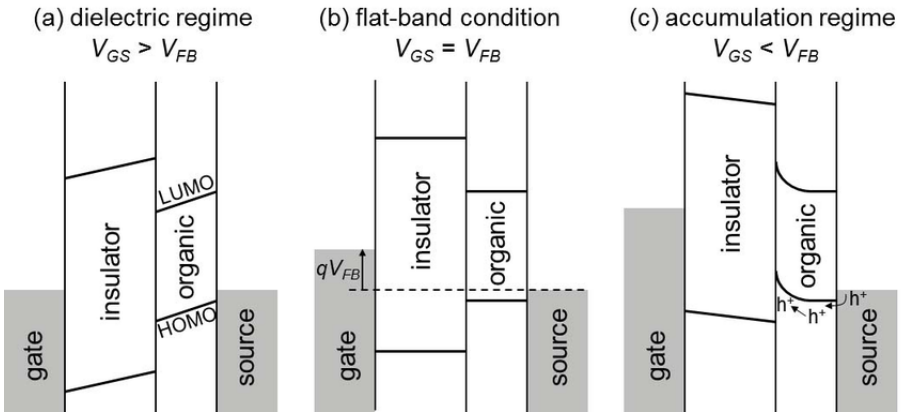

Figure 1.6: *Band diagram OFET p-type.*

The current-voltage relationship can be derived obtaining the following equations (with the negative sign for p-type):

$$I_{DS} = \begin{cases} \frac{C_i \mu_0}{(\alpha+2)V_0^{\alpha}} \frac{W}{L} \left[(V_{GS} - V_{th})^{\alpha+2} - (V_{GS} - V_{th} - V_{DS})^{\alpha+2} \right] & \textit{Linear regime} \\ \frac{C_i \mu_0}{(\alpha+2)V_0^{\alpha}} \frac{W}{L} (V_{GS} - V_{th})^{\alpha+2} & \textit{Saturation regime} \end{cases} \tag{1.4.4}$$

where W and L are the channel width and length, while V_{DS} is the voltage applied from drain to source and C_i is the gate capacitance.

1.5 EGOFET

One of the main constraints in biological application is the need to operate at low voltages and in aqueous environment. Electrolyte-Gated Organic Field Effect Transistor (*EGOFET*) substitutes the dielectric material with an electrolyte, that can be either liquid or solid. This new configuration strongly increases the capacitance at the semiconductor interface, that allows a huge reduction of the operating voltage below $1V$. The imposition of a bias voltage to the gate electrode generates a redistribution of the ions within the liquid electrolyte. In the case of p-channel EGOFET, cations are attracted to the gate/electrolyte interface, while anions accumulate on the semiconductor/electrolyte one. This phenomenon generates an electrical double layer (EDL) on both interfaces. Holes accumulate in a thin layer of the organic semiconductor in order to compensate the negative charges, creating the conductive channel. As the mobility of ions is usually lower than electrons one, the formation of the EDL takes few milliseconds. The switching speed may be lowered in case of high gate voltage. In this case may occur electrochemical doping, in which ions from the electrolyte penetrate in the semiconductor, varying the electrical properties and the robustness of the device. In EGOFET structure, the electrical double layers are considered as two capacitances in series, as shown in Fig.1.7.

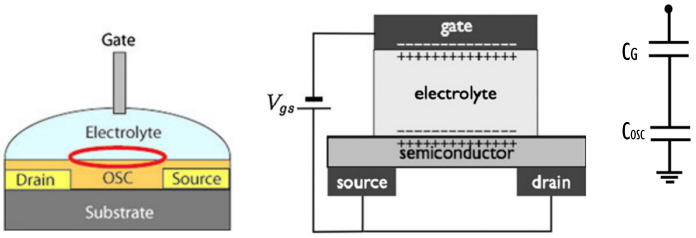

Figure 1.7: *EGOFET architecture and electrical double layers. The red circle indicates the interface involved in the detection.*

Biosening applications can be performed exploiting the high sensitivity of this device. The organic surface can be functionalized to sense specific elements, analyzing the variation on mobility, capacitances and voltages of interest. Particular coatings can be used to cell seeding, in order to record the extracellular activity, seen as potential variation across the electrolyte gate. The phase that follows the sensing is the transduction, in which the change of the potential at the interface entails a variation in the channel conductivity and thus in the channel current.

The main drawback of aqueous media is the device degradation and instability due to the direct contact with oxygen and humidity. Different architectures can be exploited to overcome this issue, by an additional gate that is separated from the channel by a metal-oxide gate dielectric. Moreover, in extracellular sensing applications, the secondary gate may be used to carry out direct stimulation of the cell, without need of invasive methods, such as patch clamp.

The current-voltage relationship for both Back-Gate and Top-Gate configurations can be described by the same equations presented before, that can be rewritten in the form of a classic p-type field-effect transistor:

$$I_{DS} = \begin{cases} -\frac{W}{L} C_i \mu_{FET} \left[(V_{GS} - V_{th}) V_{DS} - \frac{V_{DS}^2}{2} \right] & \textit{Linear regime} \\ -\frac{1}{2} \frac{W}{L} C_i \mu_{FET} (V_{GS} - V_{th})^2 & \textit{Saturation regime} \end{cases} \tag{1.5.1}$$

where $\frac{W}{L}$ is the form factor of the transistor, μ_{FET} is the field-effect mobility, V_{th} is the transistor threshold voltage, V_{DS} is the drain-to-source voltage, V_{GS} is the gate-to-source voltage and C_i is the gate capacitance (either back gate or top gate).

When operating in dual-gate in saturation regime, the control of the back gate on the threshold voltage depends on the capacitances ratio $\frac{C_S}{C_{TG}}$, where $C_S = \left(\frac{1}{C_{BG}} + \frac{1}{C_{OSC}}\right)^{-1}$ is the equivalent in-series capacitance formed by the coupling of the bottom-gate (C_{BG}) and the semiconductor (C_{OSC}) capacitances.

This linear relation is represented by the following equation:

$$V_{th} = V_{th0} - \frac{C_S}{C_{TG}} V_{BG} \tag{1.5.2}$$

with V_{th0} threshold voltage at $V_{BG} = 0V$.

Chapter 2

Materials, methods and characterization

In this section the fabrication method and materials of the EGOFETs involved are discussed. Two layouts are presented, for the coating tests and the digital control experiments, respectively. Then, the characterization procedure and results are shown.

2.1 Devices fabrication

2.1.1 Substrate

The starting substrate is silicon ($p+$ doped, $\sigma = 0.005 - 0.02\Omega cm$), whose thickness is $525(\pm 25)\mu m$, which presents $200nm$ thermally-grown SiO_2 . The photolithography starts from a positive photoresist spin-coating (Shipley S1813), exposed to light by using the Micro-Writer ML3, then developed by Shipley Microposit MF-319. The Cr/Au electrodes ($5nm/40nm$ thick) were evaporated by means of the Metal Evaporator System Auto 306. The final treatment was performed by using acetone.

2.1.2 Organic semiconductor

The substrates, activated by using UV Ozone cleaner for 25 min, were immersed in a solution of 2,3,4,5,6-pentafluorothiophenol ($PFBT$, $2\mu L/mL$ in isopropanol) for 15 minutes. Then, they were rinsed with isopropanol and dried with nitrogen. A thick layer of dextran (drop-casted from a solution $10mg/mL$) was deposited on the areas of the coplanar gate electrode and contacts. The organic semiconductor (OSC) was deposited by means of Bar-Assisted Meniscus Shearing (BAMS).

A blend of 2,8-Difluoro-5,11-bis(triethylsilylethynyl)anthradithiophene ($diF\text{-}TES\text{-}ADT$) and polystyrene ($Mw = 10000 g/mol$) was dissolved in chlorobenzene 2%wt with a ratio 4:1 ($diF\text{-}TES\text{-}ADT : PS$). $diF\text{-}TES\text{-}ADT$ is a benchmark organic small semiconductor molecule (Fig.2.1), which has shown excellent properties when employed in organic field-effect transistors (OFETs), namely high field-effect mobility and low threshold voltage. Blends of diF-TES-ADT with polystyrene (PS) deposited by BAMS have been reported to give rise to devices exhibiting high performance and stability with potential in sensing and bioapplications. The solution was deposited at $10 mm/s$ at $105°C$.

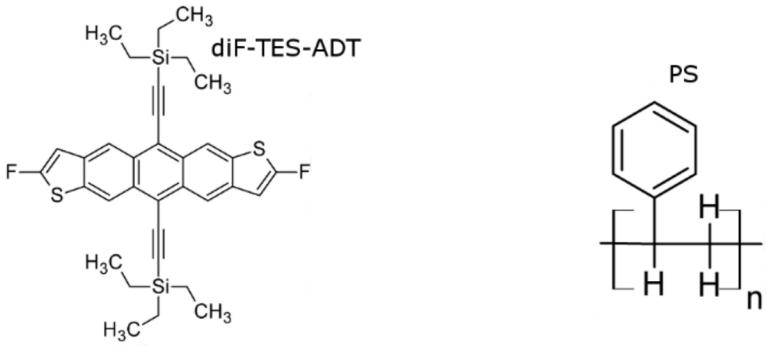

Figure 2.1: *diF-TES-ADT and PS.*

Finally, the dextran coating has been removed immerging the silicon substrate in bi-distilled water. Homogeneity, thickness, anisotropy, crystallinity and vertical phase separation of the semiconducting thin-film have been accurately verified. The vertical phase separation between $diF\text{-}TES\text{-}ADT$ and PS leads to most of PS being sandwiched between the SiO_2 and the OSC. The back gate capacitance is given by the in-series capacitances related to the SiO_2 (200nm thick) and PS (10nm thick), resulting in an overall capacitance around $16 nF/cm^2$.

2.1.3 Layout

Interdigitated lateral gate layout

The layout used in digital control tests is depicted in Fig.2.2, with the source and drain contacts interdigitated each other, in order to increase the area of the channel, and the lateral top-gate located at a distance of 4mm.

Table 2.1: Interdigitated lateral gate details.

Details of the layout			
$Electrode\ gate\ area$	$3x3mm^2$	$Channel - gate\ ratio$	1 : 1000
$Electrode\ width\ (fingers)$	30μm	$Number\ of\ fingers$	12
$Channel\ length\ (L)$	30μm	$Channel\ width\ (W)$	8476μm
$Distance\ PADs - IDE$	3.2mm	$Distance\ PAD - Gate\ electrode$	2.1mm

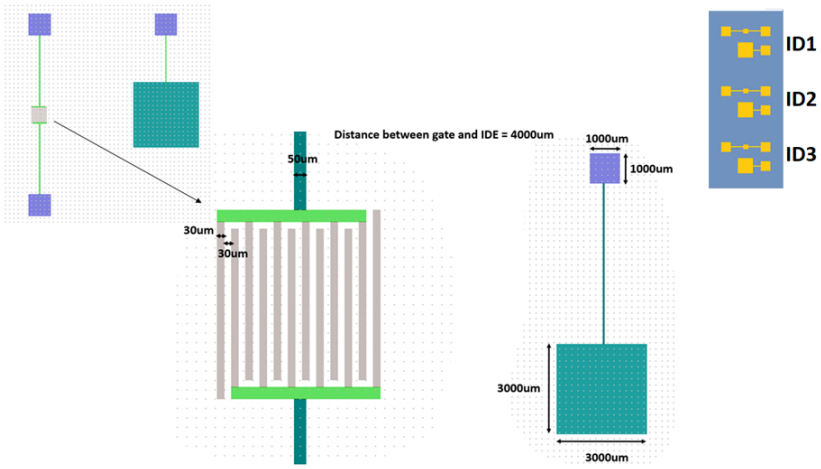

Figure 2.2: *Interdigitated lateral gate layout*

Corbino layout

Another layout has been developed in two configurations (Fig.2.3), in order to minimize transistor footprint and enhance its stability, with circular shape electrodes for source and drain. These devices have been used to test the impact of coatings and the degradation of the device with time (in Fig.2.3 on the right, in different concentrations of Matrigel with extracellular solution).

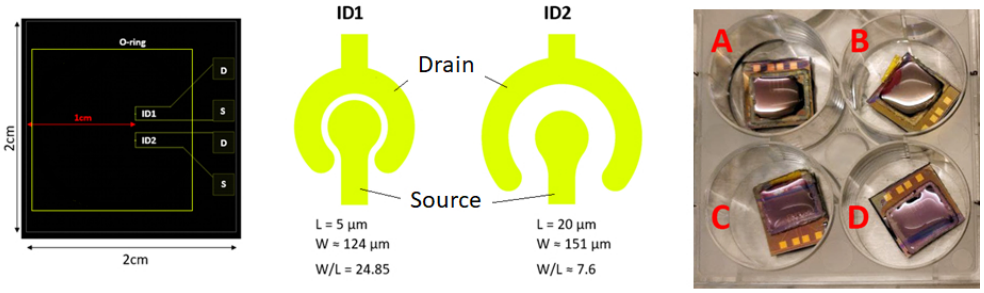

Figure 2.3: *Corbino layout.*

Table 2.2: Corbino details.

Details of the layout			
ID1		ID2	
Channel length (L)	$5\mu m$	*Channel width* (L)	$20\mu m$
Channel length (W)	$124\mu m$	*Channel width* (W)	$151\mu m$

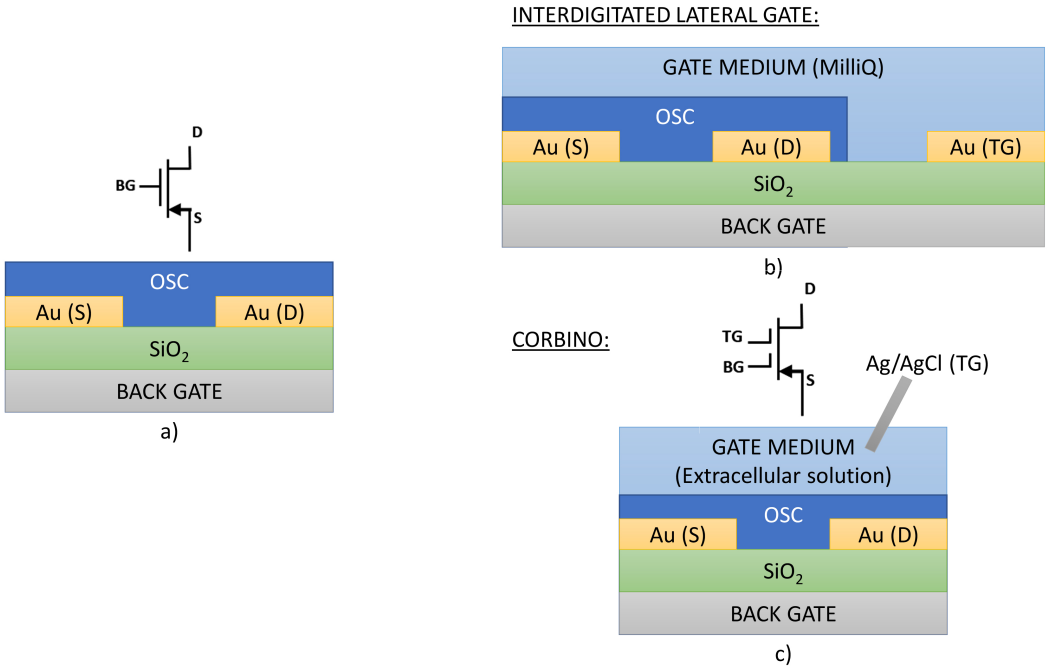

Figure 2.4: *a)Back Gate configuration b) Top Gate configuration (interdigitated lateral gate) c) Top Gate configuration (Corbino).*

2.1.4 Coatings

Poly-L-lysine

Poly-L-lysine (*PLL*) is a synthetic polypeptide of naturally occurring amino acid l-lysine. It represents a polyelectrolyte comprising amino groups that can be easily protonated allowing them to be rendered positively charged for a broad pH range. Therefore, PLL is often used for functionalization of solid substrates in order to promote an efficient attachment of bioactive molecules such as cells.

Matrigel

Matrigel is a blend of extracellular matrix proteins derived from murine tumor cells, an animal-derived extracellular matrix (*ECM*) proteins adsorbed to the culture substrata. It is extracted from EngelbrethHolmSwarm mouse sarcomas that contains not only basement membrane components laminin, collagen IV, heparin sulfate proteoglycans and entactin but also matrix degrading enzymes, their inhibitors, and numerous growth factors. It is exploited for cell adhesion on semiconductors.

2.2 Characterization procedures

Electrical characterizations are executed to investigate the functionality and the performance of the individual devices, before and after the experiments. The electrical characterizations and control tests for the interdigitated lateral gate devices have been performed in dark by using using an Agilent B1500 parameter analyzer driven by Desktop Computer by using Matlab®, with two high-power and two high-sensitive source measurement units (*SMUs*). The measurement set-up is synthesized in Fig.2.5. The electrical characterizations for the circular devices have been carried out by using a home-made custom acquisition system, equipped with three high-speed SMUs ($T_{s_{min}} = 20\mu s$).

2.2.1 Back-Gate

Concerning the Back-Gate measurements without gate liquid medium (Fig.2.4 a)) on interdigitated lateral gate devices:

- Quasi-Static $QS - I_{DS}V_{DS}$ output characteristics were taken by scanning V_{DS} from $0V$ to $15V$ with a constant V_{BG} respectively equal to $5V$, $10V$, $15V$ and a scan rate of $150mV/sample$;
- $QS - I_{DS}V_{BG}$ transfer characteristics were taken by scanning V_{BG} from $5V$ to $15V$ with constant $V_{DS} = 1V$ (linear regime) and $V_{DS} = 15V$ (saturation regime), with a scan rate of $200mV/sample$.

2.2.2 Top-Gate

Regarding the Top-Gate measurements on interdigitated lateral gate devices, whereas the back gate is fixed to $0V$ (Fig.2.4 b)) and the gate medium is deionized water:

- $QS - I_{DS}V_{DS}$ output characteristics were taken by scanning V_{DS} from $0V$ to $0.5V$ (higher voltages may lead to redox reactions) with a constant V_{TG} respectively equal to $0.3V$ and $0.5V$ and a scan rate of $5mV/sample$;
- $QS - I_{DS}V_{TG}$ transfer characteristics were taken by scanning V_{TG} from $0.2V$ to $0.5V$ with constant $V_{DS} = 0.05V$ (linear regime) and $V_{DS} = 0.5V$ (saturation regime), with a scan rate of $7mV/sample$.

Concerning the Top-Gate measurements on Corbino layout devices with extracellular solution (Fig.2.4 c)):

- $QS - I_{DS}V_{DS}$ output characteristics were taken by scanning V_{DS} from $0V$ to $0.5V$ with a constant V_{TG} respectively equal to $0.4V$ and $0.5V$ and a scan rate of $5mV/sample$;

- $QS - I_{DS}V_{TG}$ transfer characteristics were taken by scanning V_{TG} from $-0.2V$ to $0.5V$ with constant $V_{DS} = 0.5V$ and a scan rate of $3mV/sample$.
- Current vs time (I-Time) characteristics were taken applying a voltage step on Top-Gate from $0V$ to $-0.5V$ (turn on) and from $-0.5V$ to $0V$ (turn off), to study its capacitive coupling and turn on/off times. V_{DS} was set equal to $0V$, $-0.5V$ (for the decoupling of the FET contribution).

Drain and source have been tested both in inner and outer configuration to analyse the best performances of the circular electrodes.

2.2.3 Dual-Gate

Dual-gate characterizations have been carried out as follows:

- $QS - I_{DS}V_{TG}$ transfer characteristics were taken by scanning V_{TG} from $0.2V$ to $0.5V$ with constant $V_{DS} = 0.5V$ and a scan rate of $7mV/sample$. Each transfer curve was repeated at a different value of V_{BG}, from $0V$ to $50V$ at step of $5V$.
- Current vs time (I-Time) characteristics were taken with $V_{TG} = -0.5V$ and $V_{DS} = -0.5V$. The Back-Gate voltage was initially set to $5V$ and then controlled by the developed digital control, according to the recorded values of the current, with $T_s \simeq 200ms$.

Concerning the Dual-Gate measurements on Corbino layout devices:

- Current vs time (I-Time) characteristics were taken applying a voltage step on Back-Gate from $0V$ to $-0.5V$, to study its capacitive coupling. V_{DS} was set equal to $0V$, $-0.5V$ (for the decoupling of the FET contribution) and $0.5V$ (for the analysis of the inner/outer electrodes as source or drain), with $V_{TG} = -0.5V$.

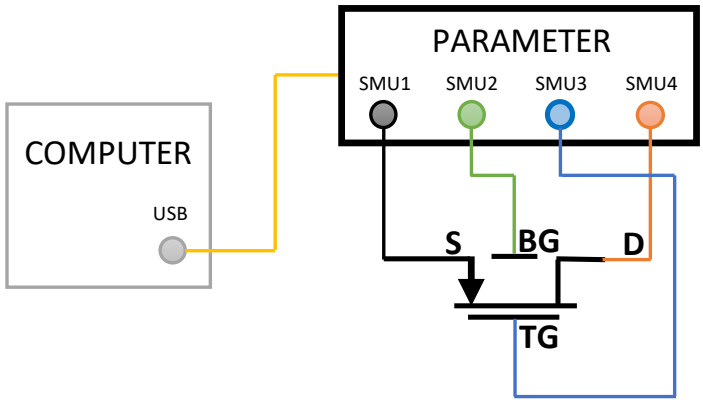

Figure 2.5: *Measurement set-up.*

2.3 Characterization results

Transfer characteristics of devices have been investigated in order to extrapolate the threshold voltage and the mobility of EGOFETs in different conditions. The threshold extrapolation has been carried out by means of three methods, according to the feasibility of the fit, in saturation regime (respectively $V_{BG} = -15V = V_{DS}$ and $V_{TG} = -0.5V = V_{DS}$). α has been computed by applying derivative (eq.2.3.1) or integral (eq.2.3.2) methods:

$$y = \frac{I_{DS_{sat}}}{\delta I_{DS_{sat}}} = \frac{V_{GS}}{\alpha + 2} - \frac{V_{th}}{\alpha + 2} \tag{2.3.1}$$

$$y = \frac{\int I_{DS_{sat}}}{I_{DS_{sat}}} = \frac{V_{GS}}{\alpha + 3} - \frac{V_{th}}{\alpha + 3} \tag{2.3.2}$$

where, from the linear fit $y = m \cdot V_{GS} + q$:

$$V_{th} = -\frac{m}{q} \qquad \alpha = \begin{cases} \frac{1}{m} - 2 & derivative \\ \frac{1}{m} - 3 & integral \end{cases} \tag{2.3.3}$$

If not possible, α was forced to 0 and the square root method (eq.2.3.4) has been applyied:

$$\sqrt{I_{DS_{sat}}} = \sqrt{\frac{1}{2}\mu_{FET} C_I \frac{W}{L}}(V_{GS} - V_{th}) \tag{2.3.4}$$

Once extrapolated V_{th}, the field-effect mobility has been computed from the relative equation of I_{DS}.

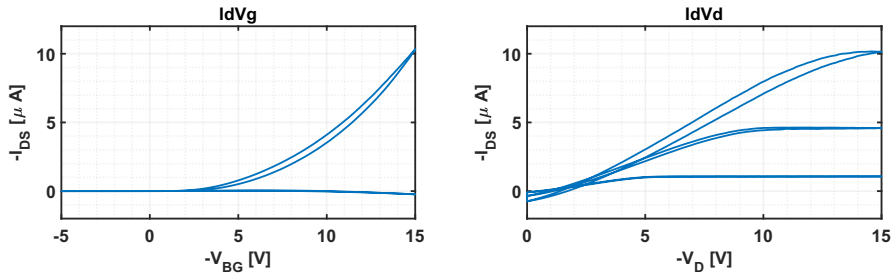

Figure 2.6: *$QS - I_{DS}V_{BG}$ and $QS - I_{DS}V_D$ on back gate.*

Back-Gate transfer and output characteristics were performed on interdigitated lateral gate EGOFETs in order to verify the operation of the devices (Fig.2.6). Typical threshold voltage values around $-1.10V$ have been extrapolated from measurements. Above this voltage, the back-channel starts to accumulate carriers and the back-gate organic field-effect transistor turn on. The back-gate modulaton on the top channel voltage threshold were investigated by means of V_{BG} scan from $0V$ to $50V$ (Fig.2.7). Consecutive measurements show that the modulation preserves its effectiveness, altough, due to charge trapping, the variation of V_{th} is shifted. On Fig.2.8 we can see that below $20V - 30V$ of V_{BG}

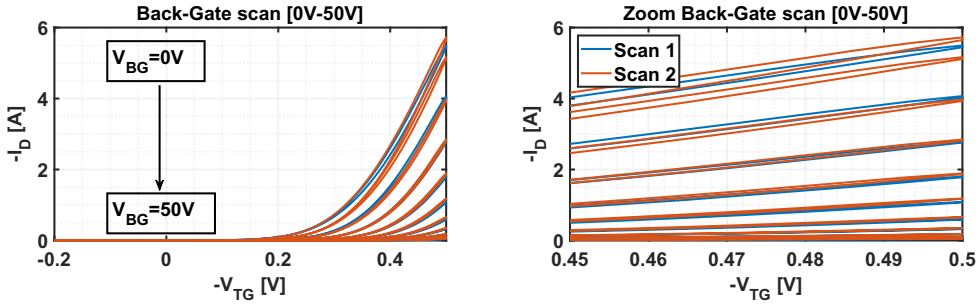

Figure 2.7: *$QS - I_{DS}V_{TG}$ on top gate at different V_{BG}, from 0V to 50V.*

the device works according to eq.(1.5.2). Above $V_{BG} = 30V$ the modulation of V_{th} vanishes and the field-effect mobility is lowered by more than 90% likely due to charge trapping.

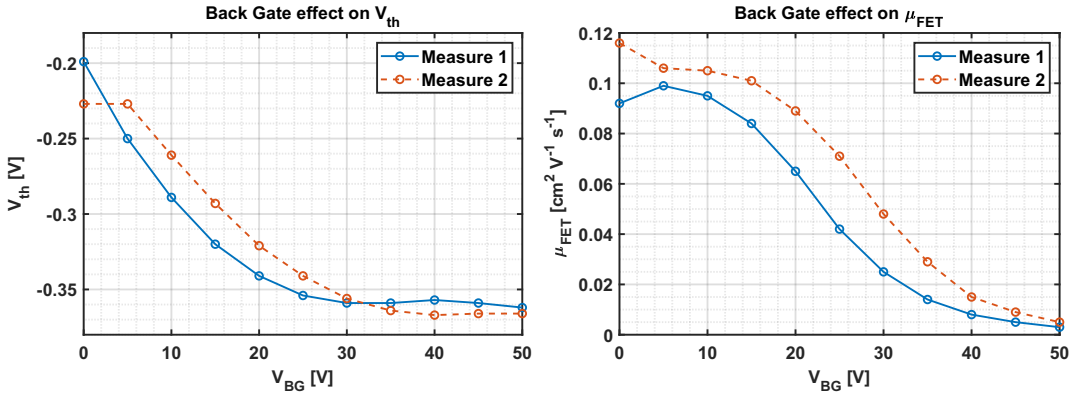

Figure 2.8: *Consecutive V_{BG} scan from 0V to 50V: a) Effect on V_{th} b) Effect on μ_{FET}.*

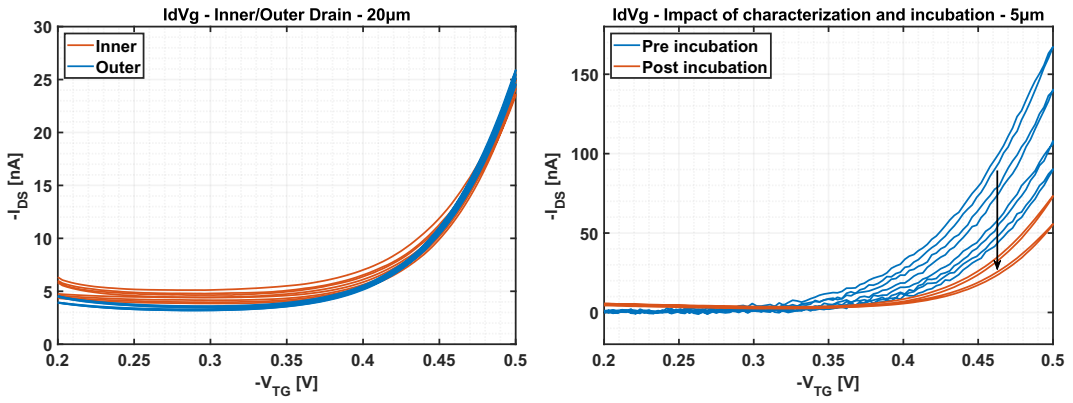

Figure 2.9: *1) Consecutive $QS - I_{DS}V_{TG}$ alternating source and drain connections 2) Impact of characterization and incubation.*

The choice of the inner or outer electrode on Corbino layout as Drain or Source has been done performing multiple measurements with the same bias conditions. Using the outer annular electrode as the Drain electrode reduces gate leakage and I_{DS} hysteresis, as it can be seen in Fig.2.9 1). The performance decay is mostly caused by the intrinsic and characterization induced degradation rather than the incubator effect (Fig.2.9 2)).

2.3.1 Coatings effect

Different coatings for cell seeding have been tested in order to observe their effect on electrical performances of the Corbino layout devices. Results are reported below, regarding Poly-L-lysine and Matrigel treatments.

PLL

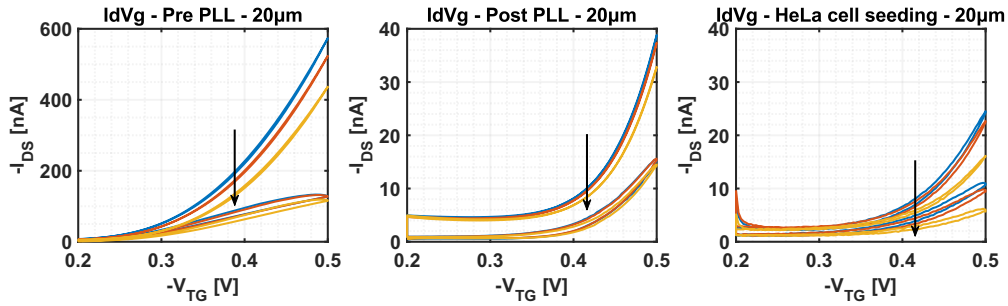

Figure 2.10: *$QS - I_{DS}V_{TG}$ without coating, after PLL coating, after HeLa cell seeding.*

Table 2.3: Threshold voltage and mobility with PLL.

	Pre PLL	***Post PLL***	***Post HeLa***
$\mathbf{V_{th}}$ $[\mathbf{mV}]$	-159	-363	-370
μ_{FET} $[cm^2/Vs]$	0.290	0.090	0.060
$\boldsymbol{\alpha}$	0.723	0	0

In Fig.2.10 are shown the transfer characteristics of the devices before the coating, after 4.5 hours of PLL deposition and after HeLa cell seeding. The transistor feature a drastic loss of performance mainly ascribable to a conspicuous shift in the threshold voltage, as it can be noticed on table 2.3. The contribution of leakage before and after the treatment is mostly the same. The main cause of current reduction seems to be correlated to the coating, rater than to the seeding of the cells.

Matrigel

EGOFETs were coated with Matrigel at different concentrations and put in incubation for 24 hours. Sample A with no Matrigel as reference device, B with Matrigel 1:50, C with Matrigel 1:200 and D with Matrigel 1:100. Electrical performances seems to be not affected by Matrigel, both on $5\mu m$ and $20\mu m$ layouts. Moreover, Matrigel ensures a good coverage of the sample with cells, as can be observed by cell imaging in Fig2.12. Different concentrations of Matrigel do not change much the cells density, but they have a small impact on their shape.

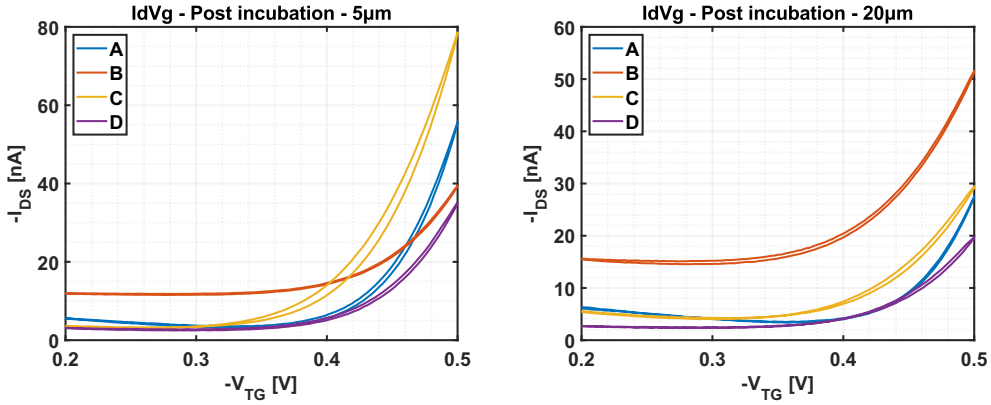

Figure 2.11: *$QS - I_{DS}V_{TG}$ at different concentrations of Matrigel: A) No Matrigel B) Matrigel 1:50 C) Matrigel 1:200 D) Matrigel 1:100.*

Table 2.4: Threshold voltage and mobility with Matrigel pre incubation - $5\mu m$.

	A	*B*	*C*	*D*
$\mathbf{V_{th}}$ $[\mathbf{mV}]$	-382	-373	-350	-355
μ_{FET} $[cm^2/Vs]$	0.276	0.230	0.291	0.185

Table 2.5: Threshold voltage and mobility with Matrigel post incubation - $5\mu m$.

	A	*B*	*C*	*D*
$\mathbf{V_{th}}$ $[\mathbf{mV}]$	-393	-306	-359	-376
μ_{FET} $[cm^2/Vs]$	0.274	0.057	0.193	0.104

Table 2.6: Threshold voltage and mobility with Matrigel pre incubation - 20μm.

	A	*B*	*C*	*D*
$\mathbf{V_{th}}$ $[\mathbf{mV}]$	-398	-361	-321	-332
μ_{FET} $[cm^2/Vs]$	0.230	0.108	0.088	0.075

Table 2.7: Threshold voltage and mobility with Matrigel post incubation - 20μm.

	A	*B*	*C*	*D*
$\mathbf{V_{th}}$ $[\mathbf{mV}]$	-401	-285	-321	-366
μ_{FET} $[cm^2/Vs]$	0.145	0.054	0.050	0.049

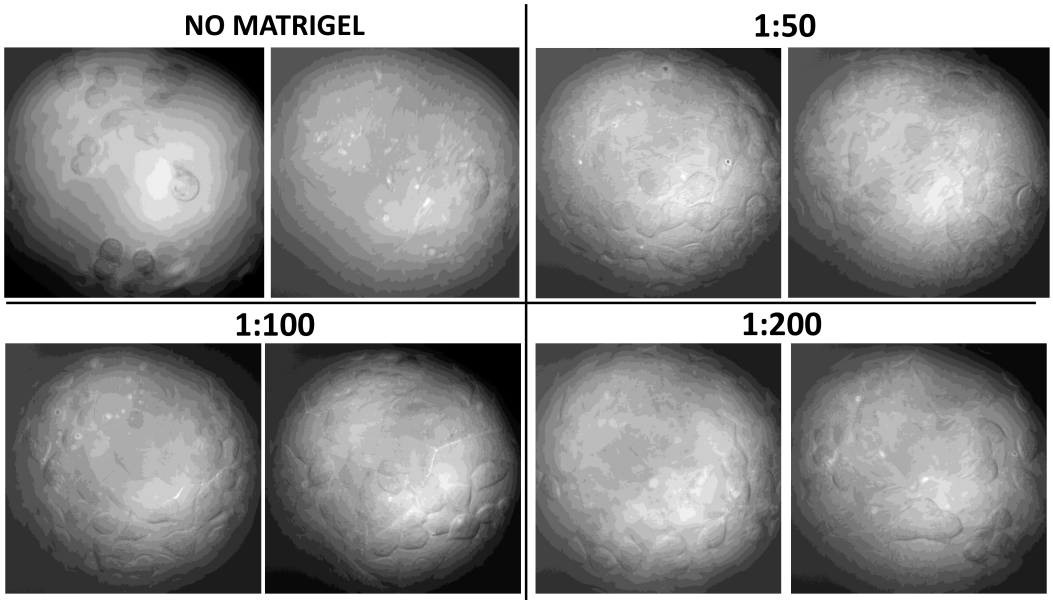

Figure 2.12: *Cell seeding imaging:*
A) No Matrigel B) Matrigel 1:50 C) Matrigel 1:200 D) Matrigel 1:100.

Better overall results are achieved for 1:100 concentration of Matrigel. On the following tables are reported the values of field-effect mobility and threshold voltage at different concentrations and layout, before and after the incubation.

2.3.2 Degradation

Samples A,B,C,D have been stored in air with extracellular solution (to keep Matrigel functionality) for over a month. Measurements show a non-monotonous decrease in performances (Fig.2.13). Samples stop to exhibit a field-effect behavior around 35 days of storage.

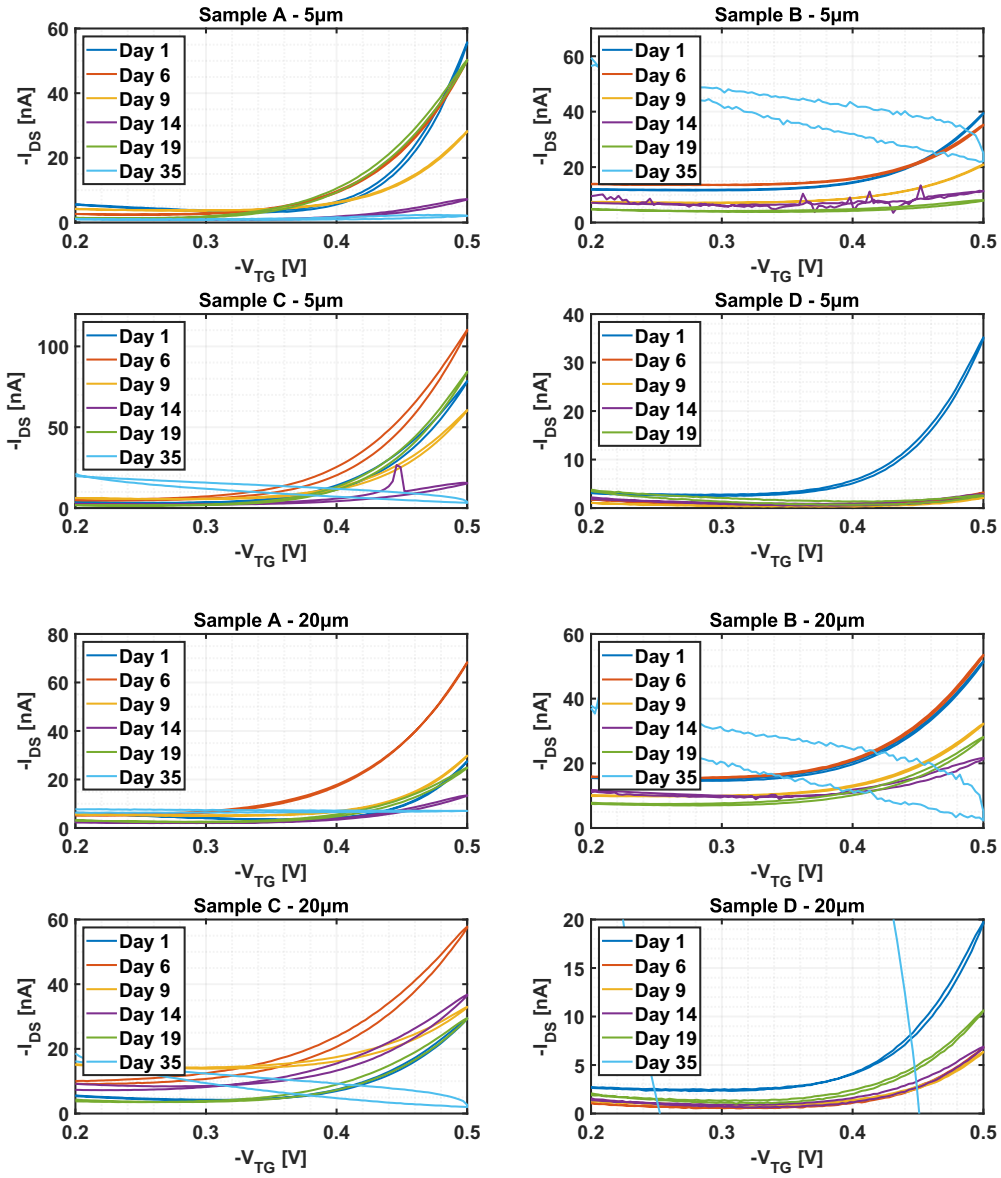

Figure 2.13: *Impact of 35 days storage at different concentrations of Matrigel: A) No Matrigel B) Matrigel 1:50 C) Matrigel 1:200 D) Matrigel 1:100.*

2.3.3 Digital control effect

In Fig.2.14 are reported typical Top-Gate transfer and output characteristics, whereas in Fig.2.15, $QS - I_{DS}V_{TG}$ have been performed at different V_{BG}, before and after a sequence of digital control experiments. Average values of V_{th} and μ_{FET} are listed on table 2.8*. Devices show similar threshold values before and

after the tests and the overall voltage threshold shift is almost the same over all the measurements ($\Delta V_{th}(V_{BG} = 0V) \simeq 0.082V$ and $\Delta V_{th}(V_{BG} = 5V) \simeq 0.049V$).

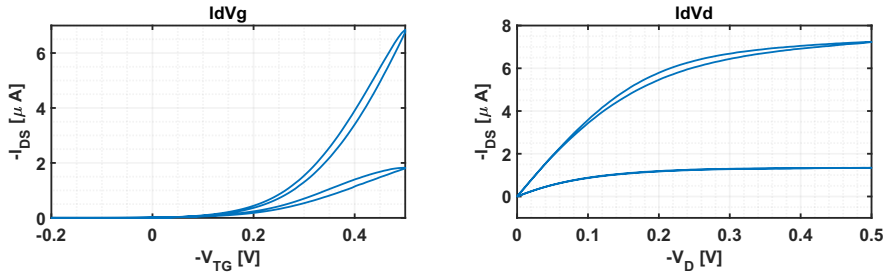

Figure 2.14: *$QS - I_{DS}V_{TG}$ and $QS - I_{DS}V_D$ on top gate.*

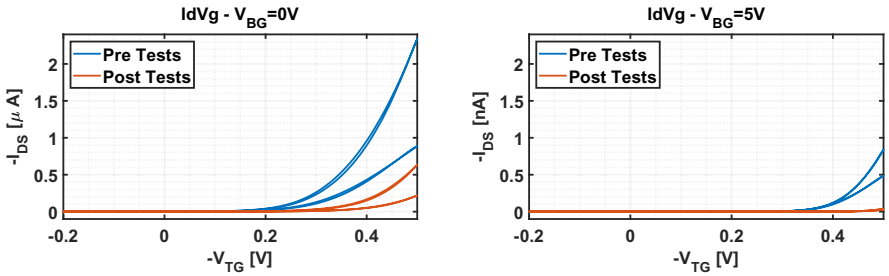

Figure 2.15: *$QS - I_{DS}V_{TG}$ on top gate at different V_{BG}, before and after the experiments.*

Table 2.8: Threshold voltage and field-effect mobility during digital control experiments - a)$V_{BG} = 0V$ b)$V_{BG} = 5V$.

a)	$\overline{\mathbf{V}}_{\mathbf{th}}$ [mV]	$\overline{\mu}_{FET}$ $[cm^2/Vs]$
Pre	−233	0.051
Post	−315	0.030
b)	$\overline{\mathbf{V}}_{\mathbf{th}}$ [mV]	$\overline{\mu}_{FET}$ $[cm^2/Vs]$
Pre	−341	0.053
Post	−389	0.018

*

$\sigma^2_{V_{th}}(Pre\text{-}V_{BG} = 0V) = 0.018V^2$
$\sigma^2_{V_{th}}(Post\text{-}V_{BG} = 0V) = 0.033V^2$
$\sigma^2_{V_{th}}(Pre\text{-}V_{BG} = 5V) = 0.019V^2$
$\sigma^2_{V_{th}}(Post\text{-}V_{BG} = 5V) = 0.008V^2$
$\sigma^2_{\mu_{FET}}(Pre\text{-}V_{BG} = 0V) = 0.0026(cm^2/Vs)^2$
$\sigma^2_{\mu_{FET}}(Post\text{-}V_{BG} = 0V) = 0.0029(cm^2/Vs)^2$
$\sigma^2_{\mu_{FET}}(Pre\text{-}V_{BG} = 5V) = 0.0070(cm^2/Vs)^2$
$\sigma^2_{\mu_{FET}}(Post\text{-}V_{BG} = 5V) = 0.0074(cm^2/Vs)^2$

Chapter 3

Digital Control

EGOFETs typically exhibit a continuous current drift for long-time periods, that changes its magnitude and shape over time. This can be mostly brought back to the transformation of mobile carriers into immobile carriers, when the device operates in aqueous media. This phenomenon leads to a threshold voltage shift towards the gate voltage applied, varying the operative point. It results in an operational instability and a distortion of the output signal. Regarding biochemical sensors applications, the EGOFET transduces an input signal (*e.g. cell action potential*) into an output current, from which we can extract the information related to the sensed input. Since the current drift induces a variable distortion of the recorded signal over time, the device can be used only for brief detections, with complicate post-processing techniques for the extraction of useful signals. In this chapter we focus on a theoretical formulation of the problem and the study of an alternative approach to achieve a well-defined output signal, by exploiting an additional gate to control the threshold voltage of the transistor. We started from the definition of the model of the system, then we have proceeded with the design of a digital control that dynamically changes the back gate (*i.e.* $Si/Si0_2$) potential to stabilize the operating point of the device. Finally, different methods to preserve a hypothetical cell action potential response are presented.

3.1 Problem formulation

The EGOFET is considerated in dual-gate operation in saturation regime, according to the equation defined on chapter 1.
NOTATION:

- $i_{DS}(t)$ output drain-to-source EGOFET current
- I_{DS} constant component of $i_{DS}(t)$
- $i_{ds}(t)$ time-varying component of $i_{DS}(t)$

- $v_{BG}(t)$ back-gate potential and control variable of the EGOFET
- V_{BG0} initial bias point of the back-gate and constant component of $v_{BG}(t)$
- $v_{bg}(t)$ time-varying component of $v_{BG}(t)$

The characteristic current drift to eliminate, typically presents a stretched exponential variation, as we can observe on the measurements reported in Fig.3.1. This behaviour can be approximated by an exponential shift of the transistor threshold voltage:

$$V_{th} = V_{th0} + \Delta V e^{-\frac{t}{\tau}} \tag{3.1.1}$$

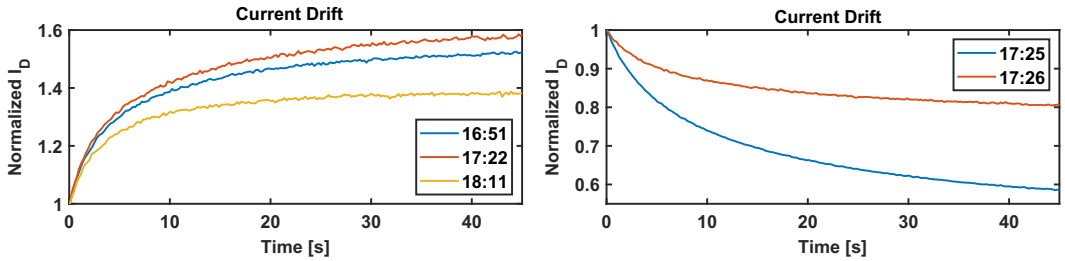

Figure 3.1: *Measured current drift over time, normalized to I_{D_0}, in two different samples.*

3.1.1 Previous approach

The first idea to overcome to this issue was based on the definition of two control variables ΔI and ΔV, in order to maintain the output current at a given I_{REF} target value. The digital control acts fulfilling the following rule:

$$\begin{cases} v_{BG}(t_{i+1}) & = v_{BG}(t_i) - \Delta V & if\ iDS(t_i) < I_{REF} - \Delta I \\ v_{BG}(t_{i+1}) & = v_{BG}(t_i) + \Delta V & if\ iDS(t_i) > I_{REF} + \Delta I \\ v_{BG}(t_{i+1}) & = v_{BG}(t_i) & otherwise \end{cases} \tag{3.1.2}$$

The drawbacks of this control are the intrinsic instability of the system and the impossibility to decouple any sensed signal from the current drift, forcing a constant output. Since its response is fixed and it is based on the instantaneous error, unavoidable oscillation of the current can be lowered only by reducing ΔV and ΔI. However, the smaller the control variables, the slower the response of the system, making the digital control unsuitable.

In order to design an ad-hoc digital control to correctly compensate this detrimental behaviour, it is worthwhile to analyse the model of the system on its small-signal operation and define the variables involved.

3.1.2 Modeling and linearization

Starting from eq.(1.5.1) in saturation regime, considering the dual-gate operation (eq.(1.5.2)) and the threshold shift (3.1.1), we can define the output current of the EGOFET as:

$$i_{DS}(t) = -\frac{1}{2}\frac{W}{L}C_{TG}\mu_{FET}(V_{GS} - V_{th0} - \Delta V e^{-\frac{t}{\tau}} + \frac{C_S}{C_{TG}}V_{BG})^2 \tag{3.1.3}$$

where V_{BG} is our control variable and we can consider it as the sum of the initial bias point of the device V_{BG0} and the time-varying output of the control $v_{BG}(t)$:

$$v_{BG}(t) = V_{BG0} + v_{bg}(t) \tag{3.1.4}$$

Therefore we can decompose $i_{DS}(t)$ into a constant component:

$$I_{DS} = -\frac{1}{2}\frac{W}{L}C_{TG}\mu_{FET}(V_{GS} - V_{th0} + \frac{C_S}{C_{TG}}V_{BG0})^2 \tag{3.1.5}$$

and a time-varying component:

$$\begin{aligned} i_{ds}(t) &= -\frac{1}{2}\frac{W}{L}C_{TG}\mu_{FET}\left\{[X(t)]^2 + 2(V_{GS} - V_{th0} + \frac{C_S}{C_{TG}}V_{BG0})[X(t)]\right\} \\ X(t) &= \left(-\Delta V e^{-\frac{t}{\tau}} + \frac{C_S}{C_{TG}}v_{bg}(t)\right) \end{aligned} \tag{3.1.6}$$

We linearize the system around the operating point $X(t) = 0$, where there is no disturbance (or it is compensated $\frac{C_S}{C_{TG}}v_{bg}(t) = \Delta V e^{-\frac{t}{\tau}}$). The time-varying component is nullified and the system is at steady-state, described by:

$$\begin{aligned} i_{DS}(t) &\simeq I_{DS} + \left.\frac{\delta i_{DS}(t, X(t))}{\delta X(t)}\right|_{X(t)=0} \cdot X(t) \\ &\simeq I_{REF} + \underbrace{g_{m_{BG}}v_{bg}(t)}_{\hat{i}_{ds}(t)} + \underbrace{h_m \Delta V e^{-\frac{t}{\tau}}}_{d(t)} \end{aligned} \tag{3.1.7}$$

$$g_{m_{BG}} = -C_S\mu_{FET}\frac{W}{L}(V_{GS} - V_{th0} + \frac{C_S}{C_{TG}}V_{BG0}) \tag{3.1.8}$$

$$h_m = C_{TG}\mu_{FET}\frac{W}{L}(V_{GS} - V_{th0} + \frac{C_S}{C_{TG}}V_{BG0}) \tag{3.1.9}$$

Where $g_{m_{BG}}$ is the bottom-gate thin-film-transistor transconductance and $d(t)$ is the exponential drift of the current. I_{DS} can be chosen as reference value I_{REF} for the DC component. We assumed that the time-varying component $X(t)$ over time is sufficiently small and slow, so that the response will be still linear and the model can be generalized to a generic disturbance with these characteristics. This is ensured by the action of the feedback control.

The first aim of the control is to keep the output current constant, by nullifying the time-varying component $i_{ds}(t) \simeq \hat{i}_{ds}(t) + d(t)$. Since the plant of the system has been made up through several assumptions and the actual disturbance can change its behaviour during operation, we introduce a feedback control with a controller C and we represent the equivalent small signal block diagram of the system as follow:

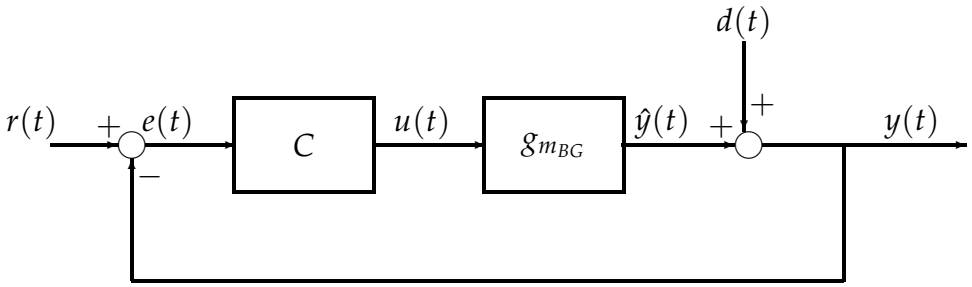

Figure 3.2: *Equivalent small signal block diagram.*

$i_{ds}(t) = 0$ represent the reference signal $r(t)$, $e(t) = -i_{ds}(t)$ is the feedback error, $v_{bg}(t)$ is the control variable $u(t)$ and $d(t)$ the generic disturbance, which, in addition to the response $\hat{y}(t) = \hat{i}_{ds}(t)$ of the plant $g_{m_{BG}}$, constitutes the time-varying component $y(t) = i_{ds}(t)$ of the system.

3.2 Control design

Within the frequencies of interest (low frequency), our plant $g_{m_{BG}}$ can be treated as a constant gain, without any significant dynamic behaviours. The digital control we need to design has to satisfy only steady-state performance targets, that are output disturbances rejection and reference tracking. The design approach is developed on a continuous-time small-signal description of the plant and the analog compensator on the Laplace-domain. Then, we proceed to its discretization, by means of *"Tustin discretization approach"*, to transform the s plane into the discrete plane z.

3.2.1 Basics of PID control

One of the simplest and at the same time more robust controller commonly adopted is the PID regulator. Its control law computes the control signal as the sum of three contributions: the Proportional (P), Integral (I) and Derivative (D) actions (also called *"control modes"*):

$$u(t) = K_P e(t) + K_I \int e(t)\delta t + K_D \frac{\delta e(t)}{\delta t} \tag{3.2.1}$$

In the s domain, the transfer function $C(s) = \frac{U(s)}{E(s)}$ is:

$$C(s) = K_P + \frac{K_I}{s} + K_D s \tag{3.2.2}$$

Proportional mode (P)

The control law of the proportional mode P is given by:

$$u_P(t) = K_P e(t) + u_b \tag{3.2.3}$$

where K_P is the proportional gain and u_b is a *"reset/bias value"*.
As the name suggests, its effect is proportional to the instantaneous value of the error, improving the responsiveness of the system. At steady-state it is ideally zero if and only if the steady-state regime can be reached without control. For this reason it needs the bias term to correctly work. This is typically made by the integral action.

Integral mode (I)

The integral mode I has the following control law:

$$u_I(t) = K_I \int e(t)\delta t + u(0) \tag{3.2.4}$$

The action of the controller is proportional to the accumulated error of the system. It can be viewed as an automatic reset of the bias term of the proportional controller. It is slower in responding to the error, however it is fundamental to reach and hold the steady-state condition.

Derivative mode (D)

The derivative control law is given by:

$$u_D(t) = K_D \frac{\delta e(t)}{\delta t} \tag{3.2.5}$$

The control is proportional to the variations of the error signal. It follows that whenever there are no changes on the error signal, the derivative contribute is zero. Derivative action generally improves the loop stability with a quick response. On the other hand, the dependency on the speed and variation of the error may lead to undesired behaviour in presence of noise or sudden changes of reference.

3.2.2 Steady-state performance

Reference signal tracking

When we set the DC reference to a certain I_{REF}, we want the steady-state error $e(\infty)$ to be zero. In the s-domain, $e(t)$ becomes:

$$E(s) = \frac{1}{1+T(s)}R(s) \tag{3.2.6}$$

where $T(s) = C(s)g_{m_{BG}}(s)$ is the loop gain.
Applying the final value theorem, the steady-state error is described by:

$$\begin{aligned} \lim_{t\to\infty} e(t) &= \lim_{s\to 0} s \cdot E(s) \\ &= \lim_{s\to 0} s \cdot \frac{1}{1+T(s)}R(s) \\ &= \lim_{s\to 0} s \cdot \frac{1}{1+T(s)}\frac{\Delta I_{REF}}{s} \end{aligned} \tag{3.2.7}$$

$R(s) = \frac{\Delta I_{REF}}{s}$ step of DC reference signal.

From eq.(3.2.9) we can observe that the steady-state error is zeroed only if $T(s) \sim \frac{1}{s^n}$ with $n \geq 1$.

Disturbance rejection

The error due to a generic output disturbance $d(t)$ is given by:

$$E(s) = \frac{1}{1+T(s)}D(s) \tag{3.2.8}$$

Where the disturbance $D(s)$ can be approximated by an exponential decay $D(s) = const \cdot \frac{\tau}{s+\tau}$. Then, applying the final value theorem:

$$\begin{aligned} \lim_{t\to\infty} e(t) &= \lim_{s\to 0} s \cdot E(s) \\ &= \lim_{s\to 0} s \cdot \frac{1}{1+T(s)}D(s) \\ &= \lim_{s\to 0} s \cdot \frac{1}{1+T(s)}\frac{\tau}{1+s\tau} \cdot const \end{aligned} \tag{3.2.9}$$

Under these assumptions the error goes to zero with no need of any compensation. However, typically the behaviour of the current drift presents slow decay, meaning high value of τ. Consequently, a further approximation can be made considering $D(s) \simeq \frac{const}{s}$, from which we can take the same conclusions obtained by the previous discussion.

Therefore, in order to satisfy the minimum steady-state requirements, we need at least an integrator $C(s) = \frac{K_I}{s}$. The proportional part can be added to improve the response of the system in terms of promptness or stability. The derivative action, considering the nature of the system, is not needed.
The controller becomes:

$$C(s) = K_P + \frac{K_I}{s} = K_I \frac{1 + s\tau_{PI}}{s} \tag{3.2.10}$$

with $\tau_{PI} = \frac{K_P}{K_I}$.

3.2.3 Dynamic performance

The stability of the system can be studied by means of Bode's criterion, since the open loop gain $T(s) = g_{m_{BG}} K_I \frac{1+s\tau_{PI}}{s}$ has no real positive poles and it crosses $T(s) = 0dB$ only one time. Requirements for stability of the closed loop system are: gain margin G_M positive (dB) and phase margin Φ_M positive. Then the control design will be refined through the choice of specific phase margin Φ_M and crossover frequency ω_c parameters.

Gain margin

The gain margin is defined as the amount of change in open-loop gain needed to make the closed-loop system unstable. It can be calculated as the difference between $0dB$ and the gain at the frequency where $\angle T(j\omega) = -180°$:

$$G_M = 20log\left(\frac{1}{|T(j\omega_{G_M})|}\right)dB \tag{3.2.11}$$

$\angle T(s)$ can reach $-180°$ only if $K_P < 0$, for $s \to \infty$. Then we obtain the first constraint:

$$G_M = \frac{1}{|g_{m_{BG}} K_P|} > 1 \qquad \to \qquad |K_P| < \frac{1}{|g_m|} \tag{3.2.12}$$

Phase margin

The phase margin represents the amount of change in open-loop phase needed to make a closed-loop system unstable. It is defined as the difference in phase between $180°$ and the phase of $T(s)$ at the gain crossover frequency ω_c, where $|T(j\omega_c)|_{dB} = 0dB$:

$$\Phi_M = \pi + \angle T(j\omega_c) \tag{3.2.13}$$

Recalling that $T(s) = g_{m_{BG}} K_I \frac{1+s\tau_{PI}}{s}$ with $g_{m_{BG}} > 0$, we can write its module and phase as:

$$T(jw) = \begin{cases} |T(j\omega)| & = |\frac{g_{m_{BG}} K_I}{\omega}| \sqrt{1 + \tau_{PI}^2 \omega^2} \\ \angle T(j\omega) & = \angle g_{m_{BG}} K_I + \angle(1 + j\omega\tau_{PI}) - \angle j\omega \end{cases} \tag{3.2.14}$$

According to the sign of K_I, the open-loop phase becomes:

$$\angle T(j\omega) = (sgn(K_I) - 1)\frac{\pi}{2} + \angle(1 + j\omega\tau_{PI}) - \frac{\pi}{2} \tag{3.2.15}$$

Knowing that $|T(j\omega_c)| = 1$ and considering eq.(3.2.15) with eq.(3.2.13), we obtain the system of equations from which we can express the PI gains in function of Φ_M and ω_c:

$$\begin{cases} |T(j\omega_c)| & = |\frac{g_{m_{BG}} K_I}{\omega}| \sqrt{1 + \tau_{PI}^2 \omega_c^2} = 1 \\ \Phi_M & = \pi + (sgn(K_I) - 1)\frac{\pi}{2} + tan^{-}1\left(\frac{\omega_c \tau_{PI}}{1}\right) - \frac{\pi}{2} \end{cases} \tag{3.2.16}$$

From eq.(3.2.16) we get:

$$|K_P| = \frac{1}{|g_{m_{BG}}|} \sqrt{1 - \frac{1}{1 + tan^2(\Phi_M + \beta)}} \tag{3.2.17}$$

$$|K_I| = \frac{\omega_c}{|g_{m_{BG}}|} \frac{1}{\sqrt{1 + tan^2(\Phi_M + \beta)}} \tag{3.2.18}$$

where:

$$\beta = \begin{cases} - \frac{\pi}{2} & if\ K_I > 0 \\ \frac{\pi}{2} & if\ K_I < 0 \end{cases} \tag{3.2.19}$$

From PI gains equations we can notice that the gain margin condition (eq.3.2.11) is always fullfilled. With $K_P = 0$ the controller consists on a simple integrator with a phase margin of 90°. The sign of K_P determines the variation of the phase margin below or above 90°. In fact, a negative sign corresponds to a non-minimum phase controller, that theoretically would worsen our system response. The action of a negative proportional part is to initially increase the error instead of counteracting it (positive feedback). However, since we start from a condition of high stability, the idea to decrease the phase margin may find function on speeding up the system response. Therefore, the uncommon action of a negative proportional gain would have the effect to charge up the integral controller, making the response faster, with the drawback of an initial overshoot on the error. It can be overlooked in our system, since we are more interested in the steady-state response of the device.

Crossover frequency

The tuning of the crossover frequency must be done according to the signals we are dealing with. First of all we want to eliminate all the perturbation on the output current, that we treat as output disturbances $d(t)$. As reported in eq.(3.2.8), the transfer function of the error indicates that these disturbances can be counteracted by feedback if their frequency content does not extend the crossing frequency ω_c and $|T(j\omega)|$ is big for $\omega \ll \omega_c$. On the other hand, we want to preserve a hypothetical cell action potential, which can be considered as an additional signal summed up to the output (AP in Fig.3.3).

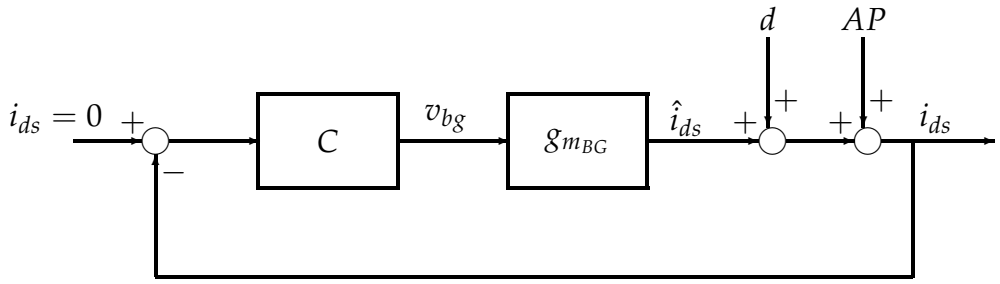

Figure 3.3: *Equivalent block diagram with action potential.*

The measurement set-up is limited by significant constraints regarding the minimum reachable sampling time ($T_s \sim 200ms$) (it is controlled by a Desktop Computer by using Matlab®). Hence, we performed a theoretical approach that can be scaled up without loss of generality. According to Shannon's sampling theorem, every continuous-time signal $y(t)$ with a band-limited spectrum ($|Y(j\omega)| = 0 \; \forall \; |\omega| > \omega_B$) can be exactly reconstructed from the impulsively sampled signal $y^*(t)$ only if $\omega_B < \omega_N$, where $\omega_N = \omega_s/2 = \pi/T_s$ denoting the Nyquist frequency. The action potential, according to Hodgkin-Huxley model, has been simulated by using an arbitrary waveform generator (*Rigol DG1000*) with a resolution of 4096 points. It has been used to set the top-gate potential of the EGOFET to emulate the cell activity, with a period of 15s and a DC offset of $-0.5V$ (Fig.3.4). According to literature, we have summarized three main characteristics of the AP: amplitude ($A_1 = |y(A) - y(B)|$ $A_2 = |y(B) - y(C)|$), duration ($D_1 = |x(A) - x(B)|$ $D_2 = |x(B) - x(C)|$), and slopes ($S_1 = D_1/A_1$ $S_2 = D_2/A_2$).

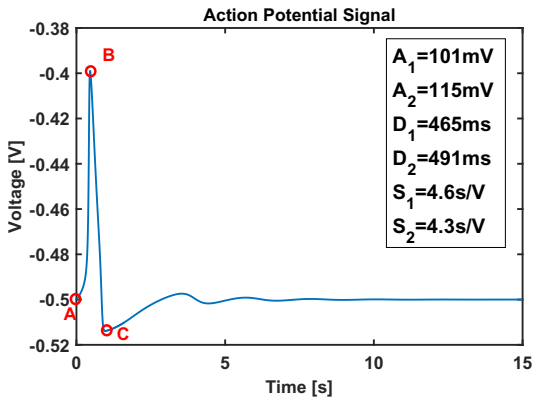

Figure 3.4: *Cell action potential.*

We can compute the Discrete Fourier Transform (*DFT*) to study the spectra of our signals and choose an appropriate ω_c:

$$Y(k) = \sum_{j=1}^{n} Z(j) W_n^{(j-1)(k-1)} \tag{3.2.20}$$

where $W_n = e^{(-2\pi i)/n}$.

The previously defined action potential normalized spectrum is represented in the Fig.3.5. The Nyquist frequency is marked in red and it is noticeable that a minimum part of the signal will be lost due to slow sampling rate, however the difference is negligible.

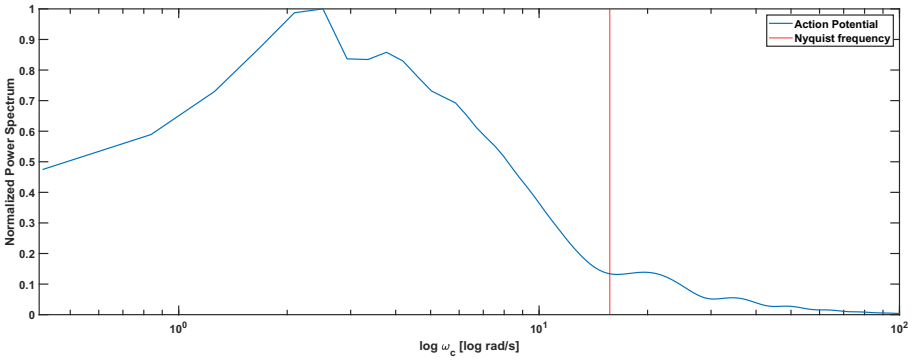

Figure 3.5: *Normalized power spectra of the cell action potential.*

In order to preserve the cell signal, ω_c has to be lower than its range of frequencies. In the next figure (3.6) it is shown the normalized spectra of the signals of interest (data from measures in Fig.3.1 regarding the output disturbance). We can see that the current drift is reduced by over 95% for $\omega_c > 0.5 rad/s$,

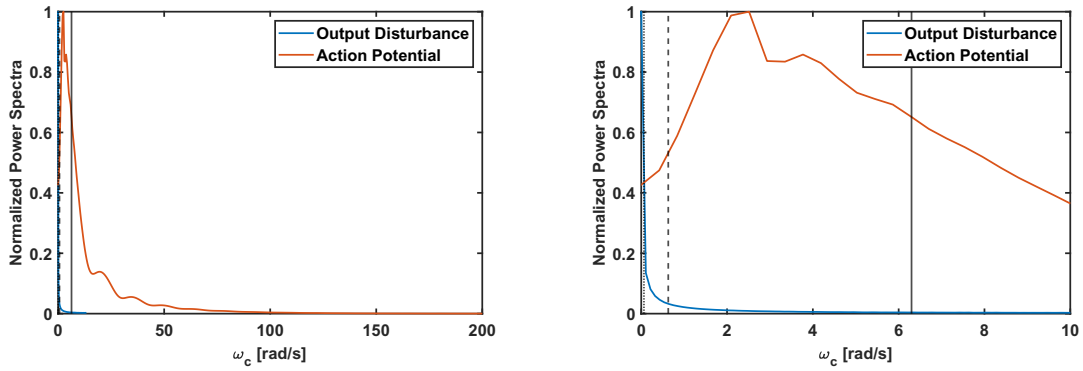

Figure 3.6: *Normalized power spectra of the disturbance and the cell action potential.*

but part of the action potential has components at lower frequencies. Three different frequencies are highlighted on the graphs, which corresponds to $\omega_{c1} = 0.0628 rad/s$ (action potential well preserved but half of the disturbance is not compensated), $\omega_{c2} = 0.628 rad/s$ (tradeoff that well rejects the current

drift and do not significantly affects the cell signal) and $\omega_{c3} = 6.28 rad/s$ (distubance completely eliminated, as well as most of the action potential).

Another aspect to keep in consideration is the rejection of high frequency measurement noise, which can be represented as an additional signal summed up on the feedback line. The transfer function from the noise input $N(s)$ to the output is defined by $-\frac{T(s)}{1+T(s)}$, therefore $|T(j\omega)|$ has to be low at $\omega \gg \omega_c$. This is complied by all the frequencies highlighted before.

3.2.4 Tustin discretization

After the continuous-time domain design has been performed, a discrete-time controller is obtained by applying a discretization procedure, approximating the response of the original one.
The Tustin (trapezoidal) discretization approach is based on a $s \Leftrightarrow z$ map that transforms the left-half plane to the unit-circle:

$$s = \frac{2}{T_s}\frac{z-1}{z+1} \qquad \Leftrightarrow \qquad z = \frac{1+s\frac{T_s}{2}}{1-s\frac{T_s}{2}} \tag{3.2.21}$$

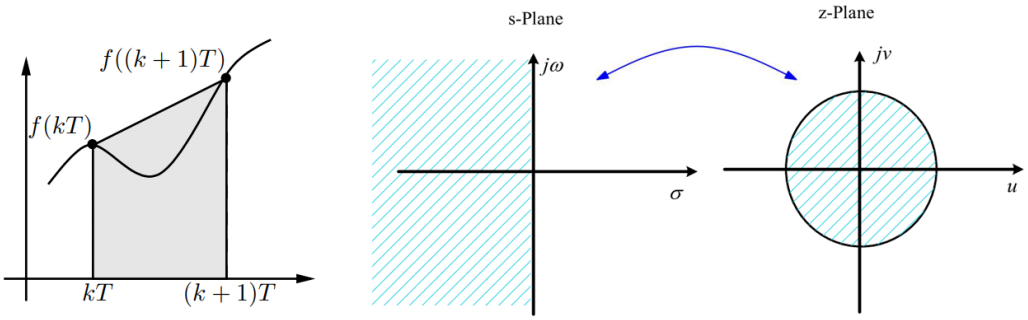

Figure 3.7: *Tustin discretization map.*

The higher the frequency is, the worse the match will be. Usually, for a good match we need a sampling frequency greater by a factor of 10 w.r.t. the frequency of interest. For lower sampling rates the frequencies get warped, according to:

$$\omega_{warped} = \frac{2}{T_s} tan^{-1}\left(\omega\frac{T_s}{2}\right) \tag{3.2.22}$$

Recalling the continuous controller eq.(3.2.10), the equation of the discretized compensator by using Tustin approach become:

$$C(z) = K_P + K_I \cdot \frac{T_s}{2}\frac{z+1}{z-1} \tag{3.2.23}$$

3.2.5 Saturation

In real applications, the control variable must be limited between a certain range of values as well as the derivative of its variation over time, otherwise several operational issues can occur.

Maximum range of back-gate potential

The back-gate potential has to be limited towards negative values in order to avoid the breakdown of the device. For this reason a value of $V_{BG} = -3V$ has been selected as minimum back-gate potential. The maximum value has been set to $V_{BG} = 30V$, because beyond this voltage electrons can accumulate at the SiO_2/OSC interface, partially screening the electric field induced by the back-gate potential. This phenomenon results in a reduction of the modulation of the threshold voltage V_{th}, as we can see on Fig.2.8-a). Furthermore, the electric field across the $200nm$ thick SiO_2 (back-gate dielectric) becomes larger than $1.5MV/cm$, causing electron tunnelling and the release of hydrogen, which yields to the formation of new interface states as well as other localized defects, explaining the decrease of the field-effect mobility as highlighted in Fig.2.8-b).

Maximum back-gate potential variation

Since sudden potential variations on the device can cause degradation on an organic device and when operating with cells, can trigger undesired action potentials, a limitation on the derivative of the control action over time is required (we choose $\Delta V_{BG_{max}} = 0.4V/s$). This boundary introduces a delay on the system response, which can be formalized as an additional cascade block $e^{-st_{delay}}$ on the loop that reduces the phase margin of the system. For this reason we must choose a sufficiently large phase margin to avoid instability in case this restriction is activated.

3.2.6 Autotuning

From the PI gains equations (3.2.17 and 3.2.18) we can observe the dependence by another parameter in addition to the phase margin and the crossing frequency: the back-gate transconductance $g_{m_{BG}}$. Recalling eq.(3.2.24), it is defined as:

$$g_{m_{BG}} = -C_S \mu_{FET} \frac{W}{L} (V_{GS} - V_{th0} + \frac{C_S}{C_{TG}} V_{BG0}) \tag{3.2.24}$$

Despite the elements of which it is composed are known ($\frac{W}{L}, V_{GS}, V_{BG0}$) or they can be estimated through specific preventive measures ($C_S, C_{TG}, V_{th0}, \mu_{FET}$), the degradation of the device due to these measurements or during operation over time makes necessary the implementation of a specific non-invasive method to obtain a real-time estimation of $g_{m_{BG}}$, that can be exploited to autotune the PI

gains. Two different ways to comply at this task are proposed, exploiting the classical definition of the transistor transconductance $g_{m_{BG}} = \frac{\delta I_{DS}}{\delta V_{BG}}$:

Back-gate voltage ramp

The first approach (Fig.3.8) is to apply an increasing ramp on the back-gate voltage at the maximum ΔV_{BG} it can sustain. Then a decreasing ramp brought back the value of the control to the normal operation. All this must be undertaken in a situation of steady-state regime, when the effect of the disturbance can be neglected. During the increasing ramp, the output current will respond with a correspondent growth, according to the linearized model we have defined in eq.(3.1.7). The differentiation between consecutive samples gives a series of estimations of the transconductance. Then the final estimation of $g_{m_{BG}}$ is computed averaging these values.

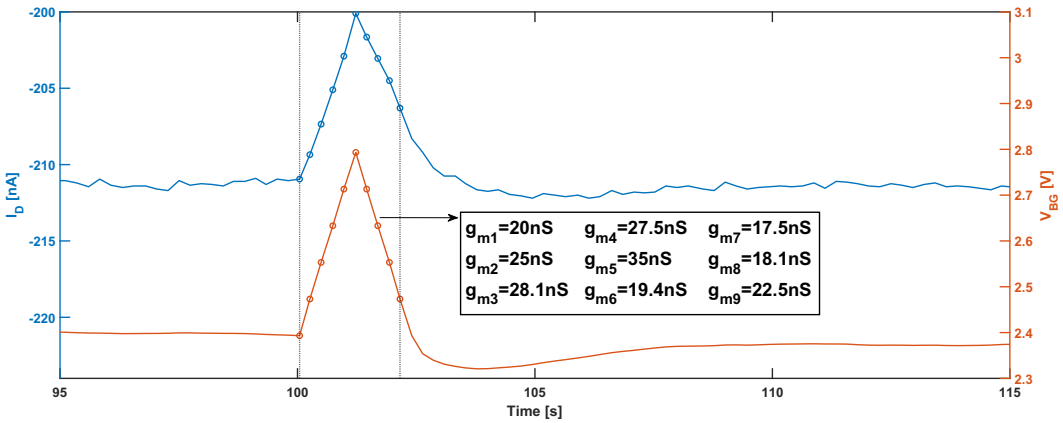

Figure 3.8: *Transconductance estimation using back-gate potential ramp.*

Reference step

The second method (Fig.3.9) consists of a step variation of the reference current (a certain percentage w.r.t. the previous I_{REF}), using a small number of samples to compute the differentiation and the average of the estimated transconductances. Since the response to the step is unknown before the tuning, we consider only the first samples in order to have an higher variation of current and voltage, so that it will be discernible from noise measurement.
Both these methods allow to autotune the PI gains regardless the condition of the EGOFET under test and they can be performed every time the system is in steady-state, ensuring that the imposed variations are clearly distinguishable from any other source of change.

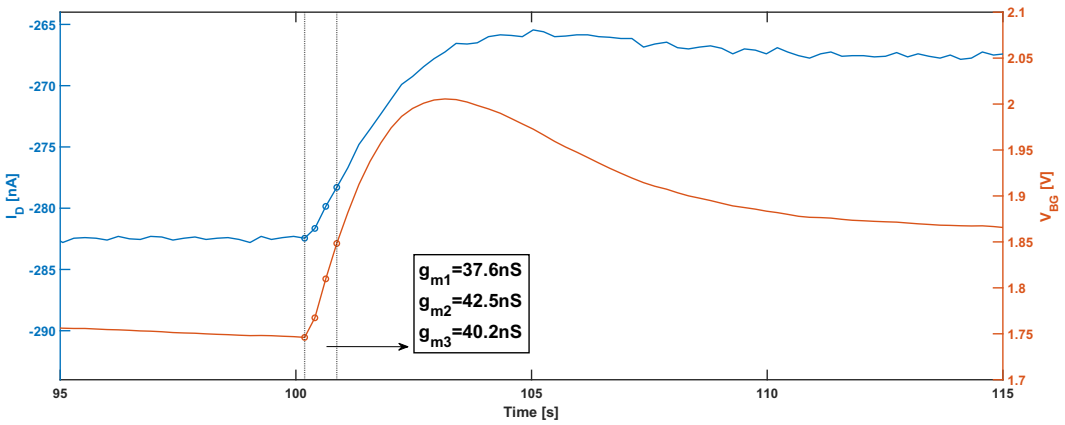

Figure 3.9: *Transconductance estimation using reference step.*

3.2.7 Action potential detection and feedforward

On this discussion, these devices are specifically considered for their application as electrical transducers of biological events such as the activity of cardiomyocyte cells. The stability required for this kind of test is guaranteed by the development of the digital control previously treated and the low voltage needed to avoid redox interference towards the biological event is made possible by the EGOFET structure. However some specific informations about the cell are demanded, since the more accurate the frequencies knowledge of the sensed activity is, the better the biological signal preservation will be. In order to give more robustness to the action potential sensing, we developed a detection and feedforward strategy to avoid the undesired compensation of useful signals.

Detection

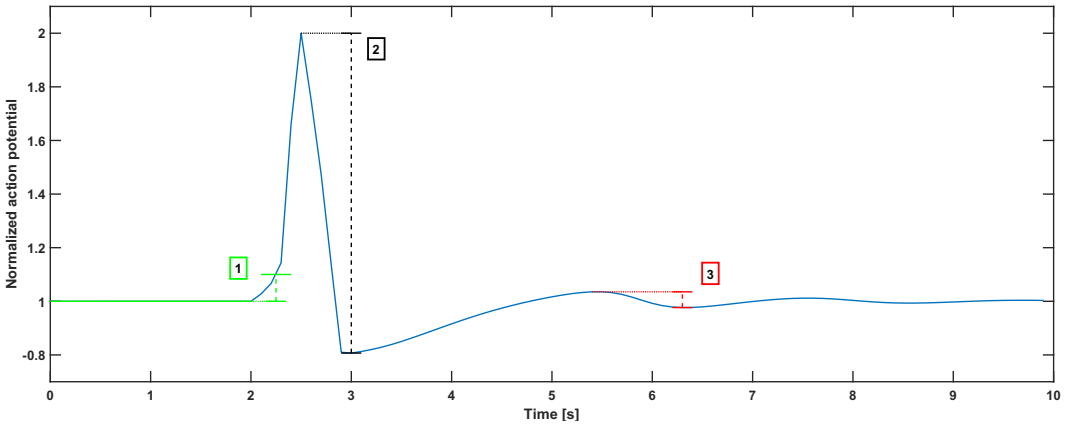

Figure 3.10: *1) Action potential detection 2) maximum peak-to-peak variation 3) peak-to-peak under threshold.*

The detection is based on a specific and recognizable expected shape of an action potential, consisting of an initial higher peak followed by a few variable

oscillations. Every time the value of the measured current exceeds the reference above a certain percentage (10% in Fig.3.10-1 in green), it is supposed that a cellular activity has begun with a good probability. Then, when the derivative of the current changes its sign, a peak is detected and its value is stored. After the first two collected peaks, the peak-to-peak variation is computed for each couple of consecutive peaks. The first and greatest one highlighted in black in Fig.3.10-2 is considered as the reference. When there is a peak-to-peak small enough w.r.t. the first one, the detection ends (6% in Fig.3.10-3 in red). Once the process starts, the feedforward control acts substituting the PI control for a minimum time $T_{hold-MIN}$ (Fig.3.11 in green). After that, it lasts until the detection ends or the maximum time $T_{hold-MAX}$ is reached (Fig.3.11 in red).

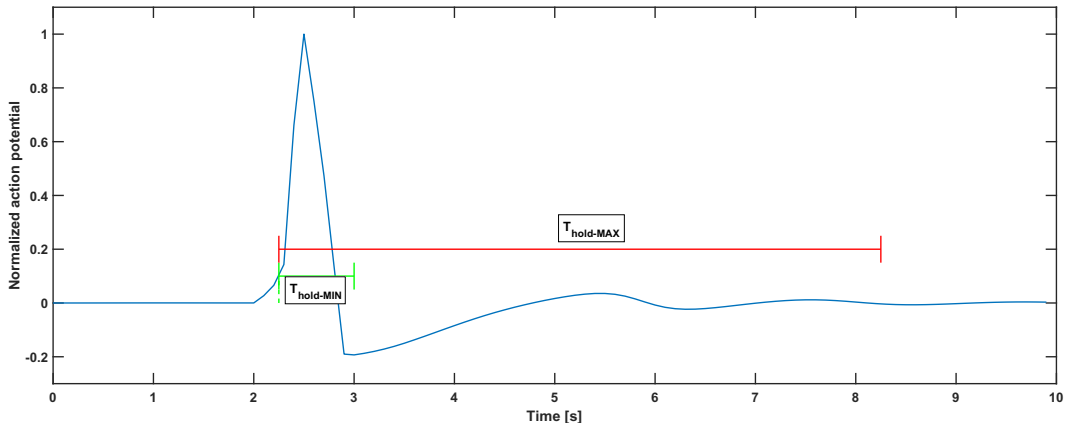

Figure 3.11: *Action potential detection: hold times.*

Feedforward

Since the current drift do not change abruptly its behaviour, when the PI controller is operating, the control variable trend $v_{BG}(t)$ can be exploited to predict the next back-gate potential value (only for a limited time), acting as feedforward term based on the previous knowledge of the disturbance. The slowness of the decay allows to implement the prediction by means of a linear fit $f(t)$ of the previous k samples:

$$v_{BG}(t_{i+1}) = m \cdot (t_i + T_s) + q \tag{3.2.25}$$

with $v_{BG}(t_{i-k}), ..., v_{BG}(t_i) \in f(t) = m \cdot t + q$.
In this way, the feedforward control can be used to substitute the PI action every time an action potential is detected. Therefore the preservation of the cell activity is consolidated by the proper operation of the detection and prediction strategy. Moreover the integral action can be reset when predictive control is enabled, acting as a wind-up strategy that avoid the saturation of the control. Once the action potential detection ends, the PI control resumes its operation, using the

last predicted value of v_{BG} to update the bias term $V_{BG0} = V_{BG0} + v_{BG}(t_{i+1})$.

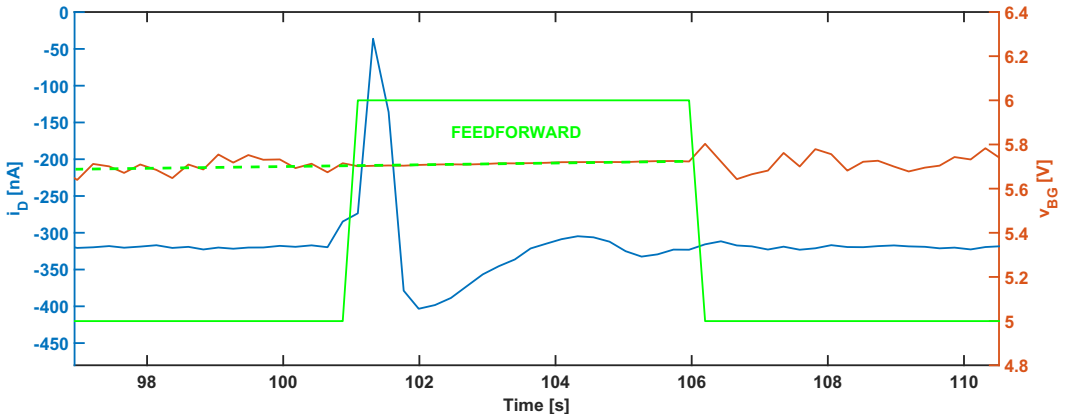

Figure 3.12: *Action potential detection: feedforward action.*

On Fig.3.12 in green is highlighted the period of time on which the feedforward control acts substituting the PI control. Dashed green line represents the linear fit of the previous value of v_{BG} (image from measurement on interdigitated lateral gate EGOFET).

3.3 Digital control: summary

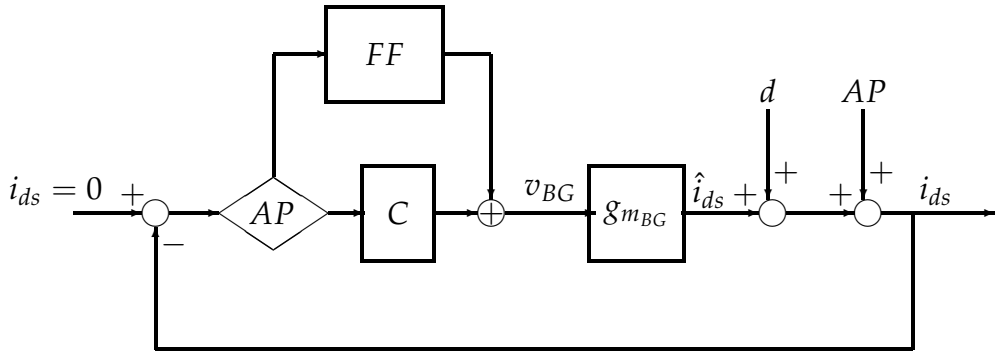

Figure 3.13: *Equivalent block diagram with feedforward.*

AP : Action potential detection

- Detection threshold.....10%I_{REF}
- End detection threshold.....6%$peak - to - peak_1$
- Minimum hold time.....750ms
- Maximum hold time.....6s

C : PI controller

- Crossing frequency.....0.628rad/s − 6.28rad/s
- Phase margin.....120°
- Autotuning PI gains.....v_{BG} $ramp$

FF : feedforward controller

- samples to fit.....37
- fit equation.....$m \cdot t + q$

EGOFET : DC bias parameters

- V_{TG}.....$-0.5V$
- V_{BG}.....$5V$
- V_{DS}.....$-0.5V$
- I_{REF}.....$initial\ i_{DS}$

SET-UP : instrumentation parameters

- Sampling time.....200ms

Chapter 4

Simulation and Results

In this chapter the simulations of the system and the digital control implemented are reported. The analysis begins from the Bode representation of the system blocks. Then, a MATLAB® script simulates the typical behaviour of the EGOFET and its response under feedback control, varying its parameters. Finally, the set-up developed has been tested on different devices. Similarities with the simulations are highlighted and the reliability of the system over time is shown.

4.1 Simulations and implementation

All the simulations have been performed using the following parameters:

Table 4.1: Simulation parameters.

Applied voltages	
V_{BG0} [V]	5
V_{TG} [V]	-0.5
V_{DS} [V]	-0.5

EGOFET parameters	
V_{th0} [V]	-0.26
W [μm]	8476
L [μm]	30
μ_{FET} $\left[\frac{cm^2}{sV^{\alpha+1}}\right]$	0.04

Capacitances	
C_{TG} [$\mu F/cm^2$]	4.6
C_{BG} [nF/cm^2]	16
C_{OSC} [$\mu F/cm^2$]	1.5

Recalling that $C_S = \left(\frac{1}{C_{BG}} + \frac{1}{C_{OSC}}\right)^{-1}$ and the eq.(3.2.24), the theoretical transconductance used on the simulations is $g_{m_{BG}} = 39.86nS$. The device is in saturation regime and the back-gate potential is biased to $5V$ in order to obtain more flexibility on the modulation range. The simulated EGOFET layout is based on the lateral gate structure, with typical threshold voltage and field-effect mobility values (table 4.1).

4.1.1 Frequency analysis

Throughout the frequencies of interest, the Bode diagram of the transconductance $g_{m_{BG}}$ is represented as a constant gain of $-148dB$ with null phase:

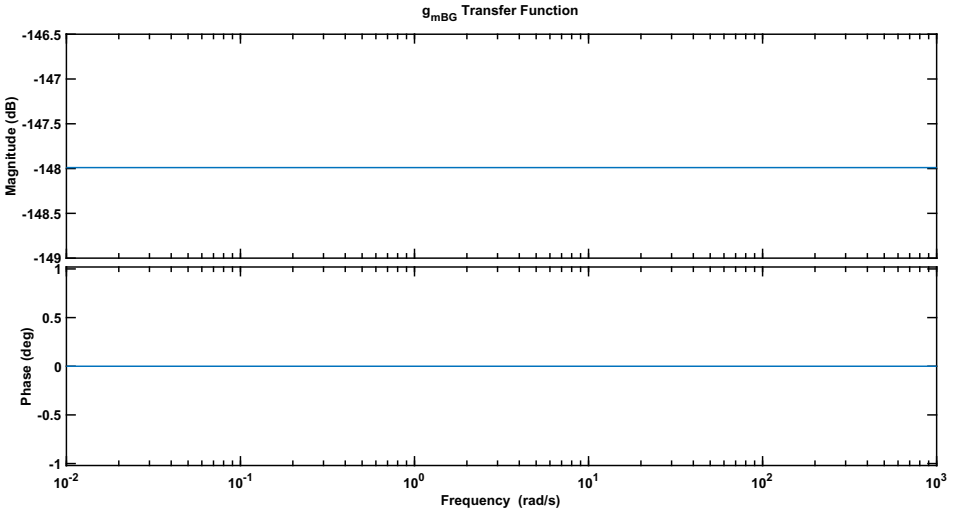

Figure 4.1: *Transconductance Bode diagram.*

By using the PI gains equations obtained on the previous chapter, with $K_P \geq 0$ for $\Phi_M \geq 90°$, the Bode diagrams of the controller varying Φ_M can be plotted:

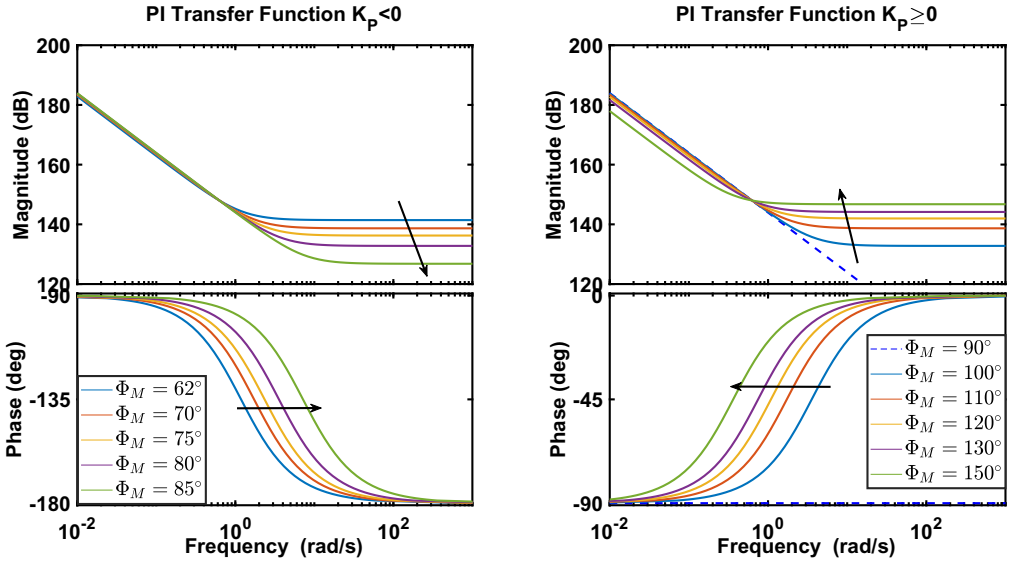

Figure 4.2: *PI controller Bode diagrams varying* Φ_M.

$$C(s) = K_P + \frac{K_I}{s} = K_I \frac{1 + s\tau_{PI}}{s} \tag{4.1.1}$$

The values of the PI gains are reported on the table (4.2):

Table 4.2: PI gains varying phase margin ($\omega_c = 0.628 rad/s$).

Φ_M [°]	K_P	K_I
62	$-1.1778 \cdot 10^7$	$1.3917 \cdot 10^7$
70	$-8.5804 \cdot 10^6$	$1.4812 \cdot 10^7$
75	$-6.4931 \cdot 10^6$	$1.5225 \cdot 10^7$
80	$-4.3564 \cdot 10^6$	$1.5523 \cdot 10^7$
85	$-2.1865 \cdot 10^6$	$1.5703 \cdot 10^7$
90	0	$1.5763 \cdot 10^7$
100	$4.3564 \cdot 10^6$	$1.5223 \cdot 10^7$
110	$8.5804 \cdot 10^6$	$1.4812 \cdot 10^7$
120	$1.2544 \cdot 10^7$	$1.3651 \cdot 10^7$
130	$1.6126 \cdot 10^7$	$1.2075 \cdot 10^7$
140	$1.9218 \cdot 10^7$	$1.0132 \cdot 10^7$
150	$2.1726 \cdot 10^7$	$7.8813 \cdot 10^6$

$$
\begin{aligned}
|K_P| &= \frac{1}{|g_{m_{BG}}|}\sqrt{1 - \frac{1}{1 + tan^2(\Phi_M + \beta)}} \\
|K_I| &= \frac{\omega_c}{|g_{m_{BG}}|}\frac{1}{\sqrt{1 + tan^2(\Phi_M + \beta)}}
\end{aligned}
\tag{4.1.2}
$$

where $\beta = -\frac{\pi}{2}$, K_I always positive and $K_P > 0$ for $\Phi_M > 90°$, negative otherwise.

The compensated closed loop transfer function is defined as:

$$
W(s) = \frac{g_{m_{BG}} C(s)}{1 + g_{m_{BG}} C(s)} \tag{4.1.3}
$$

The relative Bode diagrams varying Φ_M are shown on Fig.4.3.

The crossing frequency used as standard reference is $\omega_c = 0.628 rad/s$, since it is a good trade-off between disturbance rejection and action potential preservation.

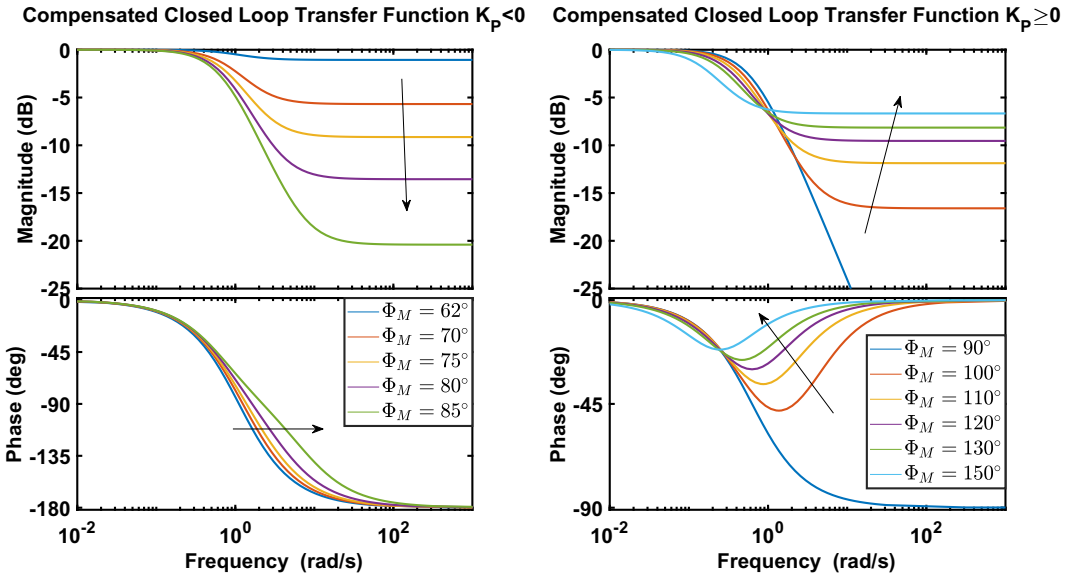

Figure 4.3: *Compensated closed loop Bode diagrams varying* Φ_M.

4.1.2 Simulink® and algorithm implementation

The behaviour of the device has been first simulated by using Simulink® model. Then, it has been implemented through a MATLAB® script, that constitutes the base of the code used for the actual operation.

Simulink®

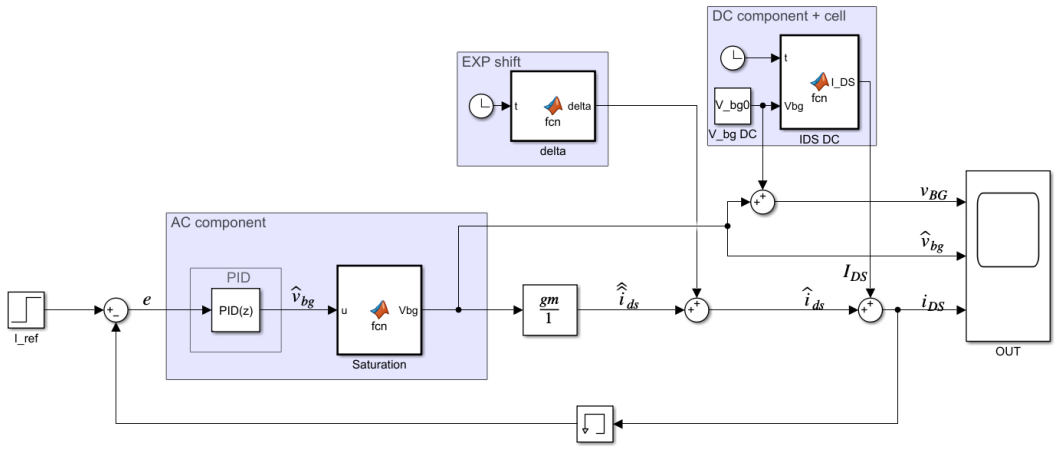

Figure 4.4: *Simulink® model of EGOFET with output disturbance and cell signal.*

The *"PID(z)"* block represent the eq.(4.1.1) discretized by Tustin approach, as described in the previous chapter. The *"saturation"* block implement the maximum sustainable values of V_{BG} and $\frac{gm}{1}$ is the back-gate transconductance based on the parameters of table 4.1. The output disturbance is given as an additional signal from the block *"delta"* equal to $h_m \Delta V e^{-\frac{t}{\tau}}$. The *"DC component + cell"* block provides the constant value of I_{DS} generated from the parameters of

the EGOFET, with a superimposed cell signal based on the periodical repetition of the simulated action potential applied as V_{TG}. The reference signal is given by *"I_ref"*, starting from the initial value of I_{DS} and introducing a step variation after half of the simulation. Since the instrumentation used to measure the device is controlled by a MATLAB® script, once verified the system behaviour, the simulation has been transposed into an algorithm.

Algorithm

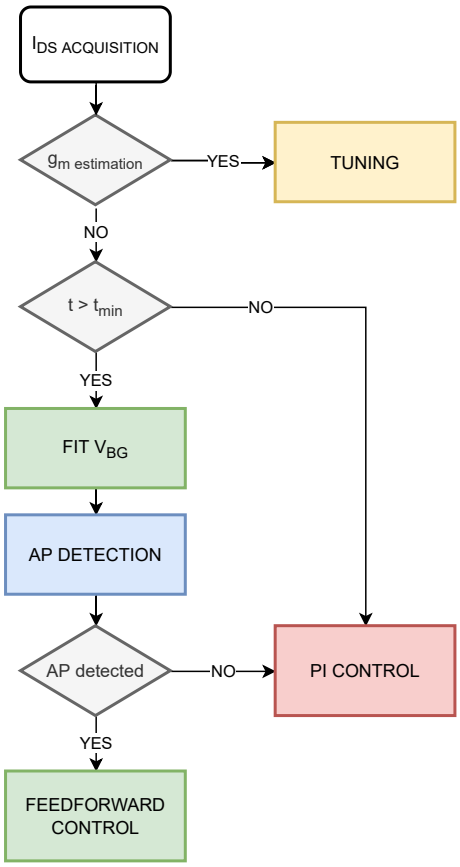

Figure 4.5: *Flowchart of the measure loop algorithm.*

The algorithm of a loop is described by the flowchart in Fig.4.5. The transconductance estimation and the consequent tuning of the PI gains are implemented only on the actual code used for the measurements. There is a minimum setting time t_{min}, during which the action potential detection and the fit of the back-gate potential are disabled. This precaution allows to check that the device is operating correctly and that steady-state is reached, as well as to perform autotuning procedures. In the simulations, the value of I_{ds} at each instant t_i is computed following the linearized model defined in the previous chapter:

$$I_{ds}(t_i) = I_{DS}(t_i) + v_{bg}(t_i) \cdot g_{m_{BG}} + d(t_i) + AP(t_i) \tag{4.1.4}$$

where I_{DS} is the DC component of the current, based on the parameters of

table 4.1, v_{bg} represent the control variable computed at each loop, d is the exponential drift and AP is the action potential generated applying the signal on Fig.3.4 as V_{GS} on eq.3.1.5.

TUNING: the tuning block operates every time a new estimation of the EGOFET transconductance (and PI gains) is required, as long as the system is in steady-state. There are two variants of the algorithm: V_{BG} ramp tuning and I_{REF} step tuning. The first one, that has been adopted for all the measures on the device, is described by the following pseudocode:

Algorithm 1 V_{BG} Ramp Tuning Algorithm

t0 ← tuning starting time
t1 ← t0 + Δv_{BG} rise time
t2 ← t1 + Δv_{BG} fall time
$\Delta v_{BG} \leftarrow \Delta v_{BG_{max}} \cdot \frac{T_s}{t1-t0}$ $\left(\Delta v_{BG_{max}} \cdot \frac{T_s}{t2-t1}\right)$
if t0 $< t_i <$ t1 **then**
    $v_{BG} \leftarrow v_{BG} + \Delta v_{BG}$
    compute $g_{m_{BG_i}} = \left|\frac{\delta I_{ds}}{\delta v_{BG}}\right|$
else if t1 $< t_i <$ t2 **then**
    $v_{BG} \leftarrow v_{BG} - \Delta v_{BG}$
    compute $g_{m_{BG_i}} = \left|\frac{\delta I_{ds}}{\delta v_{BG}}\right|$
end if
$g_{m_{BG}} \leftarrow$ mean $\sum g_{m_{BG_i}}$

The second one, with a reference variation of 5%, is:

Algorithm 2 I_{REF} Step Tuning Algorithm

t0 ← tuning starting time
$\Delta I_{REF} \leftarrow I_{REF} \cdot 5\%$
if $t_i >$ t0 **then**
    $I_{REF} \leftarrow I_{REF} - \Delta I_{REF}$
    for 3 next samples compute $g_{m_{BG_i}} = \left|\frac{\delta I_{ds}}{\delta v_{BG}}\right|$
end if
$g_{m_{BG}} \leftarrow$ mean $\sum g_{m_{BG_i}}$

After the evaluation of the transconductance, the PI gains are computed by means of eq.(4.1.2). Then, the algorithm proceeds with the digital control.

FIT V_{BG}: after the initial setting time t_{min}, a certain number of samples of the control variable trend are fitted by means of a linear fit $f(t) = m \cdot t + q$. The length of the fit is chosen according to the period of the cell signal, in order to consider only back-gate variations that counteract the current drift (Algorithm 3).

Algorithm 3 Fit $\mathbf{V_{BG}}$ Algorithm

1: $t_i \leftarrow$ fit starting time
2: $t_{i-k} \leftarrow t_i - T_{cell}/2$
3: m,q $\leftarrow$ linear fit $v_{BG}(t_{i-k}...t_i)$

FEEDFORWARD: when an action potential is detected, the back-gate potential value computed by the fit is applied to the device, instead of the PI control output and the initial bias V_{BG0} is updated (Algorithm 4).

Algorithm 4 Feedforward Algorithm

1: $T_s \leftarrow t_i - t_{i-1}$
2: $v_{BG_{i+1}} \leftarrow m \cdot (t_i + T_s) + q$
3: $V_{BG0} \leftarrow v_{BG_{i+1}}$

PI CONTROL: the main block of the digital control is the PI controller, that is implemented as follow:

Algorithm 5 PI Control Algorithm

1: $e_i \leftarrow i_{DS} - I_{REF}$ error computed on the current iteration
2: $e_{i-1} \leftarrow$ error computed on the previous iteration
3: $u_P \leftarrow K_P \cdot e_i$
4: $u_I \leftarrow K_I \frac{T_s}{2} \cdot (e_i + e_{i-1}) + u_I$
5: $u \leftarrow u_P + u_I$
6: $v_{BG_{i+1}} \leftarrow u + V_{BG0}$

The values of v_{BG} computed by both the PI control and the feedforward are subjected to a check to ensure that they do not exceed the saturation limit values set out in the subsection 3.2.5.

AP DETECTION: the detection of the action potential has to fulfill several conditions to ensure the correctness of the recording. This block checks if the current sample belongs to an actual action potential (AP detected $\leftarrow$ **true**) or not (AP detected $\leftarrow$ **false**). The current threshold to activate the detection is set to $1.1 \cdot I_{REF}$. Minimum and maximum hold times are implemented. A sample is considered a peak if the derivative of the current change its sign between consecutive couples of samples. The minimum peak-to-peak that stops the detection is equal to 6% of the first one. According to the result of this block, the corresponding digital control is used. The pseudocode is reported in Algorithm 6.

Algorithm 6 Action Potential Detection Algorithm

if AP not already detected **then**
  if $i_{DS_i} - i_{DS_{i-1}} > 1.1 \cdot I_{REF}$ **then**
    AP detected $\leftarrow$ **true**
    $T_{start} \leftarrow t_i$
  else
    AP detected $\leftarrow$ **false**
  end if
end if
if $t_i > T_{start} + T_{hold-MAX}$ **then**
  AP detected $\leftarrow$ **false**
end if
if $t_i < T_{start} + T_{hold-MIN}$ **then**
  check and store eventual peak
  AP detected $\leftarrow$ **true**
else
  check and store eventual peak
  compute peak-to-peak
  if peak-to-peak<6%(first peak-to-peak) **then**
    AP detected $\leftarrow$ **false**
  else
    AP detected $\leftarrow$ **true**
  end if
end if

Measurement set-up

The algorithm previously defined has been implemented into a measurement set-up made up by an Agilent B1500 parameter analyzer controlled by a Desktop Computer (by using MATLAB®), to set the potentials and measure the currents on the drain, source and back-gate electrodes. The top-gate has been controlled by the same parameter analyzer during the experiments to test the digital control performances. In order to simulate the action potential signal, it has been substituted by a Rigol DG1000 arbitrary waveform generator. The scheme of this implementation is shown in Fig.4.6, where *A* represents the measurement part of the instrument:

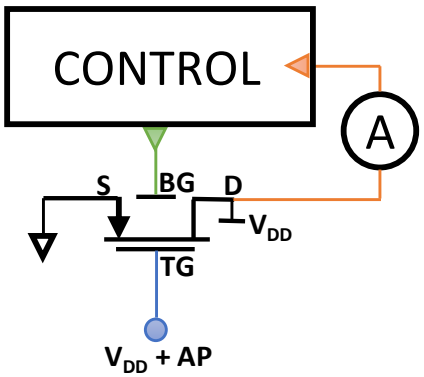

Figure 4.6: *Digital control set-up.*

4.1.3 Simulation results

The following simulations have been performed by using MATLAB® algorithm previously descripted, varying Φ_M and ω_c, with and without the cell signal (AP) and the feedforward control. Parameters are reported on table 4.1, with sampling time $T_s = 200ms$ (digital control carried out at each sample). The output disturbance has been considered as a stretched exponential decay:

$$d(t) = h_m e^{-\left(\frac{t}{\tau}\right)^{\beta}} \tag{4.1.5}$$

h_m defined in eq.3.1.9, $\Delta V = 0.01V$, $\tau = 10$, $\beta = 0.3$.
The reference DC current is set to the initial i_{DS} value of the device (eq.(3.1.7 with $t = 0$). After half of the simulation, it is increased by 5%, in order to observe the step response. The phase margins are provided on table 4.2, with the corresponding PI gains. The graphs show the behaviour of the output current $i_{DS}(t)$ and the control variable $v_{BG}(t)$, highlighting the response on some points of interest. Solid lines represent $\Phi_M > 90°$ (positive K_P), dotted lines $\Phi_M < 90°$ (negative K_P) and black line $\Phi_M = 90°$ ($K_P = 0$).

- **Simulation 1:**
  $\omega_c = 0.628rad/s$ - saturation limit off
- **Simulation 2:**
  $\omega_c = 0.628rad/s$ - saturation limit on
- **Simulation 3:**
  $\omega_c = 0.628rad/s$ - saturation limit off- $\Delta V = -0.01V$
- **Simulation 4:**
  $\omega_c = 0.628rad/s$ - saturation limit on - $\Delta V = -0.01V$

In these simulations the effectivness of the digital control counteracting the output disturbance is shown. The result is optimal with both positive (Sim.1 and Sim.2) and negative (Sim.3 and Sim.4) current drift. In Sim.2 and Sim.4 the saturation limit on Δv_{BG} is enabled and it does not affect the reference tracking at start. From dotted lines it can be clearly observed the positive feedback effect of phase margins less than 90°, where the output initially follows the current drift, and then quickly backs up to the reference. During the step response the same behaviour is observable. Decreasing the phase margin the initial undershoot increase, but the reference tracking is faster. For $\Phi_M > 90°$ the response is slightly slower and increasing the magnitude of K_P, the promptness of the control effect causes some oscillation. When the saturation limit is enabled, higher phase margins are required to avoid oscillations and compensate the introduced delay (better results with $\Phi_M = 120° - 130°$).

Simulation 1

$\omega_c = 0.628 rad/s$ - saturation limit off

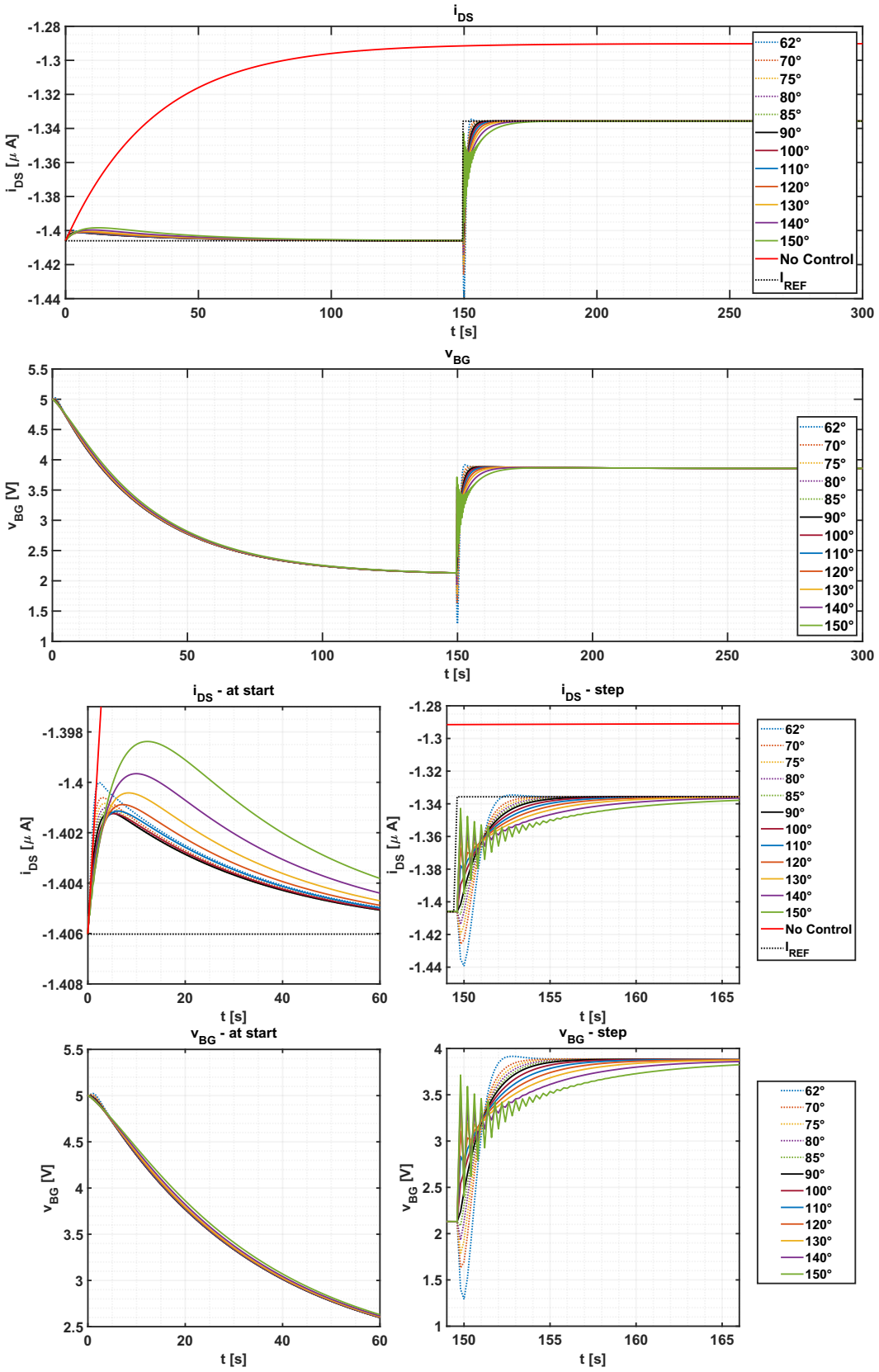

Figure 4.7: *Simulation 1 varying* Φ_M.

Simulation 2

$\omega_c = 0.628 rad/s$ - saturation limit on

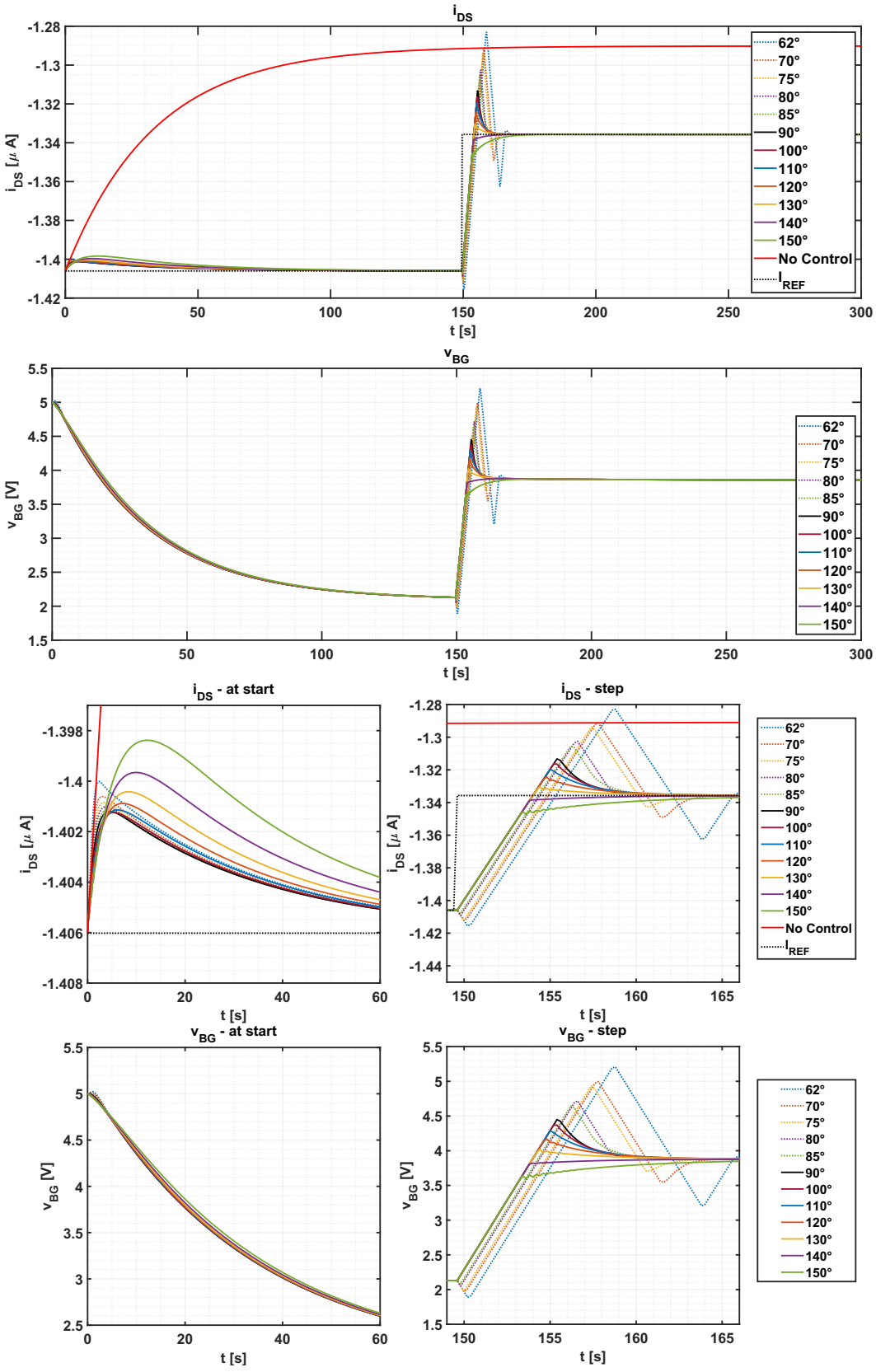

Figure 4.8: *Simulation 2 varying* Φ_M.

Simulation 3

$\omega_c = 0.628 rad/s$ - saturation limit off- $\Delta V = -0.01V$

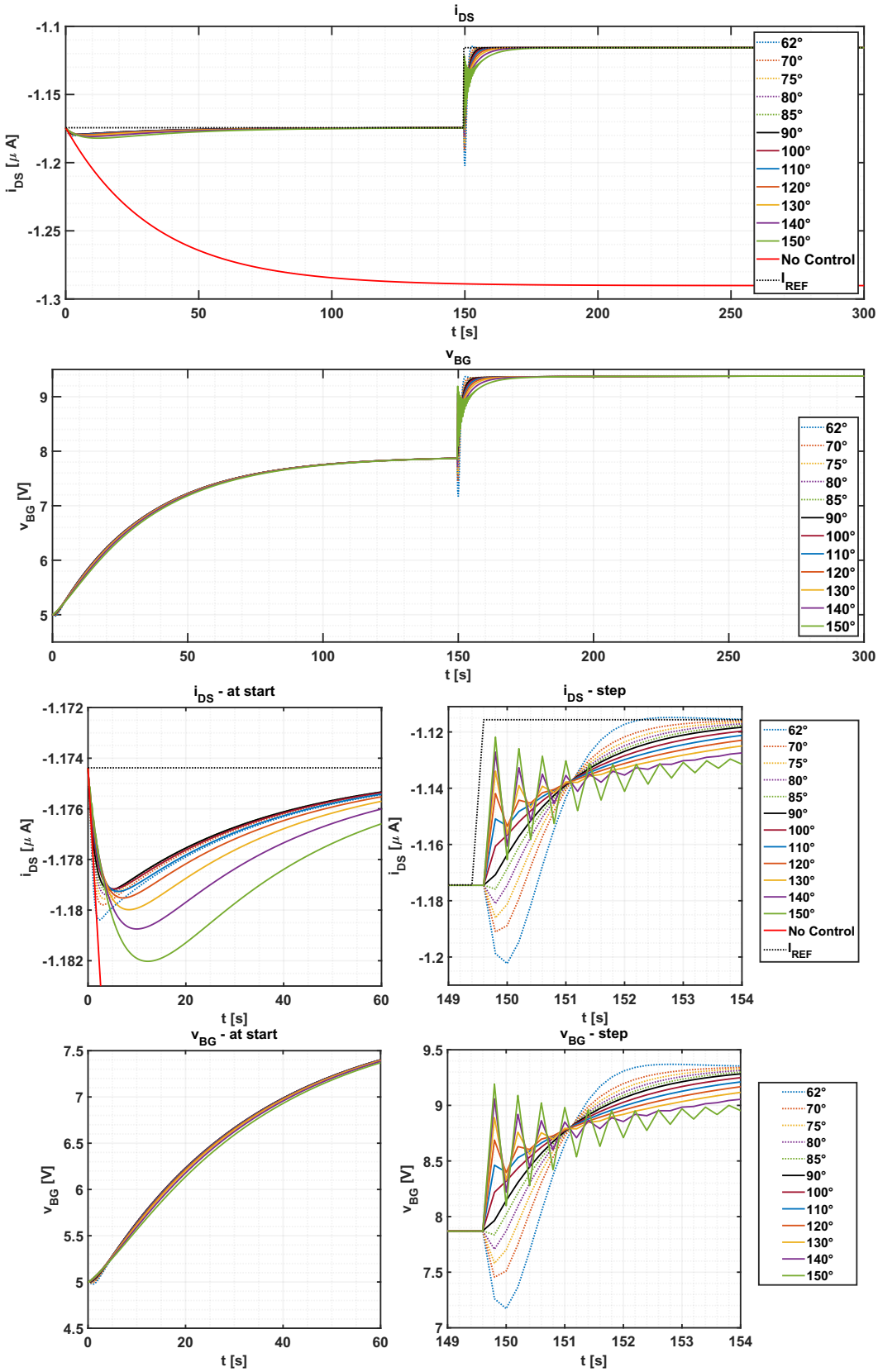

Figure 4.9: *Simulation 3 varying* Φ_M.

Simulation 4

$\omega_c = 0.628 rad/s$ - saturation limit on - $\Delta V = -0.01V$

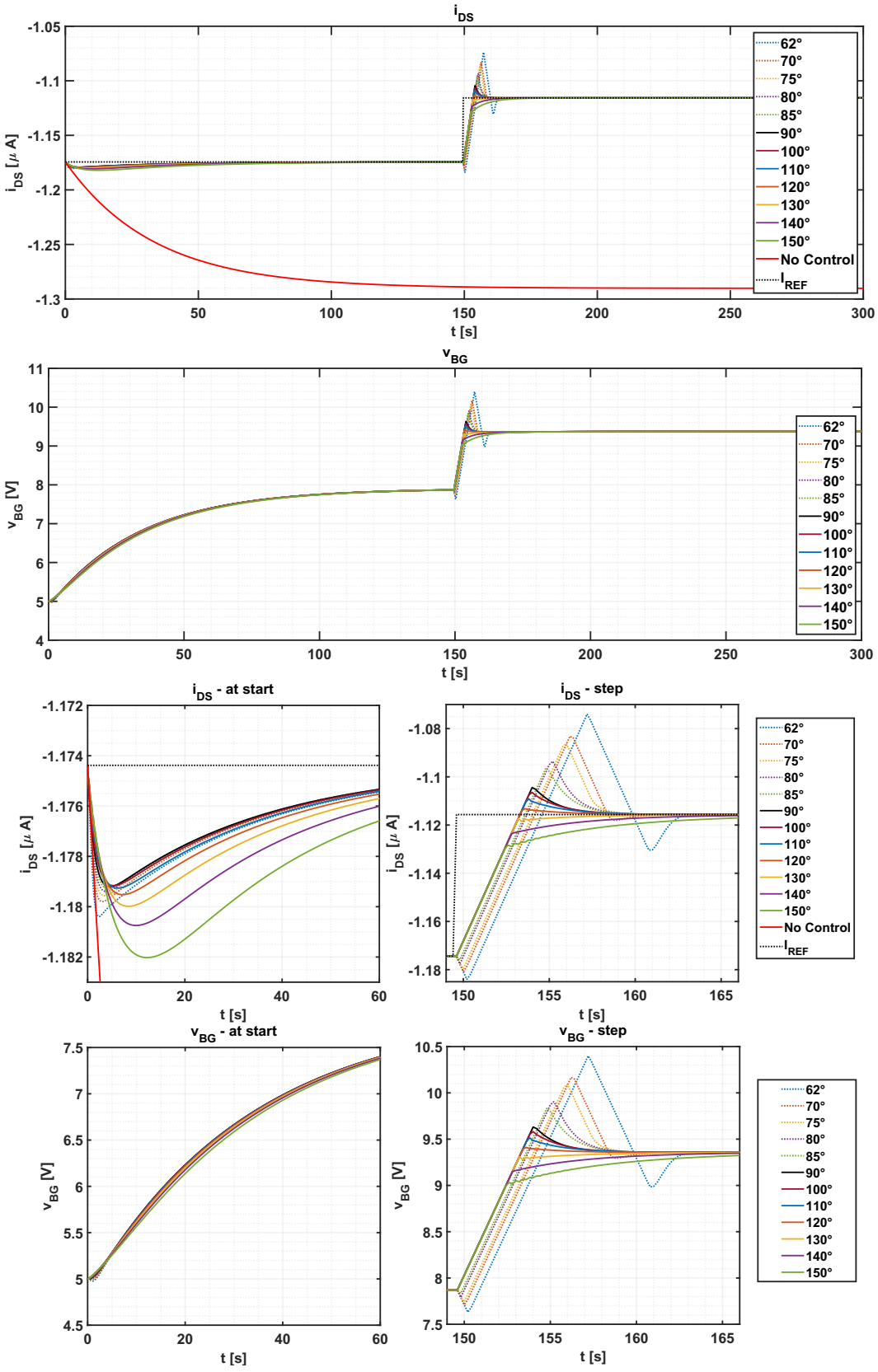

Figure 4.10: *Simulation 4 varying* Φ_M.

- **Simulation 5:**

$$\omega_c = 0.0628 rad/s \text{ - saturation limit off}$$

- **Simulation 6:**

$$\omega_c = 0.0628 rad/s \text{ - saturation limit on}$$

In Sim.5 and Sim.6 the crossing frequency is reduced by a factor of 10. As discussed in the previous chapter, at this ω_c an hypothetical action potential will be well preserved, however the output disturbance will not completely be filtered. This can be observed on Fig.4.11 and Fig.4.12, where the reference tracking is much slower than in the previous case.

Simulation 5
$\omega_c = 0.0628 rad/s$ - saturation limit off

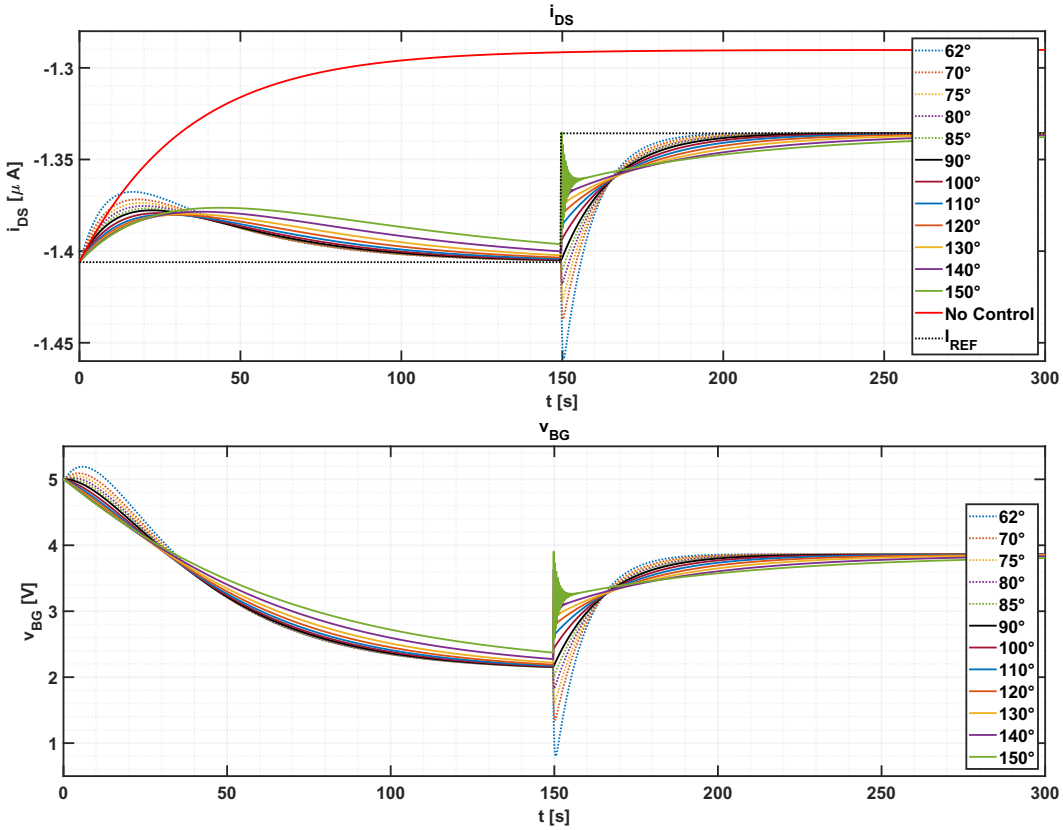

Figure 4.11: *Simulation 5 varying Φ_M: $\omega_c = 0.0628 rad/s$.*

This crossing frequency cannot be implemented in real applications since the response of the system is too slow.

Simulation 6

$\omega_c = 0.0628 rad/s$ - saturation limit on

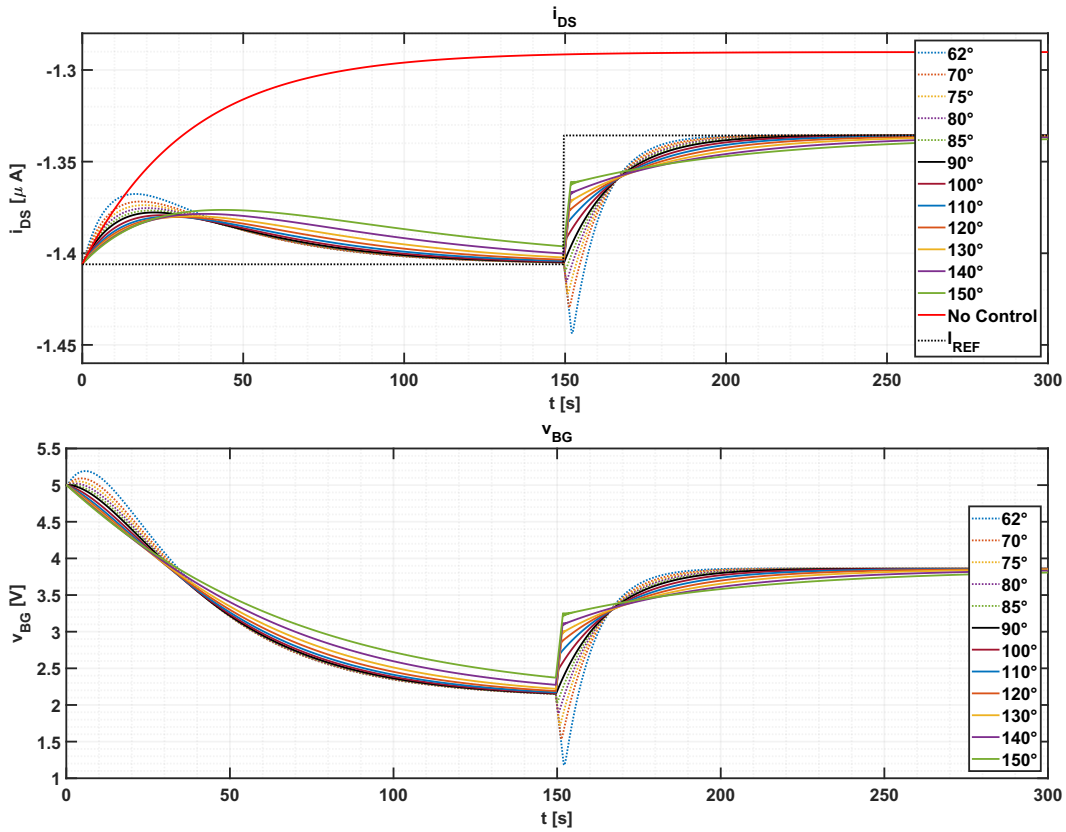

Figure 4.12: *Simulation 6 varying Φ_M: $\omega_c = 0.0628 rad/s$ + saturation.*

- **Simulation 7:**

  $\omega_c = 6.28 rad/s$ - saturation limit off

- **Simulation 8:**

  $\omega_c = 6.28 rad/s$ - saturation limit on

In Sim.7 and Sim.8 the crossing frequency is 10 times higher than the standard one. Phase margins less than $\Phi_M = 90°$ lead the system towards instability. Recalling the discretization approach described in subsection 3.2.4, there is an implicit distortion due to the high crossing frequency w.r.t. the sampling frequency. Increasing the phase margin, this effect is attenuated and the response of the system is faster, as figured in Fig.4.13 $i_{DS} - step$, where better result are obtained with $\Phi_M \geq 120°$. In Sim.8 (Fig.4.14) the trend is confirmed, but is difficult to apply on real experiments as the limit on the derivative of v_{BG} produces strong initial oscillations.

Simulation 7
$\omega_c = 6.28 rad/s$ - saturation limit off

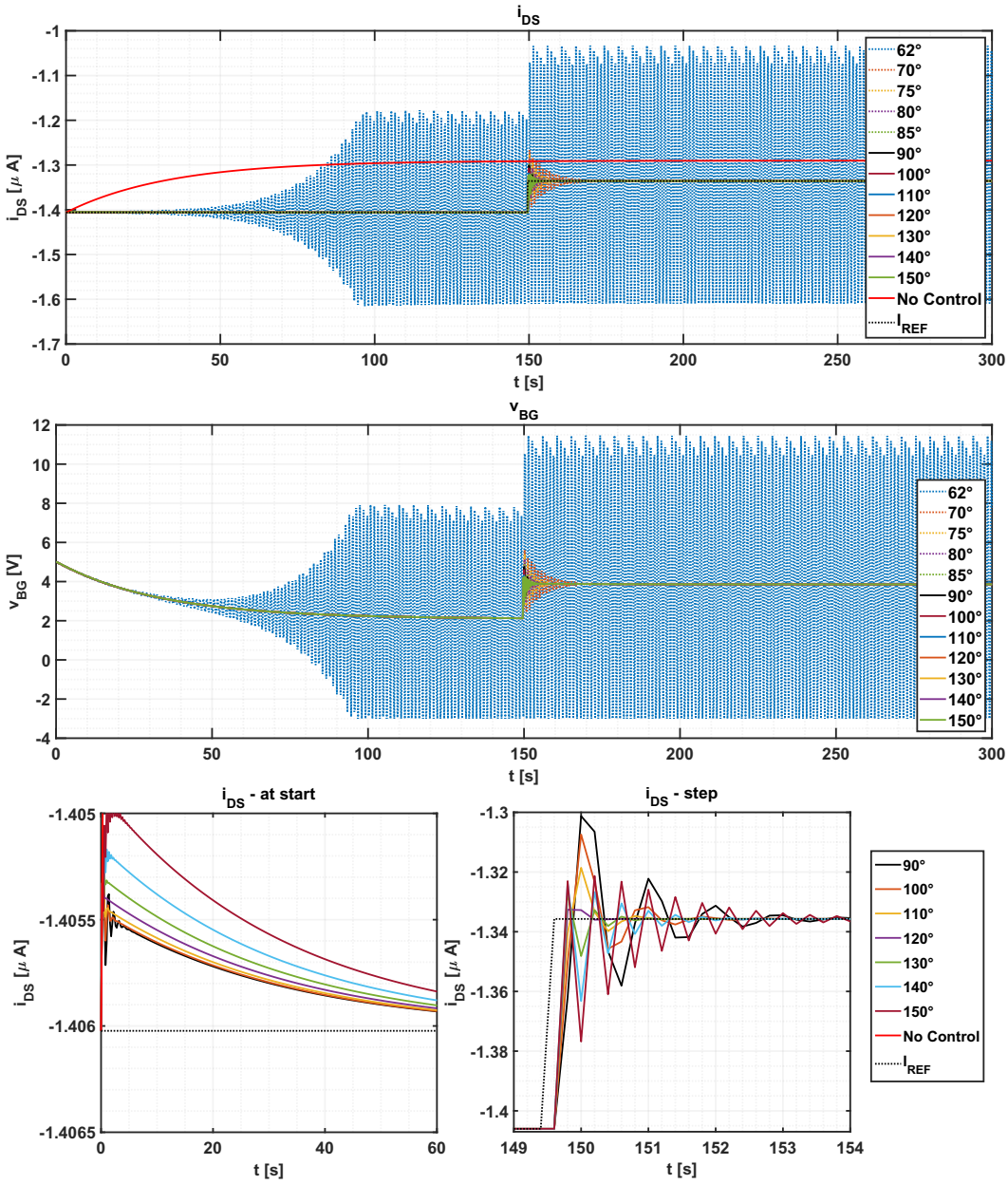

Figure 4.13: *Simulation 7 varying Φ_M: $\omega_c = 6.28 rad/s$.*

Simulation 8:
$\omega_c = 6.28 rad/s$ - saturation limit on

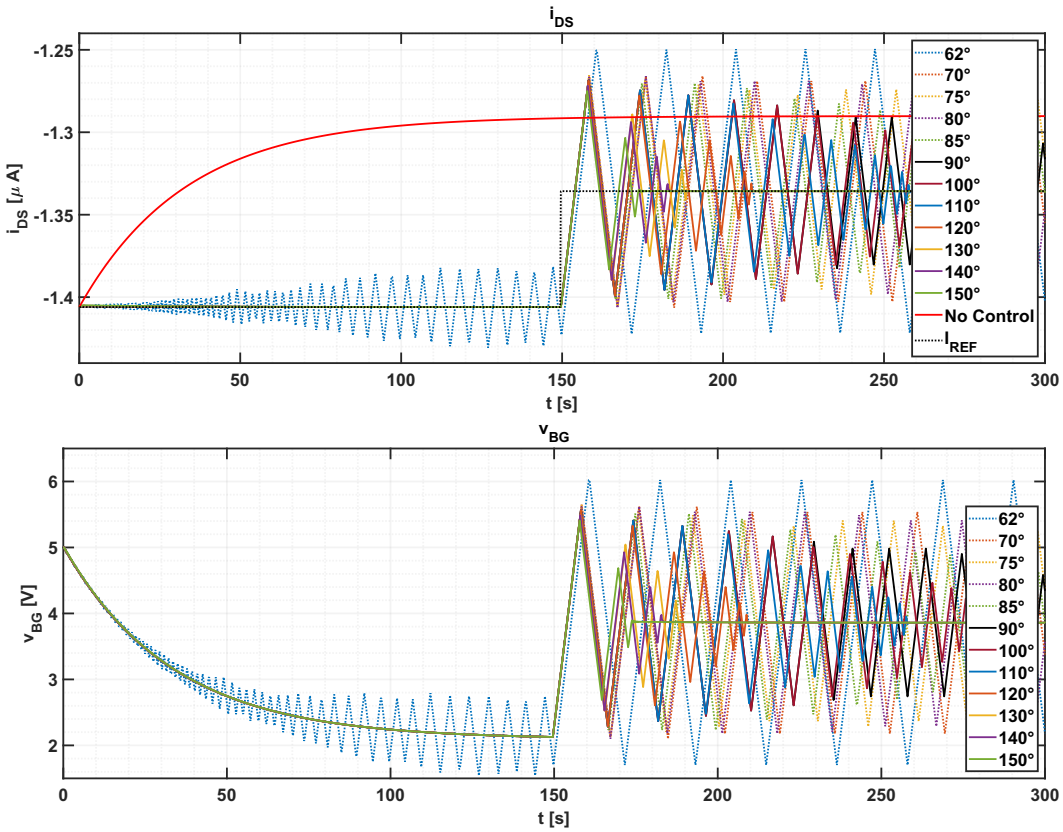

Figure 4.14: *Simulation 8 varying Φ_M: $\omega_c = 6.28 rad/s$ + saturation.*

- **Simulation 9:**
  $\omega_c = 0.628 rad/s$ - saturation limit off - Action Potential - Feedforward off
- **Simulation 10:**
  $\omega_c = 0.628 rad/s$ - saturation limit on - Action Potential - Feedforward off
- **Simulation 11:**
  $\omega_c = 0.628 rad/s$ - saturation limit on - Action Potential - Feedforward on

In Sim.9 and Sim.10 an action potential signal is superimposed to the output current. The shape of the sensed signal is sufficiently preserved (especially with higher phase margins) in both the simulations, with better results when the saturation limit is enabled. In fact the limit on the derivative of Δv_{BG} partly overcomes the slowness of the sampling rate, avoiding extra compensations. Since Sim.9 is unsuitable in real cases, the information about the action potential cannot be achieved by the back-gate potential, even if the sampling time is sufficiently decreased. In Sim.11 the feedforward control is enabled and the cyan lines highlight the detected action potentials. Until the reference step, the response is identical for all the tested phase margins. Then, only $\Phi_M \geq 90°$ are still useful for real implementation.

Simulation 9

$\omega_c = 0.628 rad/s$ - saturation limit off - Action Potential - Feedforward off

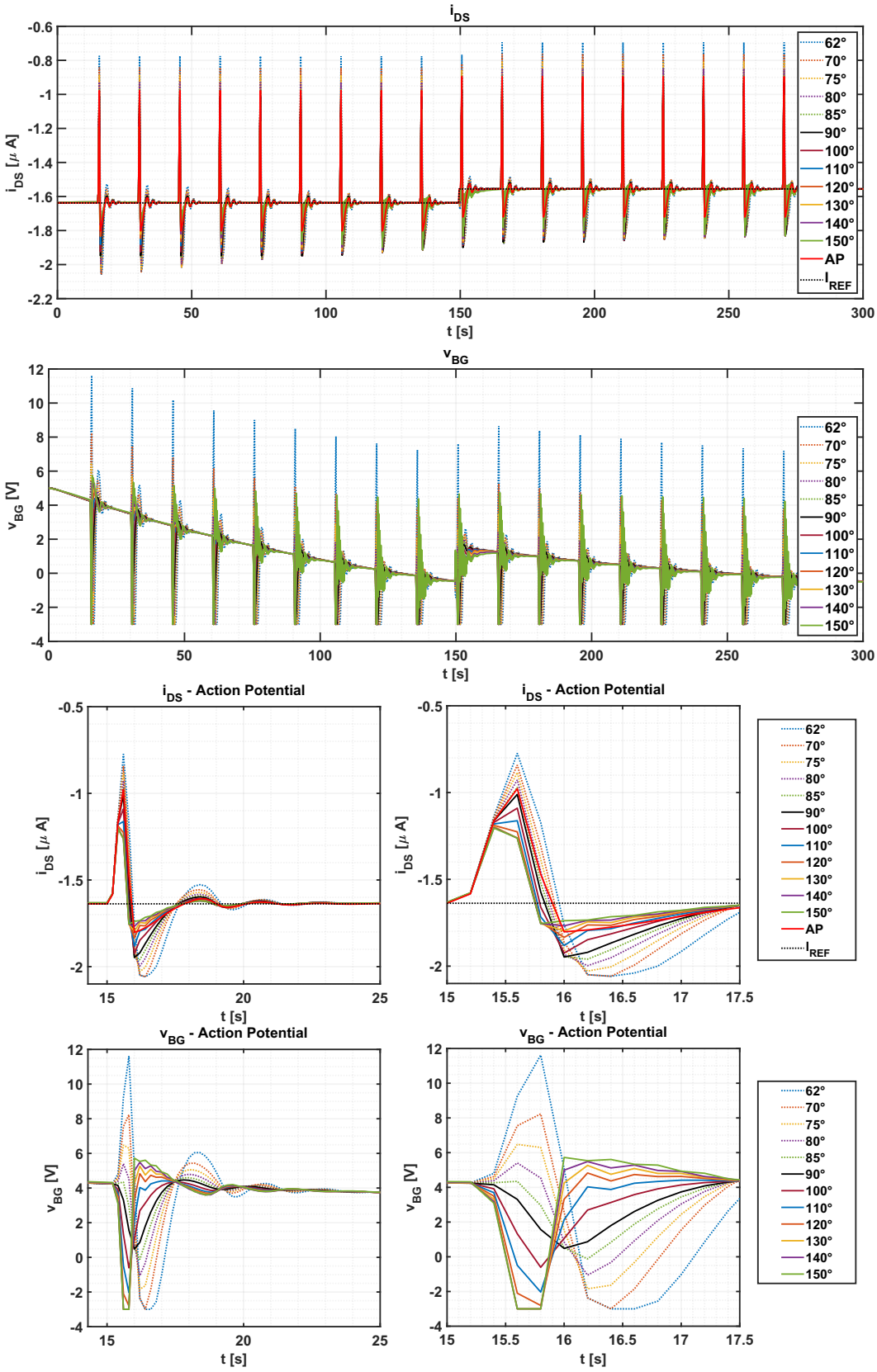

Figure 4.15: *Simulation 9 varying Φ_M: AP sensing $\omega_c = 0.628 rad/s$.*

Simulation 10

$\omega_c = 0.628 rad/s$ - saturation limit on - Action Potential - Feedforward off

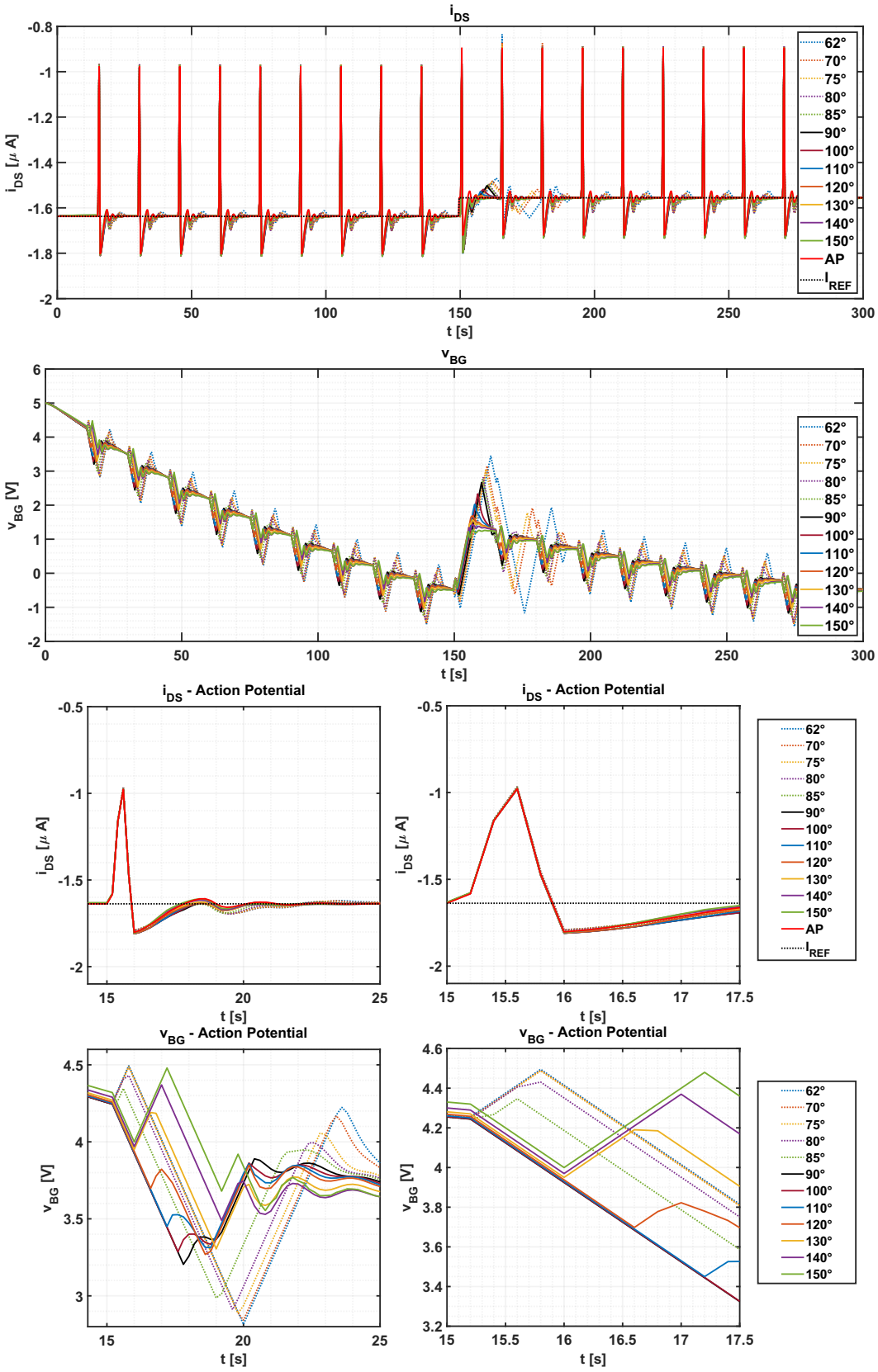

Figure 4.16: *Simulation 10 varying Φ_M: AP sensing $\omega_c = 0.628 rad/s$ + saturation.*

Simulation 11

$\omega_c = 0.628 rad/s$ - saturation limit on - Action Potential - Feedforward on

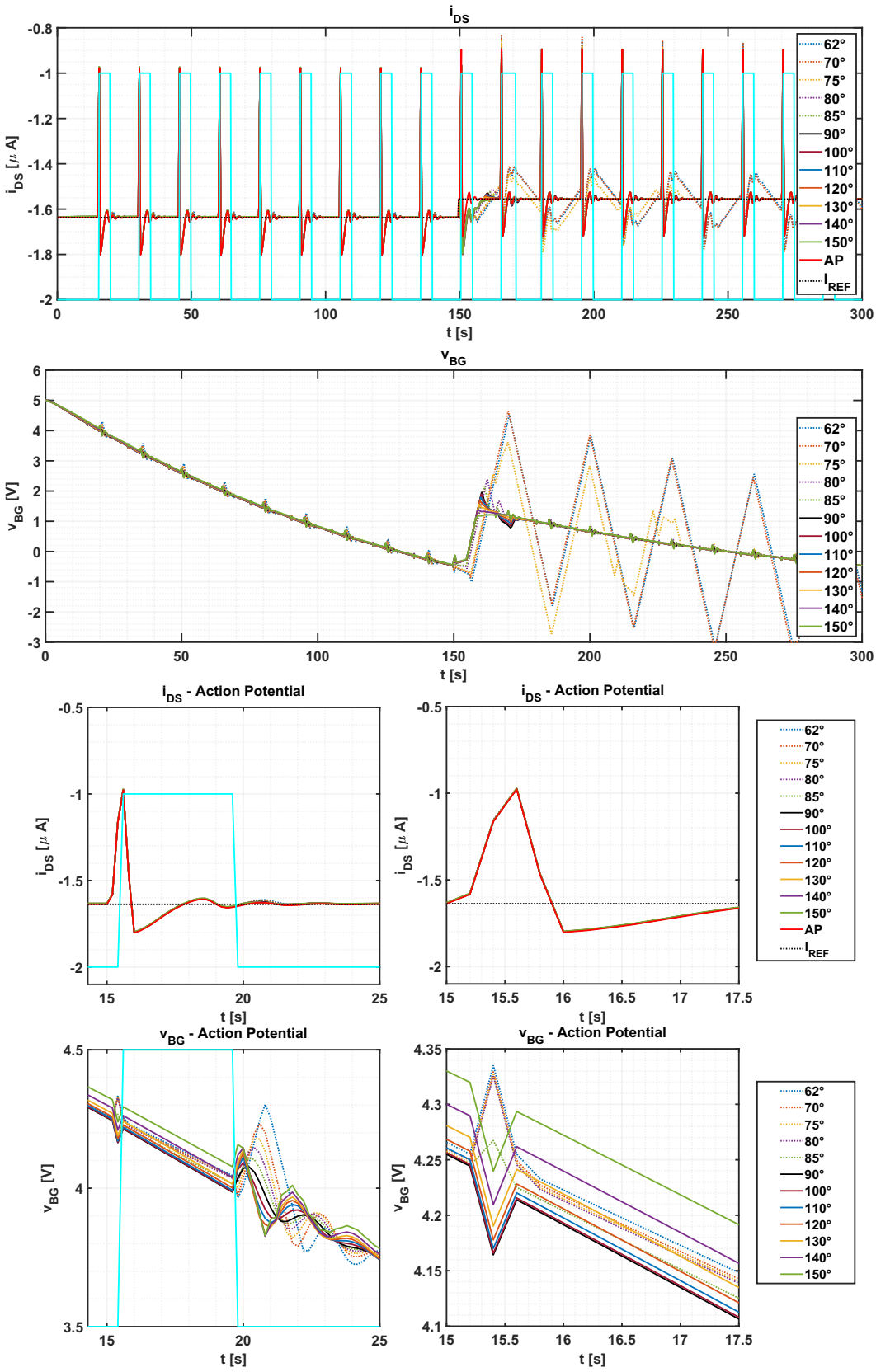

Figure 4.17: *Simulation 11 varying Φ_M: AP sensing $\omega_c = 0.628 rad/s$ + saturation + Feedforward.*

- **Simulation 12:**
  $\omega_c = 6.28 rad/s$ - saturation limit off - Action Potential - Feedforward off
- **Simulation 13:**
  $\omega_c = 6.28 rad/s$ - saturation limit on - Action Potential - Feedforward off
- **Simulation 14:**
  $\omega_c = 6.28 rad/s$ - saturation limit on - Action Potential - Feedforward on

Increasing the crossing frequency, the positive feedback surely cannot be implemented (Sim.12 Fig.4.19), as well as the whole range of phase margins with saturation limit enabled (Sim.13 Fig.4.20). Over time the response becomes increasingly unstable and the signal less recognisable. The feedforward controller combined with a tuned PI controller with sufficiently large phase margins ($\Phi_M \geq 120^c irc$) can overcome these issues, as it is observable in Fig.4.21.
In conclusion, the better results are obtained with the action potential detection and Feedforward control enabled, with Φ_M around 120°. Under these circumstances, the choice of ω_c depends on the task to accomplish. In order to have faster rejection of the current drift $\omega_c = 6.28 rad/s$ is the better choice, if it is required more stability $\omega_c = 0.628 rad/s$ is preferred (Fig.4.18).

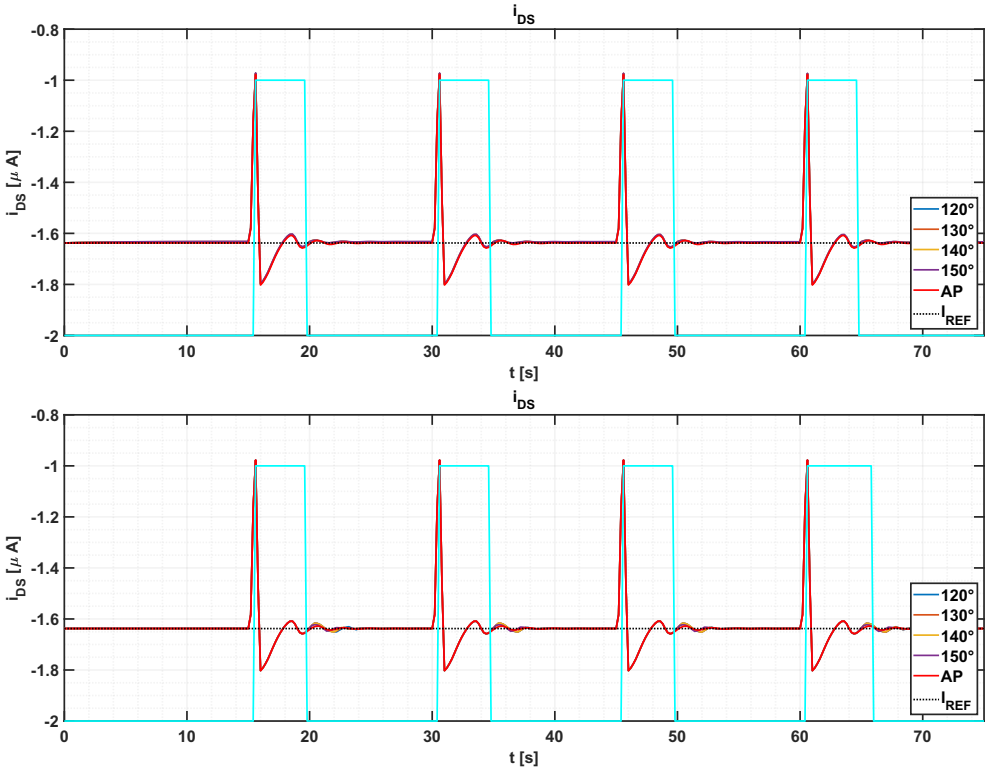

Figure 4.18: *Simulation 11 and Simulation 14 varying Φ_M: Action Potential sensing 1) $\omega_c = 0.628 rad/s$ 2) $\omega_c = 6.28 rad/s$.*

Simulation 12

$\omega_c = 6.28 rad/s$ - saturation limit off - Action Potential - Feedforward off

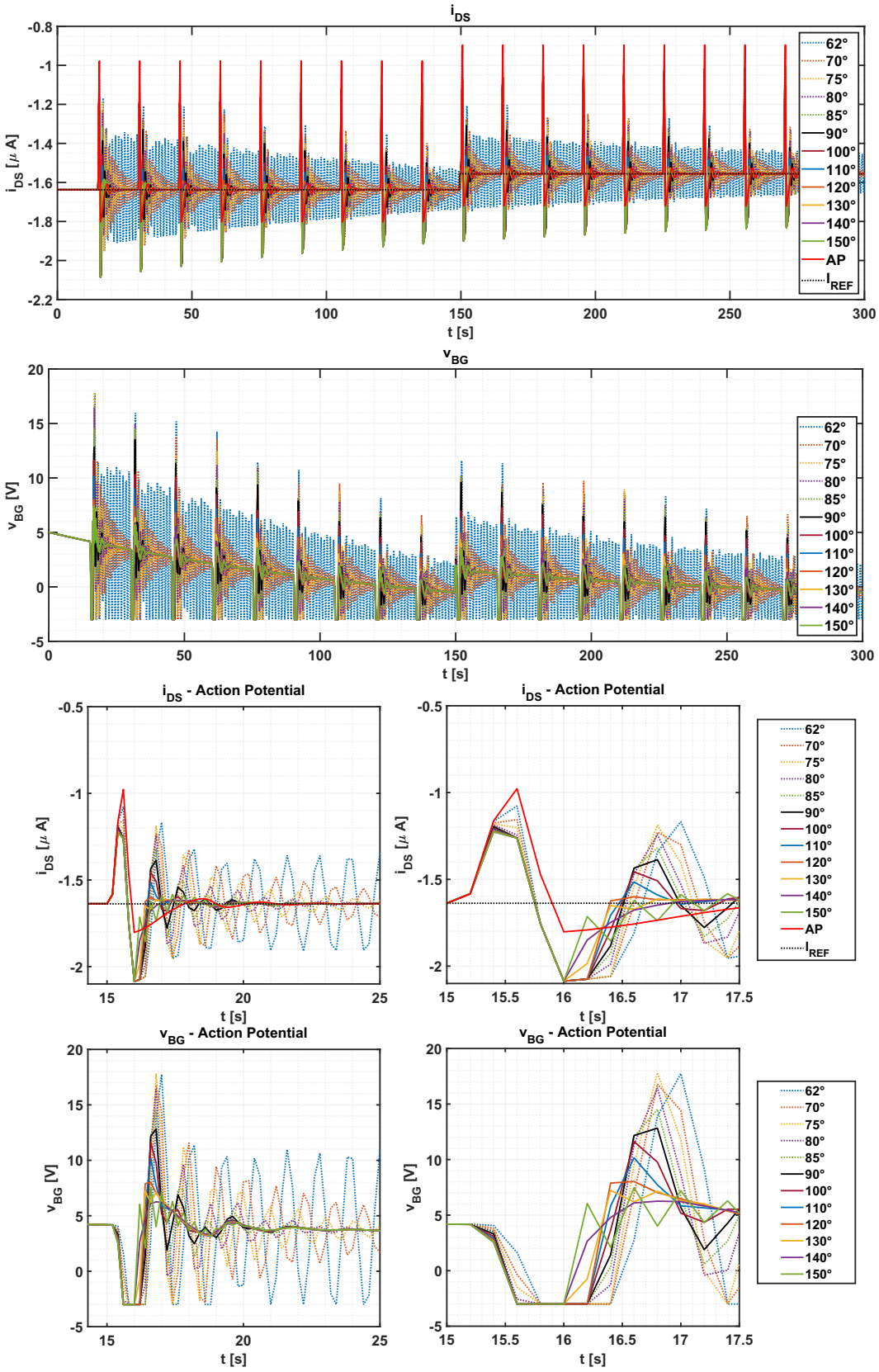

Figure 4.19: *Simulation 12 varying Φ_M: AP sensing $\omega_c = 6.28 rad/s$.*

Simulation 13

$\omega_c = 6.28 rad/s$ - saturation limit on - Action Potential - Feedforward off

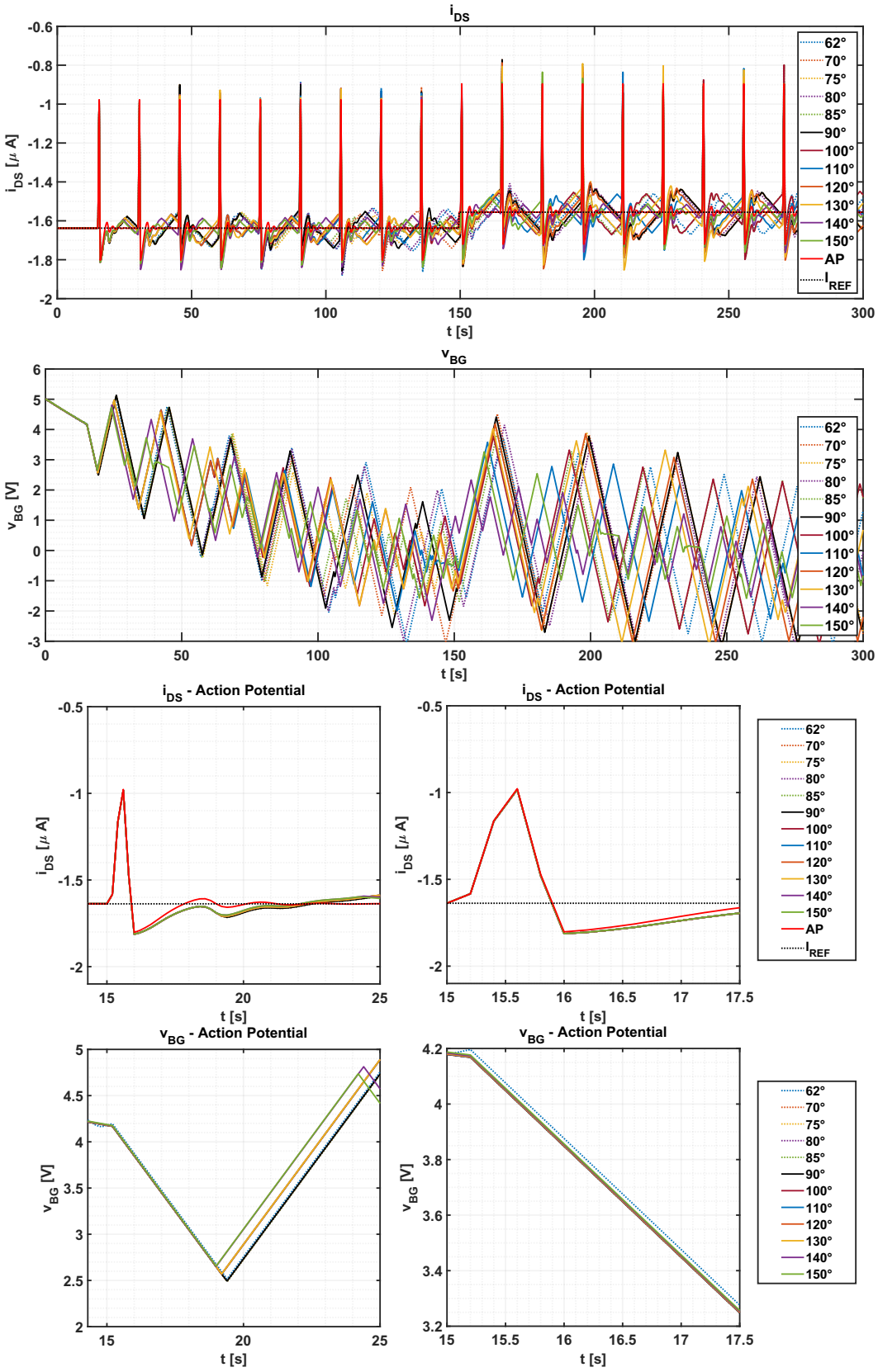

Figure 4.20: *Simulation 13 varying Φ_M: AP sensing $\omega_c = 6.28 rad/s$ + saturation.*

Simulation 14

$\omega_c = 6.28 rad/s$ - saturation limit on - Action Potential - Feedforward on

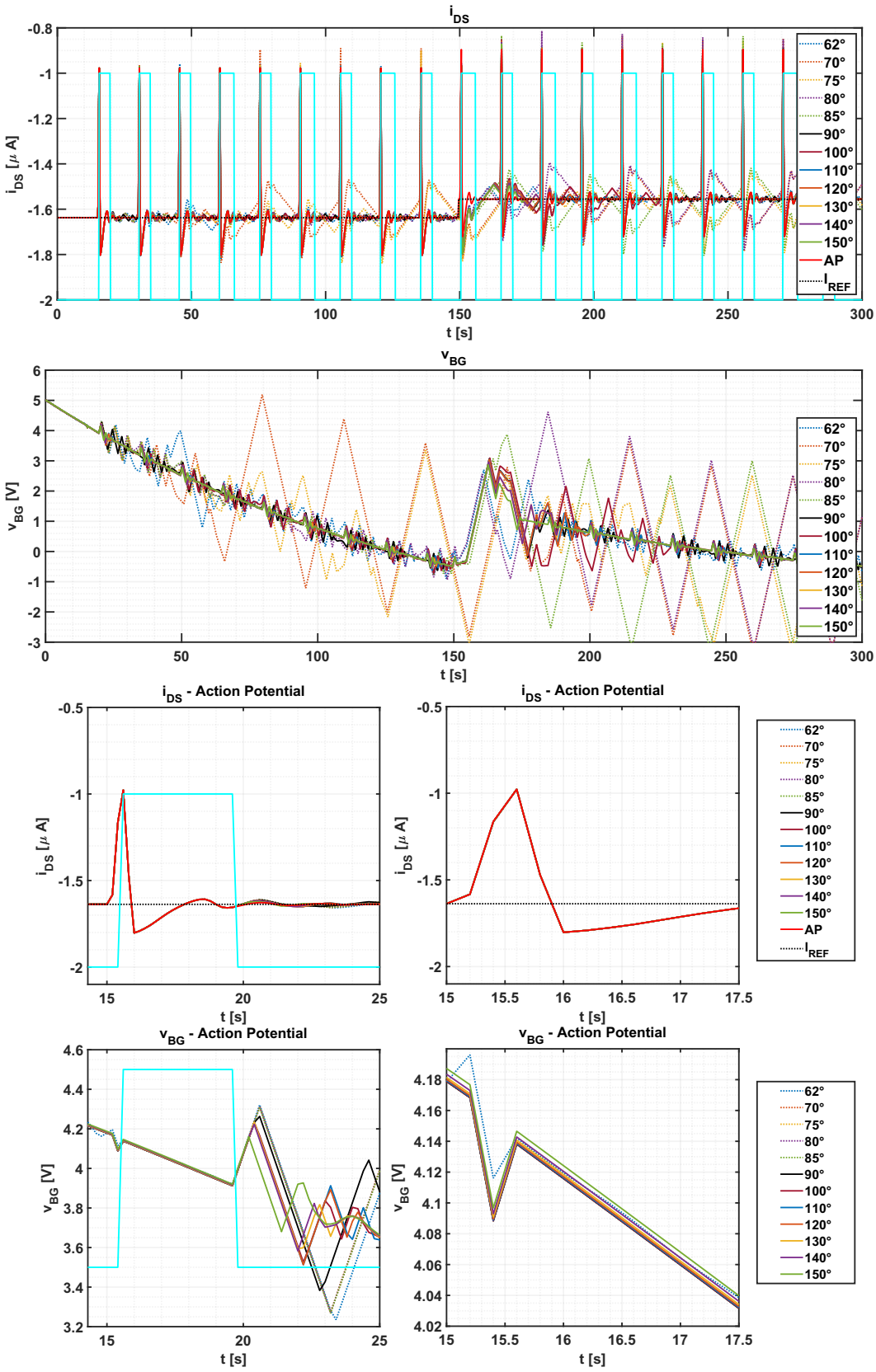

Figure 4.21: *Simulation 14 varying Φ_M: AP sensing $\omega_c = 6.28 rad/s$ + saturation + Feedforward.*

4.2 Experimental results

The measurement set-up is described in subsection 4.1.2 and the voltage applied to the EGOFET are reported on table 4.1. The sampling time is not fixed to $T_s = 200ms$ since the complexity of the algorithm and the control by Desktop Computer introduce some variable delays, however the average value is around $230ms$ and the difference is negligible for this discussion. In the following subsections the main final results of this experimental work, carried out on interdigitated lateral gate devices, are summarized.

4.2.1 Previous approach

The previous potentiometric approach, defined in subsection 3.1.1, has been tested in two variants, changing ΔV. Then, the cell recording function is shown.

Test 1

The digital control is enabled from the start of the measurement. In the first graph the control variables are set to $\Delta I = 1nA$ and $\Delta V = -100mV$, whereas in the second one ΔV is changed to $-10mV$.

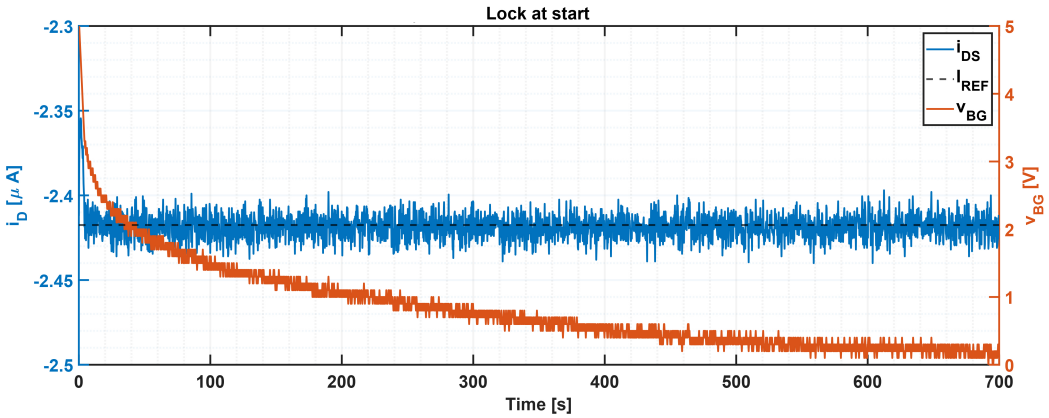

Figure 4.22: *Test 1:* $\Delta I = 1nA$ *and* $\Delta V = -100mV$.

The lower ΔV, the smaller the variance of the output current w.r.t. I_{REF}. However the reference tracking is considerably slower.

Table 4.3: Variance of the previous approach steady-state response at different ΔV.

$\Delta V\ [mV]$	$\sigma^2\ [A^2]$
-100	$9.9588 \cdot 10^{-17}$

$\Delta V\ [mV]$	$\sigma^2\ [A^2]$
-10	$2.9866 \cdot 10^{-17}$

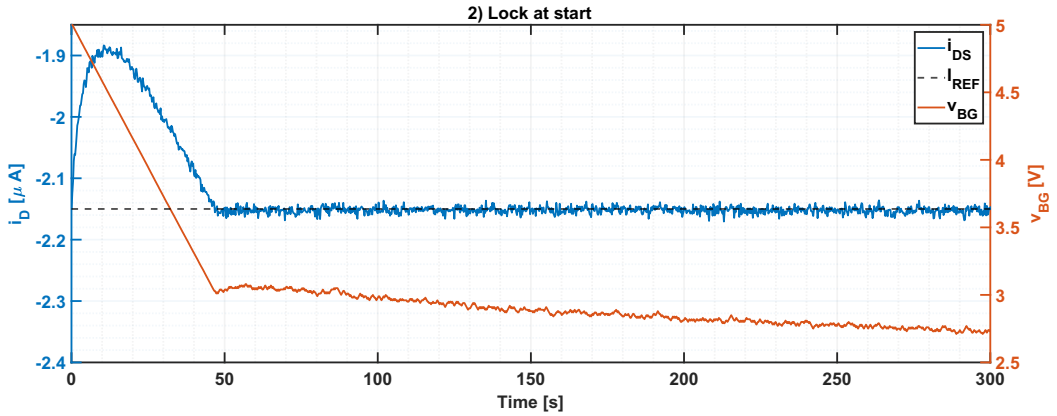

Figure 4.23: *Test 2: lock at start* $\Delta I = 1nA$ *and* $\Delta V = -10mV$.

Test 2

The digital control is activated after 10s of measurement, with $\Delta I = 1nA$ and $\Delta V = -10mV$ (Fig.4.24).

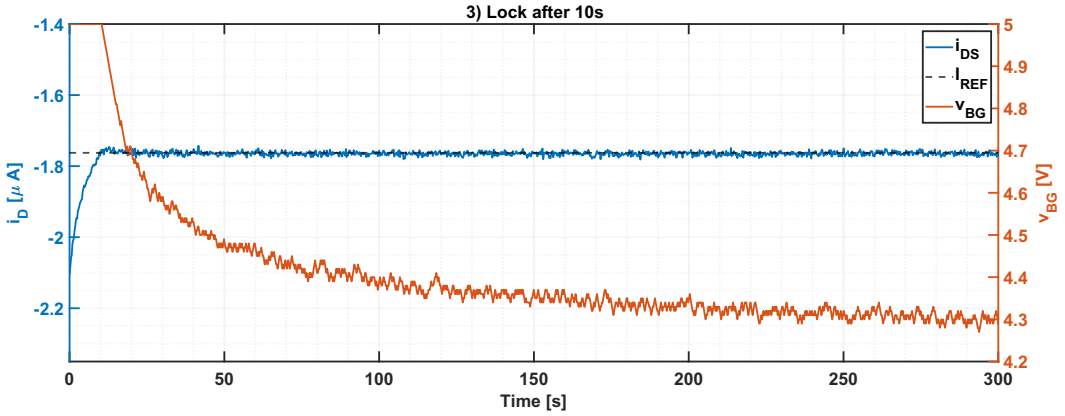

Figure 4.24: *Test 2 : lock after 10s* $\Delta I = 1nA$ *and* $\Delta V = -10mV$.

The initial settlement time allows to avoid the undershoot noticeable in Fig.4.23 and the overall control variable excursion is smaller.

Test 3

The action potential (Fig.3.4) has been applied after 70s as periodic voltage signal to the top-gate, by means of the arbitrary waveform generator, with a period of 10s. After 17s the digital control has been enabled, with the same parameters of Test 2. In order to compare the recorded action potentials with the expected ones, the simulated action potentials are shown in red (AP_{REF}), normalized w.r.t. their peak. The output current is normalized w.r.t. its highest peak, so that the probability of missed samples is minimized.

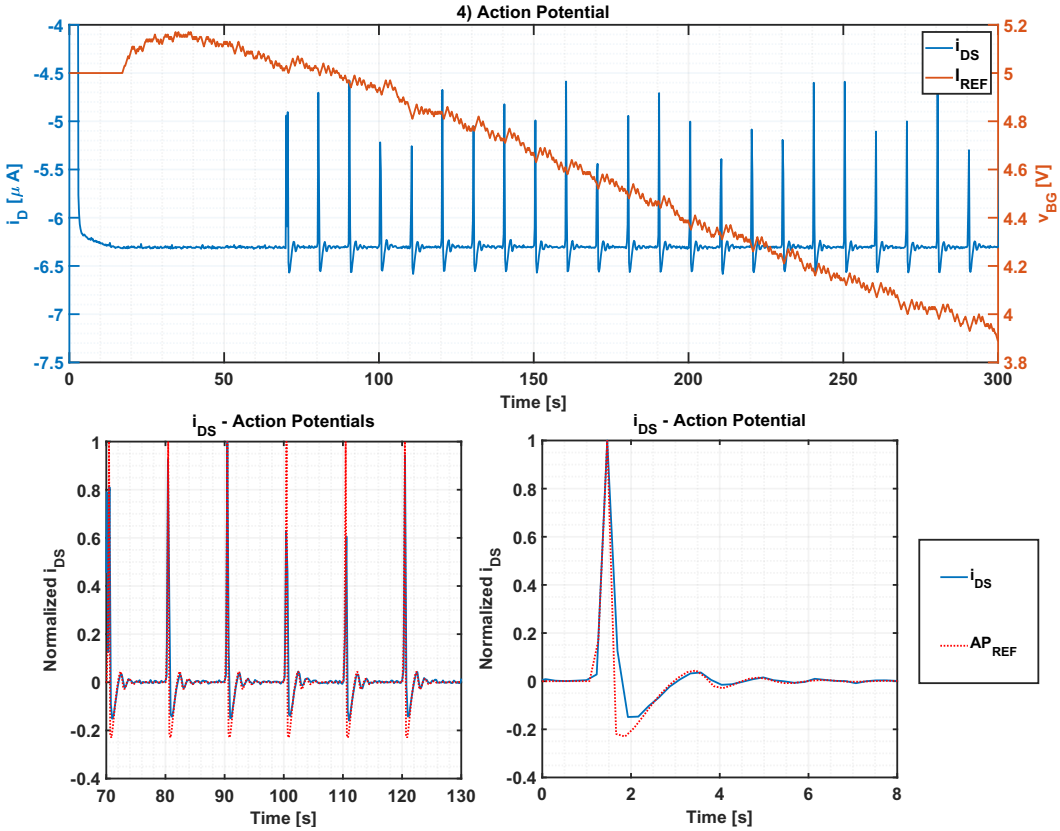

Figure 4.25: *Test 3 : action potential recording* $\Delta I = 1nA$ *and* $\Delta V = -10mV$.

The response of the system is so slow that the digital control cannot counteract the action potential. The result is a slightly distorted signal. However, from this approach, the output disturbance is not clearly estimable from the back-gate potential and if it abruptly changes its behavior, the controller will not be able to properly adapt the response. Furthermore, any variation on the sensed signal frequencies can be overcome only by trial and error calibration.

4.2.2 PI measurements repeatability

The PI digital control developed in previous chapter has been tested with some configurations in order to verify the repeatability of the measurements (Fig.4.26). I_{REF} was set to the initial value of i_{DS} and $\omega_c = 0.628 rad/s$.

Table 4.4: List of parameters used on repeatability test.

Test	Φ_M [°]	$g_{m_{BG}}$ [nS]
1	75	39.9
2	90	39.9

Test	Φ_M [°]	$g_{m_{BG}}$ [nS]
3	90	24.9
4	62	24.9

In sequence, *Test 1* and *Test 2* were performed by using the parameters reported in table 4.4, where the transconductance is the same adopted for the simulations. Then, the experiments have been repeated and after that the back-gate

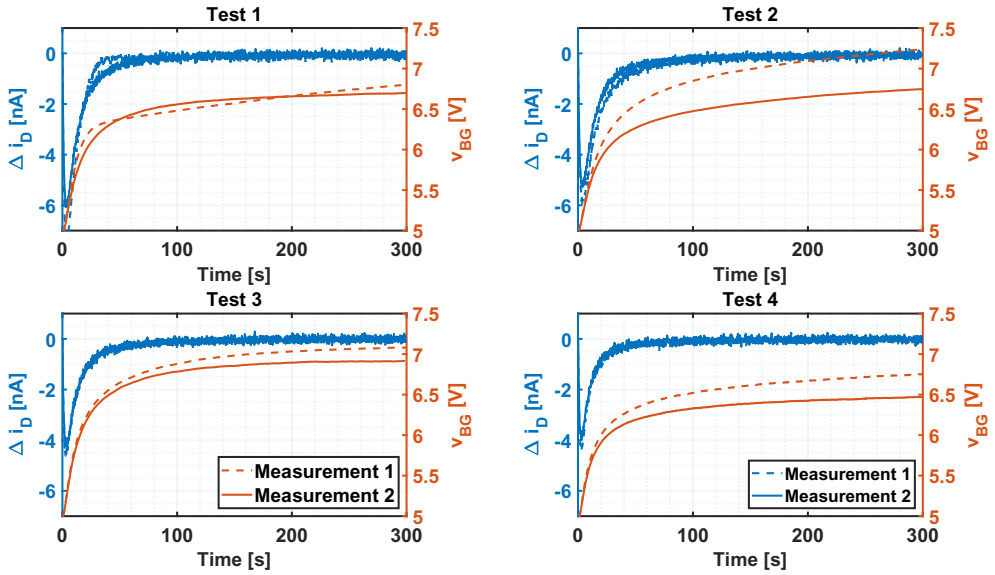

Figure 4.26: *Repeatability experiments.*

transconductance has been estimated by means of the slope of i_{DS}, obtained through v_{BG} scan from $5V$ to $5.5V$. Therefore, *Test 3* and *Test 4* were executed two times, by using the new estimated $g_{m_{BG}}$ to compute the PI gains. Finally, a new transconductance estimation has been carried out with the same method (Fig.4.27).

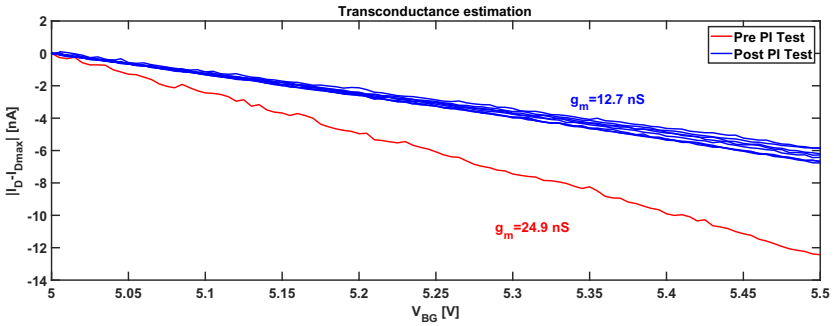

Figure 4.27: *Back-gate transconductance estimations.*

It is observable that the behaviour of the output current (from which I_{REF} is subtracted in Fig.4.26) does not change during consecutive measurements. The estimation of $g_{m_{BG}}$ seems to improve the response for both the initial undershoot and the back-gate variation. However, these also depend on the status of the device. Indeed, consecutive measurements induce charge trapping on the EGOFET, which sees its current drop due to threshold and mobility variations. In Fig.4.27 it is shown in blue the consecutive v_{BG} scan executed after the experiments. It can be seen that the slope does not change throughout an estimation, but it varies over time, denoting a substantial decay of the estimated back-gate transconductance. This phenomenon suggests the need of an autotuning system that can operate during the measurements.

4.2.3 Derivative mode effect

The fact that the derivative mode is unnecessary on the control of this system can be seen by these experiments, where starting from an integrator with $\Phi_M = 90°$ and $\omega_c = 0.628 rad/s$, we variate $|K_D|$ in range from $2 \cdot 10^6$ to $15 \cdot 10^6$. The only effect is to increase the sensibility to noise, making greater oscillations with higher gains.

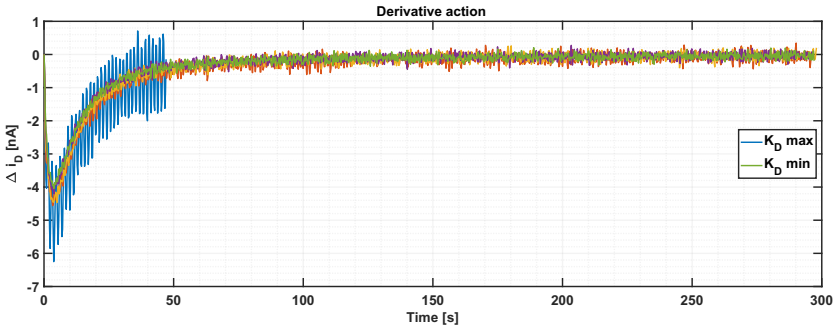

Figure 4.28: *Derivative mode effect.*

4.2.4 Autotuning methods

The autotuning methods described in subsection 3.2.6 are shown in the next experiments:

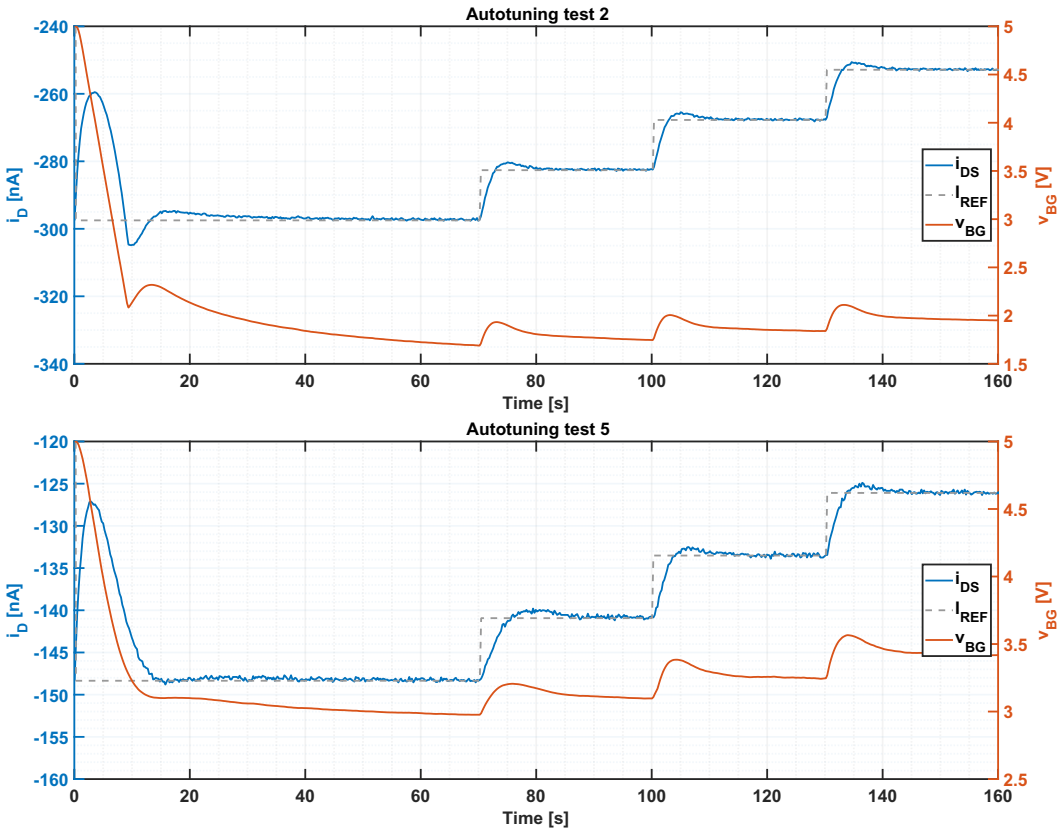

Figure 4.29: *Reference step autotuning.*

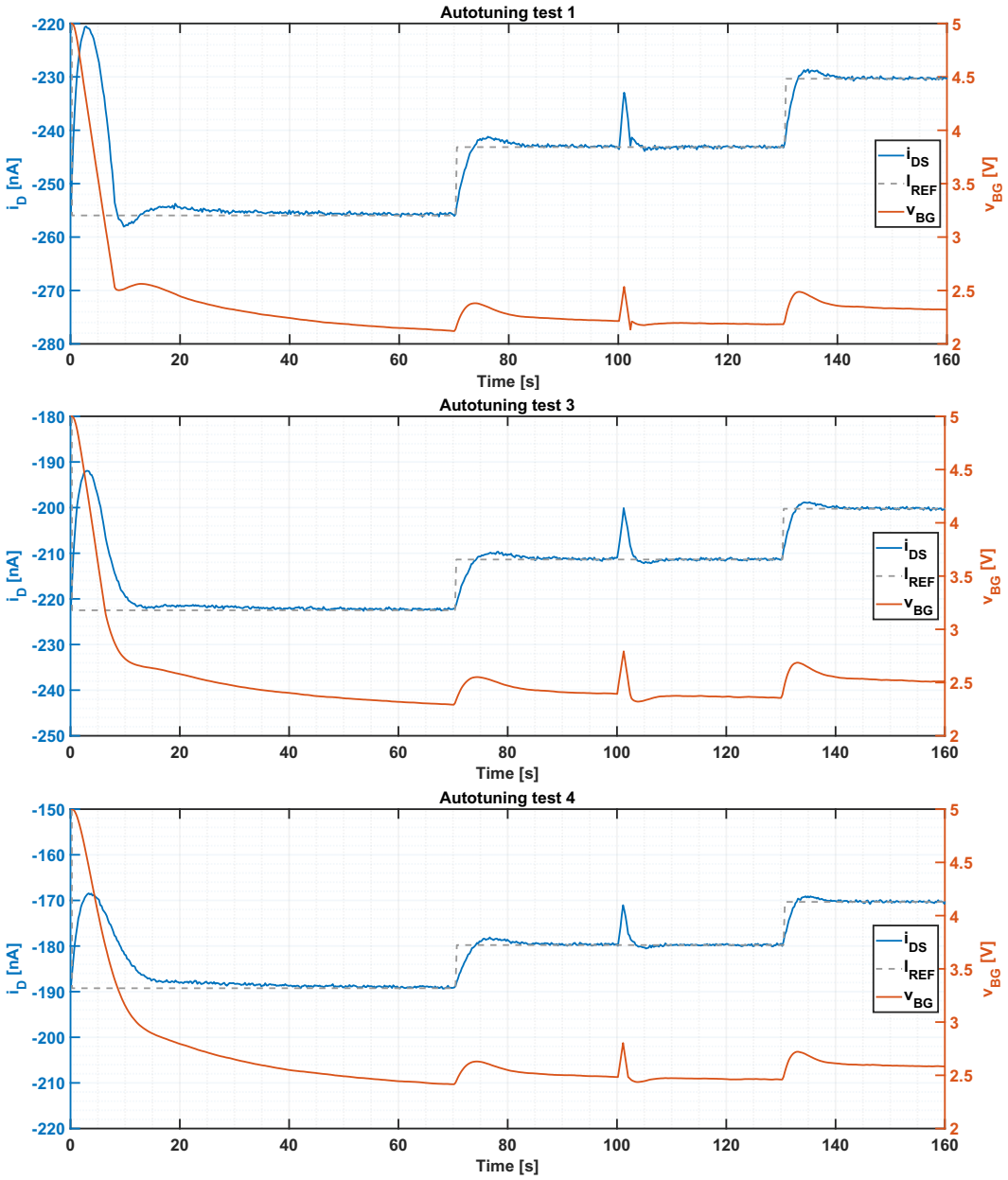

Figure 4.30: *Back-gate voltage ramp autotuning.*

All the measurements are carried out with $\Phi_M = 90°$ (that implies $K_P = 0$), $\omega_c = 0.628 rad/s$ and $K_{I_1} = 1.482 \cdot 10^7$, computed by using $g_{m_{BG_1}} = 58.4 nS$ (estimated by v_{BG} scan). In order to compare the step response before and after autotuning, the experiment proceeds as follow: to ensure reaching steady-state, the system operates for 70s. At this point the reference current is decreased by 5%I_{REF} and the set-up keeps measuring until 100s. At this time the autotuning activates and after 30s the last reference step is performed.

In Fig.4.29 is shown the *reference step* autotuning method, while the *back-gate voltage ramp* is presented in Fig.4.30. The estimated back-gate transconductances and the corresponding K_I are listed on table 4.5.

Table 4.5: Autotuning estimated parameters.

Test	$g_{m_{BG_2}}$ [nS]	K_{I_2}
1	28.5	$2.207 \cdot 10^7$
2	40.1	$1.572 \cdot 10^7$
3	23.7	$2.660 \cdot 10^7$
4	23.8	$2.653 \cdot 10^7$
5	21.1	$2.982 \cdot 10^7$

Both autotuning methods are reliable for which concerns the $g_{m_{BG}}$ estimation and the real-time operability. As demonstration of the autotuning effectiveness, in Fig.4.31 it is observable the comparison between the reference steps and how the system responses post-tuning are similar to each other. The back-gate voltage ramp seems to be less invasive and faster w.r.t. the reference step, therefore it will be used for the next experiments.

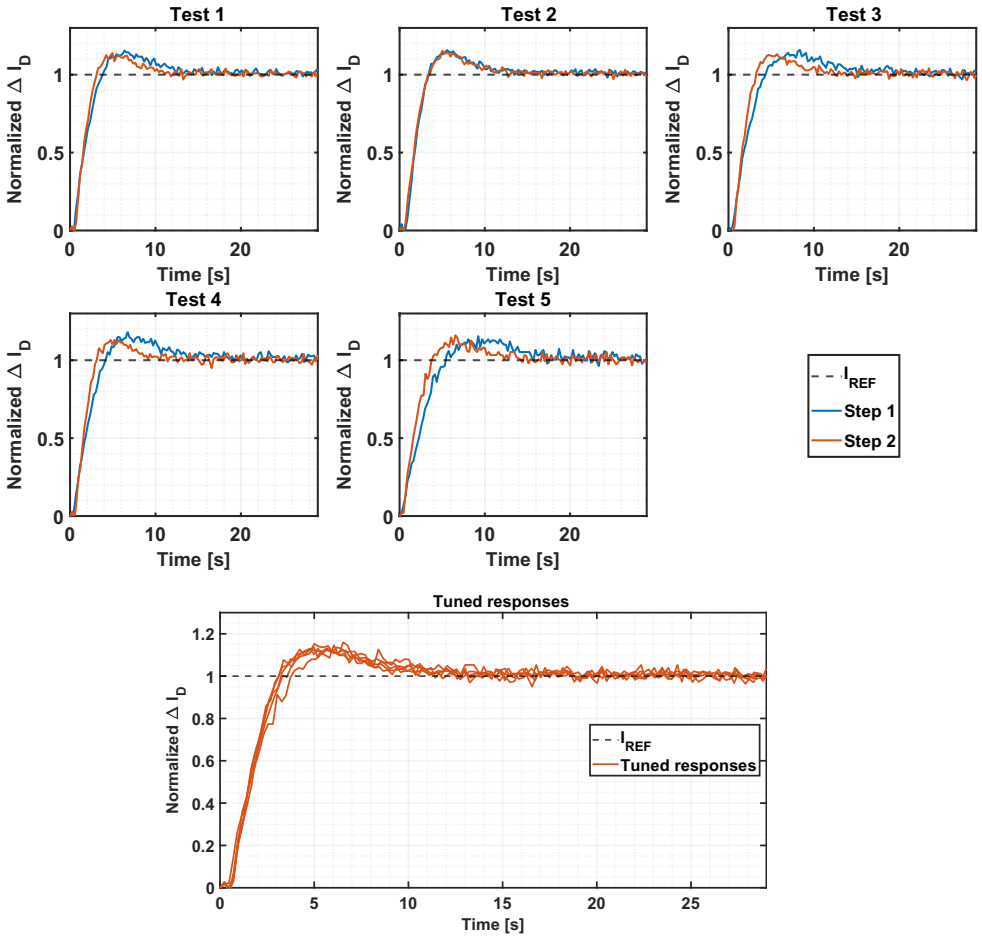

Figure 4.31: *Autotuning reference tracking.*

4.2.5 PI varying phase margin and crossing frequency

In the following tests, some relevant Φ_M and ω_c have been tried to observe the responses of the system and to compare them with the simulations. The experiments follow the autotuning tests procedure, starting from PI parameters used on theoretical analysis, with $\omega_c = 0.628$. The estimated back-gate transconductances and PI gains implemented are reported in tables 4.6,4.7 and 4.8.

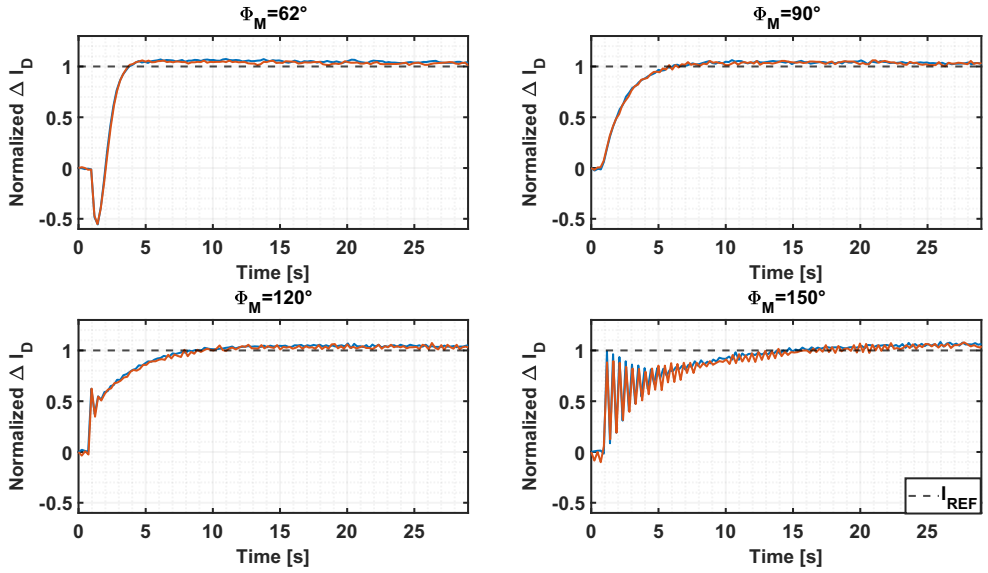

Figure 4.32: *Tuned responses varying Φ_M.*

In Fig.4.32 are shown the step responses varying Φ_M, without the saturation limit on the derivative of the back-gate potential. Depending on the chosen phase margin, the responses are identical over time. In Fig.4.33 is presented a comparison between the simulated responses and the measured ones. Despite some noise and deviation from the steady-state expected value, the results are almost identical also in this case.

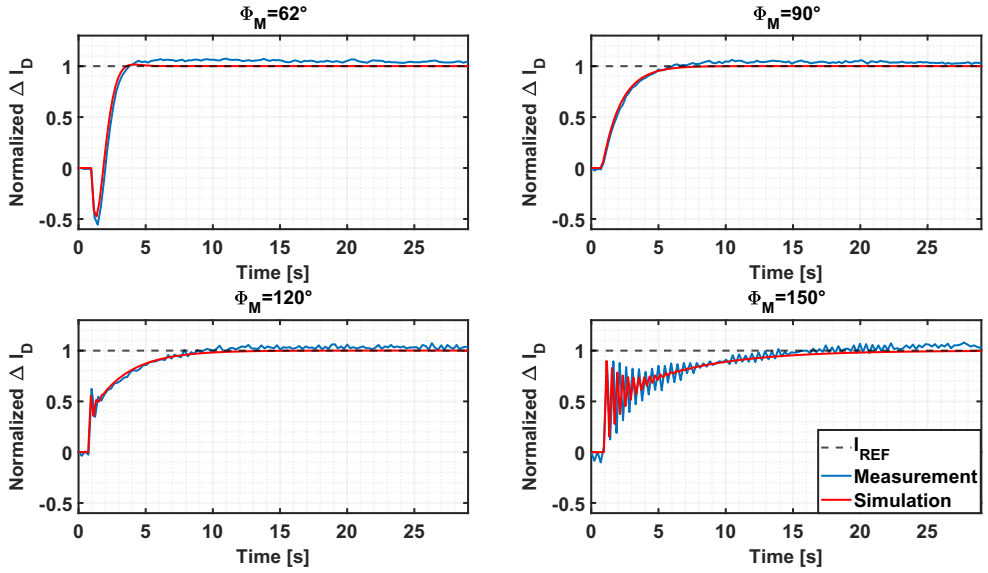

Figure 4.33: *Tuned responses varying Φ_M: measurements-simulations.*

The same experiments have been carried out enabling the saturation limit $\Delta V_{BG_{max}}$. The step responses are still coherent each other (Fig.4.34), however the settling time is faster w.r.t. the simulations, as shown in Fig.4.35. These differences can be attributed to neglected capacitive coupling effects and device degradation. In fact, during measurements, the output current is substantially decreased (Fig.4.37,4.38,4.39) and the estimated back-gate transconductance seems to confirm a decay on the EGOFET responsiveness, as it can be seen in Fig.4.36. Nevertheless, the slight recovery observable every four tests (where the pause before the successive experiment was longer) suggests that the lowering of $g_{m_{BG}}$ may be related also to charge trapping-detrapping phenomena.

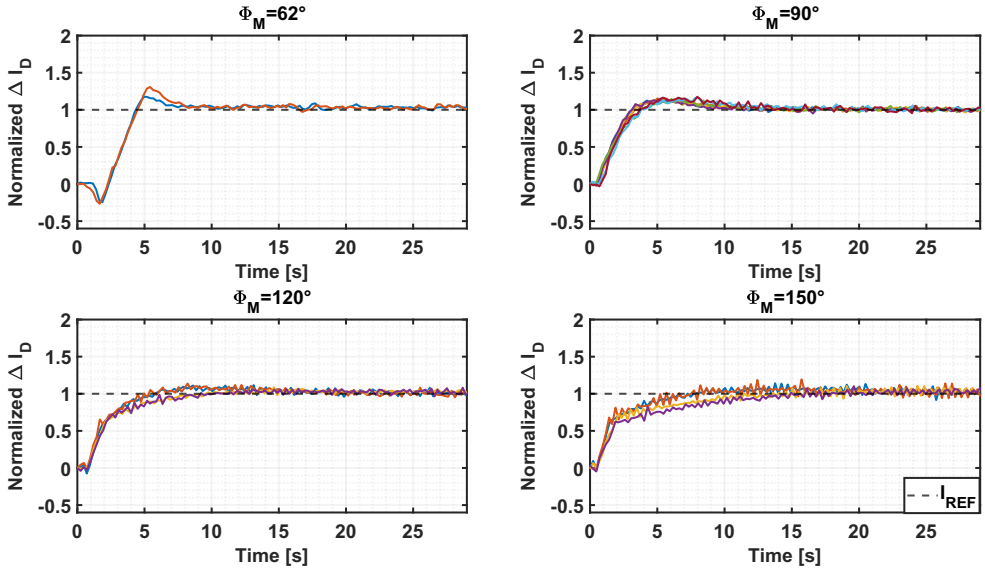

Figure 4.34: *Tuned responses varying Φ_M (saturation limit enabled).*

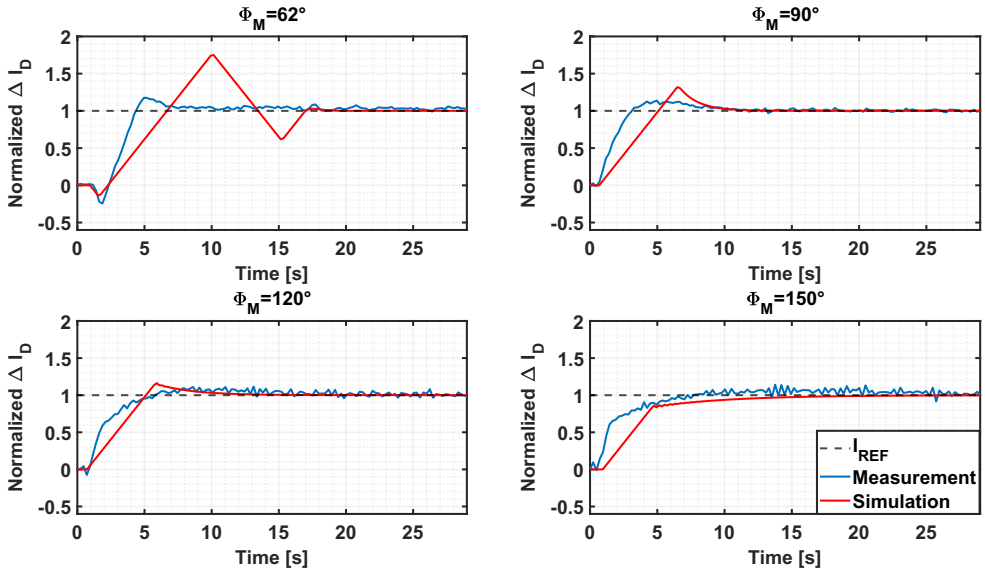

Figure 4.35: *Tuned responses varying Φ_M: measurements-simulations (saturation limit enabled).*

Table 4.6: Autotuning estimated parameters (saturation limit enabled): experiment 1.

Test	Φ_M [°]	$g_{m_{BG_2}}$ [nS]	K_{P_2}	K_{I_2}
1	90	9.8	0	$9.237 \cdot 10^7$
2	120	5.3	$9.510 \cdot 10^7$	$10.377 \cdot 10^7$
3	150	5.2	$1.675 \cdot 10^8$	$6.091 \cdot 10^7$
4	90	6.5	0	$9.751 \cdot 10^7$
5	120	5.1	$9.769 \cdot 10^7$	$1.066 \cdot 10^8$
6	150	4.3	$1.997 \cdot 10^8$	$7.265 \cdot 10^7$

Table 4.7: Autotuning estimated parameters: experiment 2.

Test	Φ_M [°]	$g_{m_{BG_2}}$ [nS]	K_{P_2}	K_{I_2}
1	62	71.1	$-6.596 \cdot 10^6$	$7.815 \cdot 10^6$
2	90	55.3	0	$1.140 \cdot 10^7$
3	120	47.3	$1.057 \cdot 10^7$	$1.154 \cdot 10^7$
4	150	34.3	$2.525 \cdot 10^7$	$9.185 \cdot 10^6$
5	62	46.3	$-1.013 \cdot 10^7$	$1.201 \cdot 10^7$
6	90	29.1	0	$2.168 \cdot 10^7$
7	120	21.3	$2.344 \cdot 10^7$	$2.558 \cdot 10^7$
8	150	18.8	$4.619 \cdot 10^7$	$1.680 \cdot 10^7$

Table 4.8: Autotuning estimated parameters (saturation limit enabled): experiment 3.

Test	Φ_M [°]	$g_{m_{BG_2}}$ [nS]	K_{P_2}	K_{I_2}
9	62	19.8	$-2.372 \cdot 10^7$	$2.811 \cdot 10^7$
10	90	16.6	0	$3.804 \cdot 10^7$
11	120	14.5	$3.445 \cdot 10^7$	$3.759 \cdot 10^7$
12	150	11.1	$7.806 \cdot 10^7$	$2.839 \cdot 10^7$
13	62	12.3	$-3.803 \cdot 10^7$	$4.506 \cdot 10^7$
14	90	11.3	0	$5.561 \cdot 10^7$
15	120	10.2	$4.885 \cdot 10^7$	$5.331 \cdot 10^7$
16	150	10.2	$8.527 \cdot 10^7$	$3.101 \cdot 10^7$

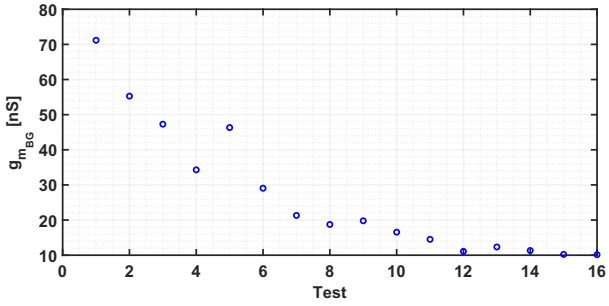

Figure 4.36: *Estimated back-gate transconductance over time during experiment 2.*

Table 4.9: Range estimated transconductances.

Φ_M [°]	62	90	120	150
$g_{m_{BG}}$ [nS]	[12.3 – 71.1]	[6.5 – 55.3]	[5.1 – 71]	[4.3 – 34.3]

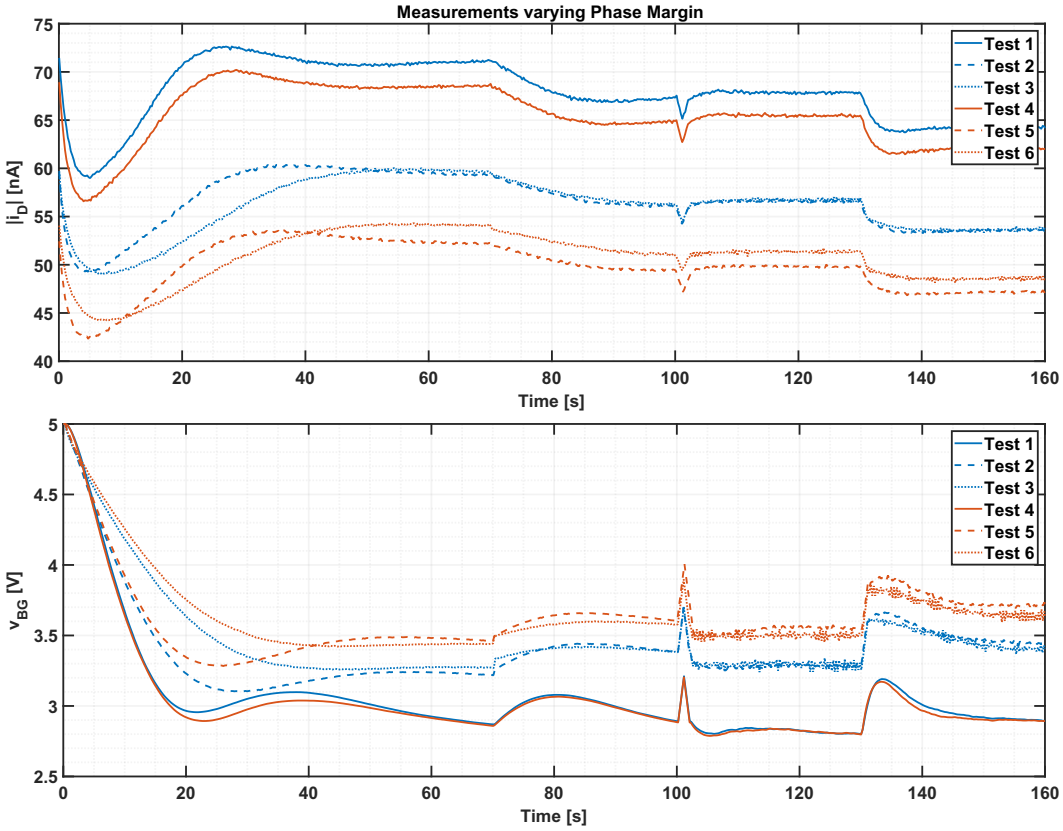

Figure 4.37: *Measurements varying Φ_M: experiment 1.*

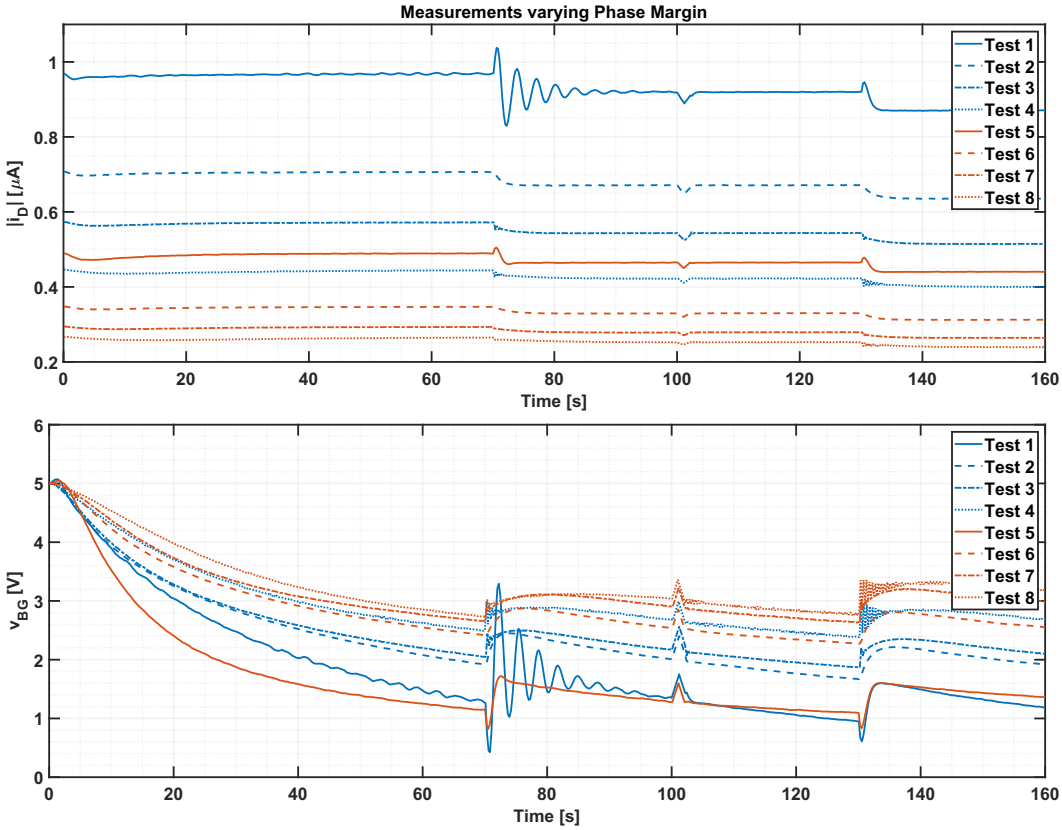

Figure 4.38: *Measurements varying Φ_M: experiment 2.*

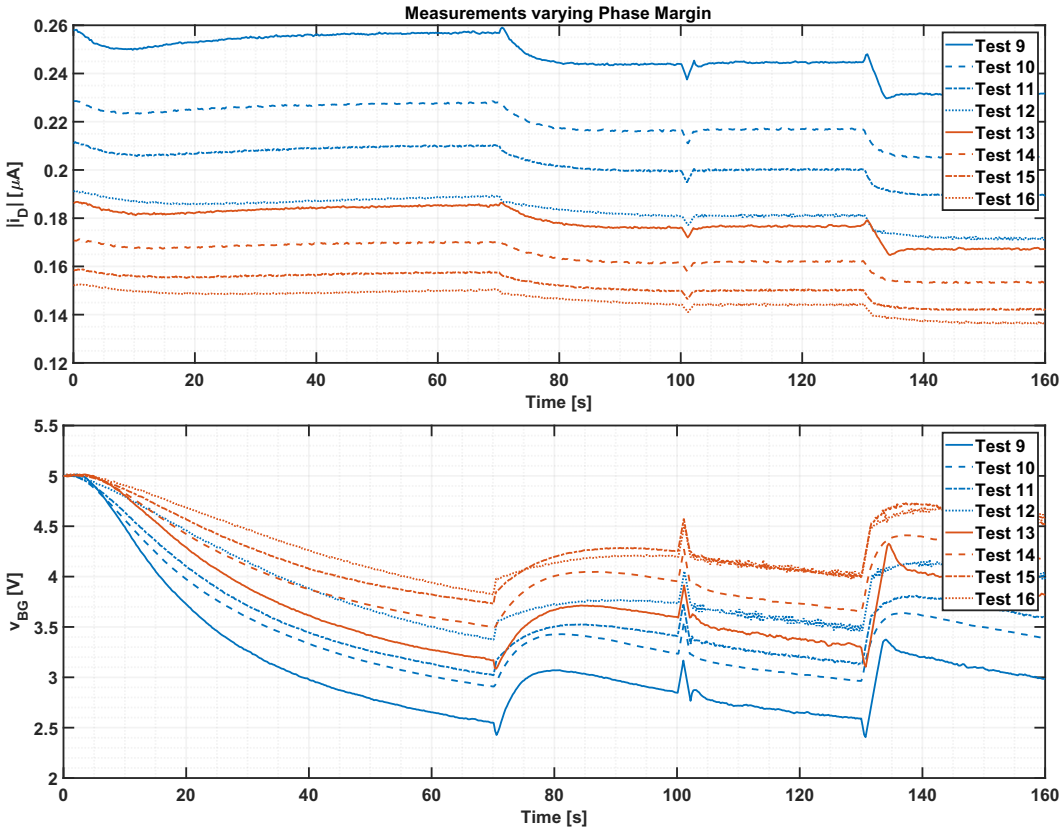

Figure 4.39: *Measurements varying Φ_M (saturation limit enabled): experiment 3.*

The next tests regards the system response varying the crossing frequency. The digital control has been set up with $\Phi_M = 120°$ and the initial PI gains are the same used on the simulations. The three configurations of ω_c described on subsection 3.2.3 have been tested and the results are shown in the next figures (estimated parameters on table 4.10).

Table 4.10: Autotuning estimated parameters: experiment 4.

Test	ω_c $[rad/s]$	$g_{m_{BG_2}}$ [nS]	K_{P_2}	K_{I_2}
1	0.0628	44.1	$1.134 \cdot 10^7$	$1.238 \cdot 10^6$
2	0.628	39	$1.283 \cdot 10^7$	$1.400 \cdot 10^7$
3	6.28	41.4	$1.209 \cdot 10^7$	$1.319 \cdot 10^8$
4	0.0628	39.6	$1.262 \cdot 10^7$	$1.377 \cdot 10^6$
5	0.628	44.2	$1.132 \cdot 10^7$	$1.235 \cdot 10^7$
6	6.28	42.1	$1.187 \cdot 10^7$	$1.295 \cdot 10^8$

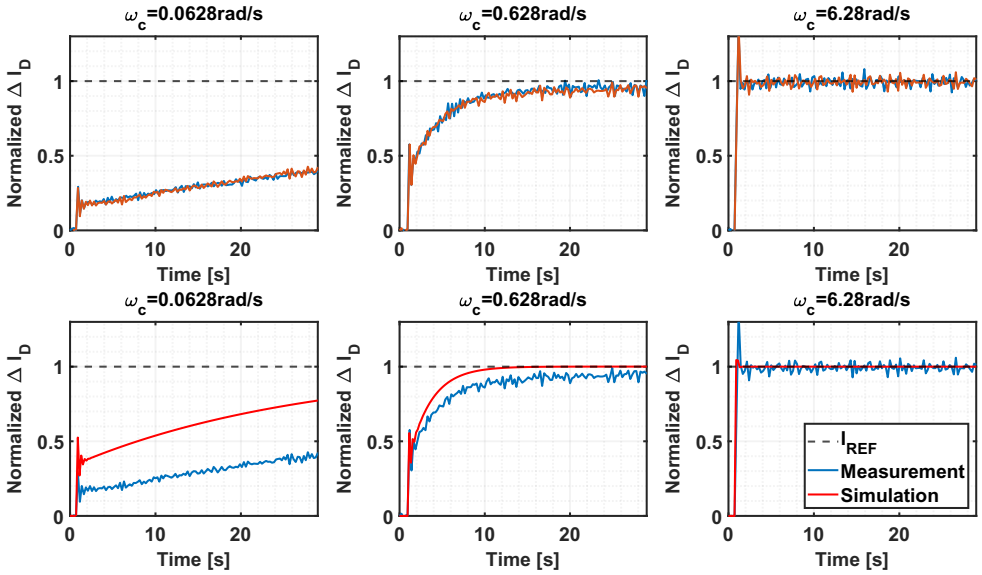

Figure 4.40: *Tuned responses varying ω_c and comparison with simulations.*

The configuration with $\omega_c = 6.28 rad/s$ seems to be stable and the setting time is around $800ms$. With $\omega_c = 0.628 rad/s$ it become more than 15 times greater, but there is no overshoot on the response. Smaller ω_c are unfeasible, since the steady-state regime cannot be reached within a reasonable time. On these experiments the saturation limit never had to be enabled, probably due to the high number of consecutive measurements that caused significant drop in current, but at the same time a sort of stabilization of its electrical characteristics. Confirming that, the range of estimated back-gate transconductances is within a small range $[39nS - 44.2nS]$.

From Fig.4.41, observing the control variable, it is observable that the detrimental behaviour has changed its shape w.r.t. the previous tests.

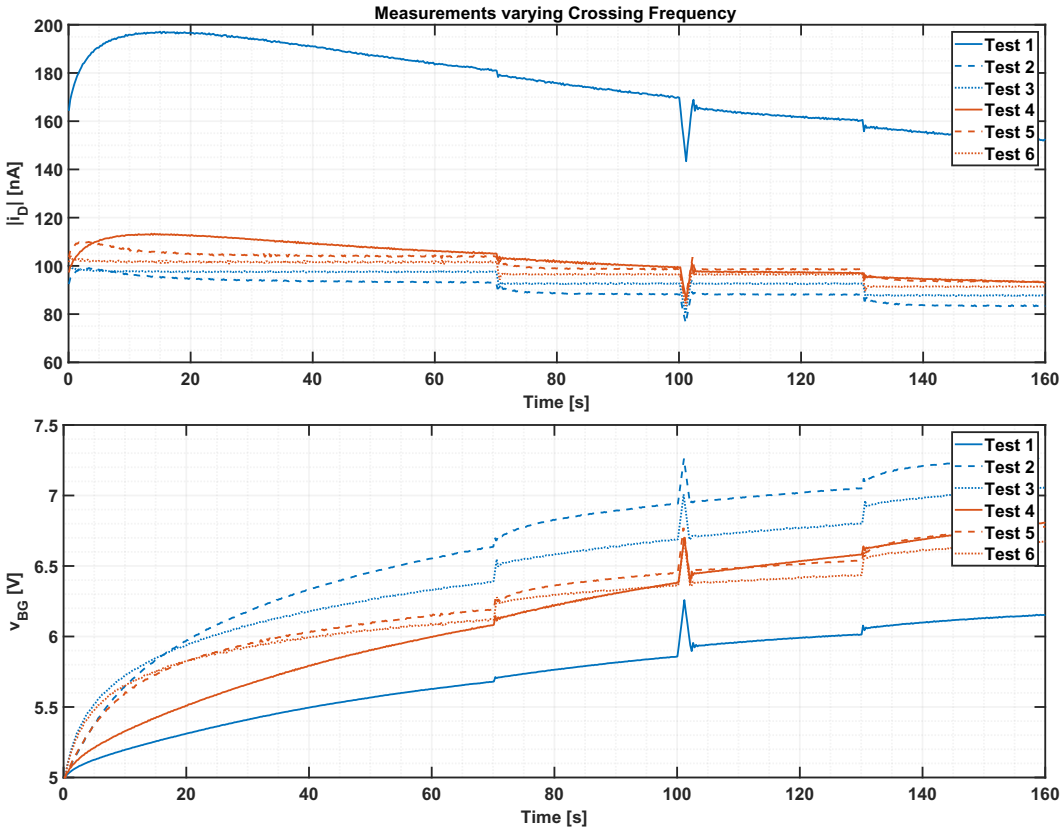

Figure 4.41: *Measurements varying ω_c: experiment 4.*

Table 4.11: Variance of the PI control steady-state response.

σ^2_{min} $[A^2]$	σ^2_{max} $[A^2]$	$\overline{\sigma}^2$ $[A^2]$
$1.3127 \cdot 10^{-20}$	$1.6530 \cdot 10^{-19}$	$4.9266 \cdot 10^{-20}$

In table 4.11 the values of i_{DS} variance at steady-state are reported. It is remarkable to note that all the configurations of the developed digital control achieve much lower variance values than those obtained with the previous approach($\sigma^2 \sim 10^{-17} A^2$ in table 4.3).

4.2.6 Action potential recording

The sensing of the hypotetical cell signal has been tested in four configurations: $\omega_c = 0.628 rad/s$ and $\omega_c = 6.28 rad/s$, with and without the action potential detection and feedforward control. The autotuning activates after 50 seconds. Then the action potential signal generated by the arbitrary waveform generator starts at $100s$. In table 4.12 the estimated parameters of these measurements are listed.

Table 4.12: Autotuning estimated parameters AP tests.

Test	ω_c $[rad/s]$	$g_{m_{BG_2}}$ [nS]	K_{P_2}	K_{I_2}
1	0.628	71	$7.045 \cdot 10^6$	$7.688 \cdot 10^6$
2	0.628	28.9	$1.731 \cdot 10^7$	$1.889 \cdot 10^7$
3	6.28	26.5	$1.890 \cdot 10^7$	$2.062 \cdot 10^8$
4	6.28	32.2	$1.553 \cdot 10^7$	$1.695 \cdot 10^8$
5	0.628	51.2	$9.771 \cdot 10^6$	$1.066 \cdot 10^7$
6	0.628	28.9	$1.731 \cdot 10^7$	$1.889 \cdot 10^7$
7	6.28	26.8	$1.866 \cdot 10^7$	$2.036 \cdot 10^8$
8	6.28	26.3	$1.900 \cdot 10^7$	$2.073 \cdot 10^8$

The detection and feedforward action leds to the better sensing of the action potential, with similar results with both the crossing frequencies involved (Fig.4.44,Fig.4.46,Fig.4.48,Fig.4.50). The cell signal is slightly distorted if only PI control is enabled, with $\omega_c = 0.628 rad/s$ (Fig.4.43,Fig.4.47). Higher ω_c cannot be implemented without the feedforward, otherwise uncontrolled oscillations make the system unstable (Fig.4.45,Fig.4.49).

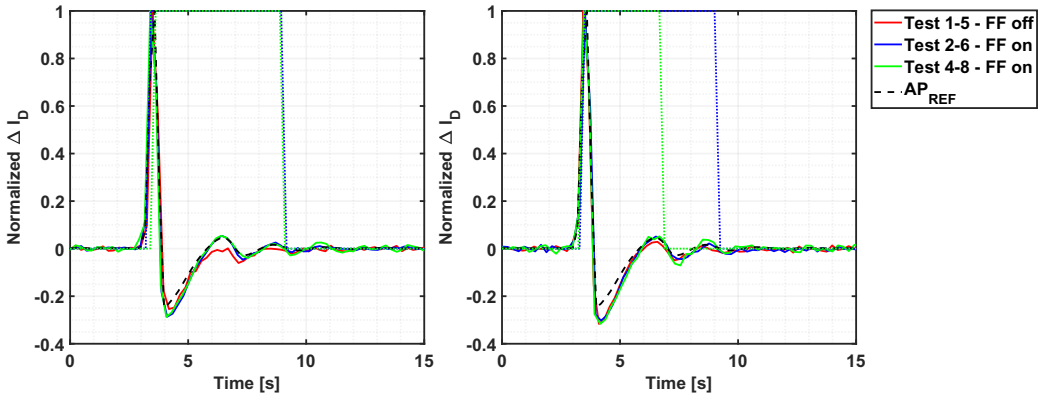

Figure 4.42: *Action potential sensing.*

In Fig.4.42 are shown the main results, taking for comparison the highest peak for each test. On the left the first triplet of measurements and on the right the same tests repeated sequentially. The first configuration with $\omega_c = 0.628 rad/s$ and the feedforward disabled is represented in red, while the dashed black line is the signal generated by the instrument, considering $T_s = 200ms$. Blue and green lines constitute the measured action potentials with the feedforward enabled, respectively at $\omega_c = 0.628 rad/s$ and $\omega_c = 6.28 rad/s$. The dotted lines show the period where the action potential is detected by the algorithm. We can observe that the end of the detection always exceeds the first two peaks, which are the most relevant features for the action potential recognition.

Anticipating the onset of detection by lowering the threshold could improve sensing by preventing the feedforward action from including part of the peak compensation in the v_{BG} fit.

Despite the current decay from the first measurement to the last one on the stressed device, the results on the sensed output are still good, obtaining a well-preserved action potential.

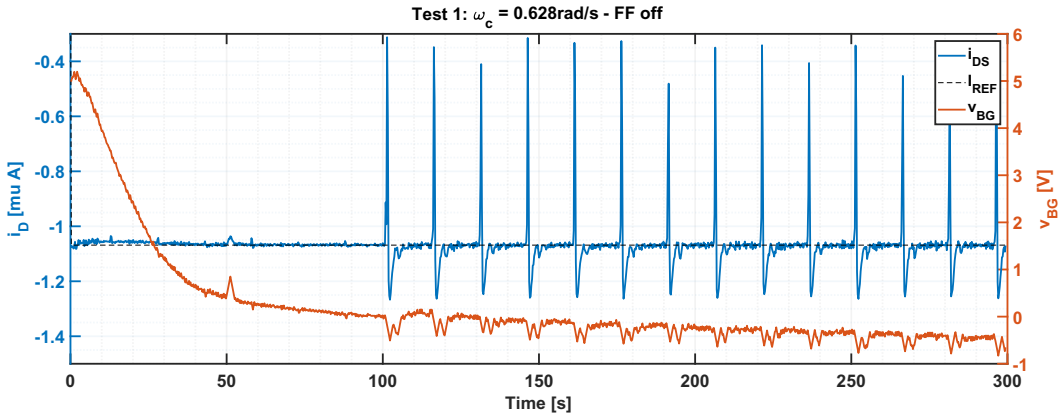

Figure 4.43: *Test AP 1: $\omega_c = 0.628 rad/s$ - Feedforward off.*

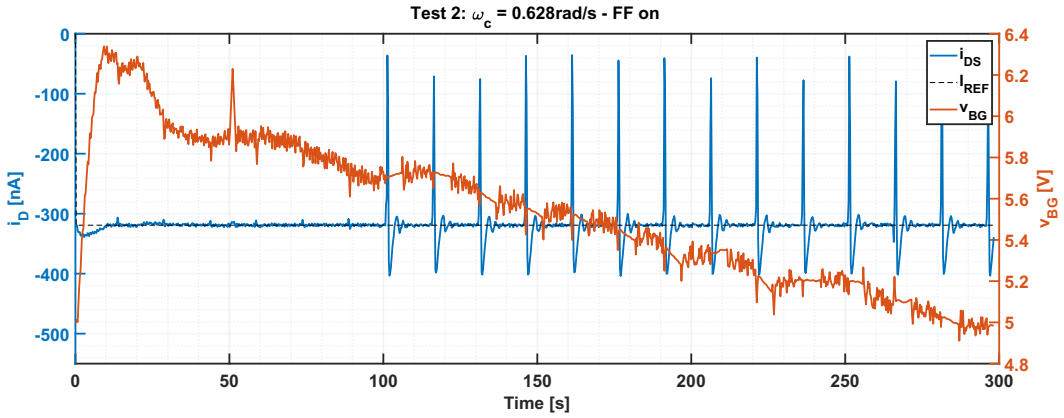

Figure 4.44: *Test AP 2: $\omega_c = 0.628 rad/s$ - Feedforward on.*

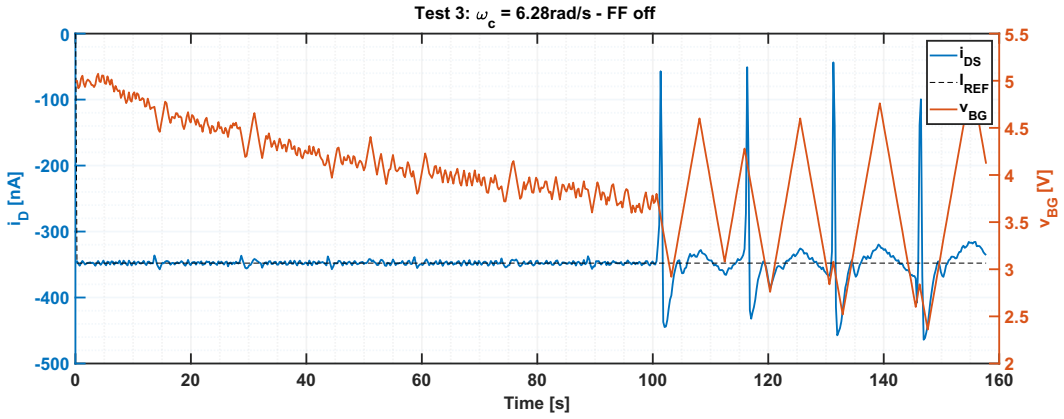

Figure 4.45: *Test AP 3: $\omega_c = 6.28 rad/s$ - Feedforward off.*

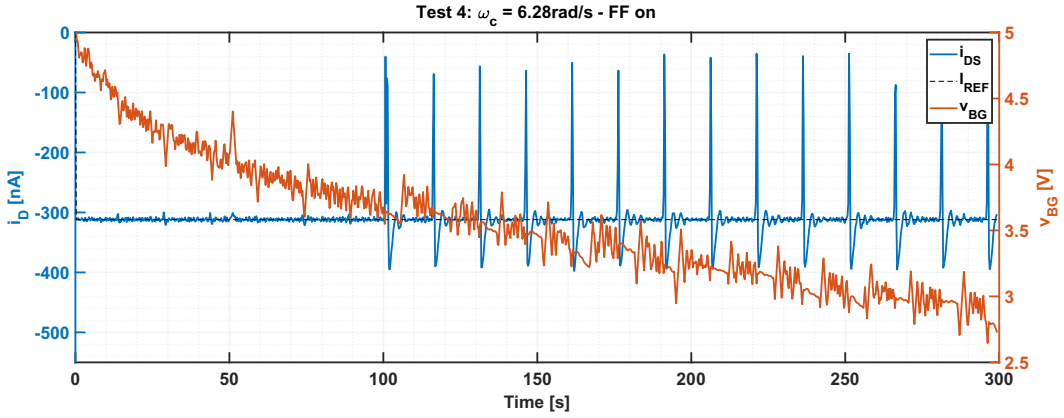

Figure 4.46: *Test AP 1: $\omega_c = 6.28 rad/s$ - Feedforward on.*

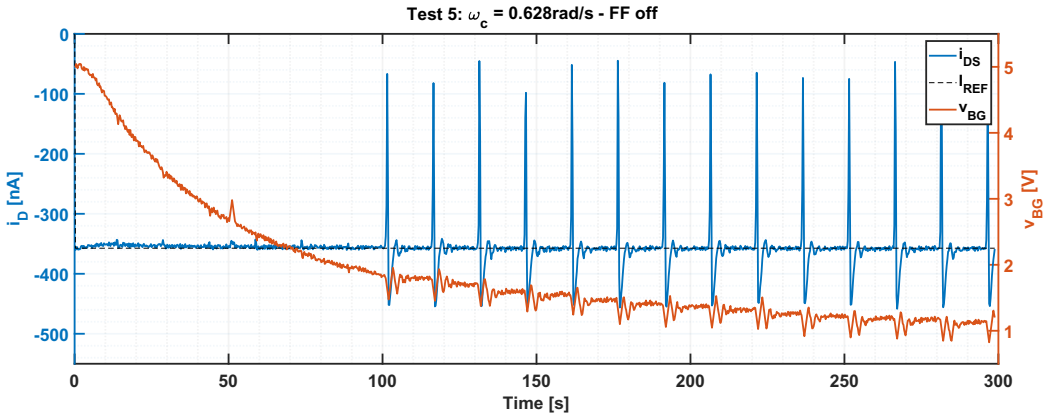

Figure 4.47: *Test AP 5: $\omega_c = 0.628 rad/s$ - Feedforward off.*

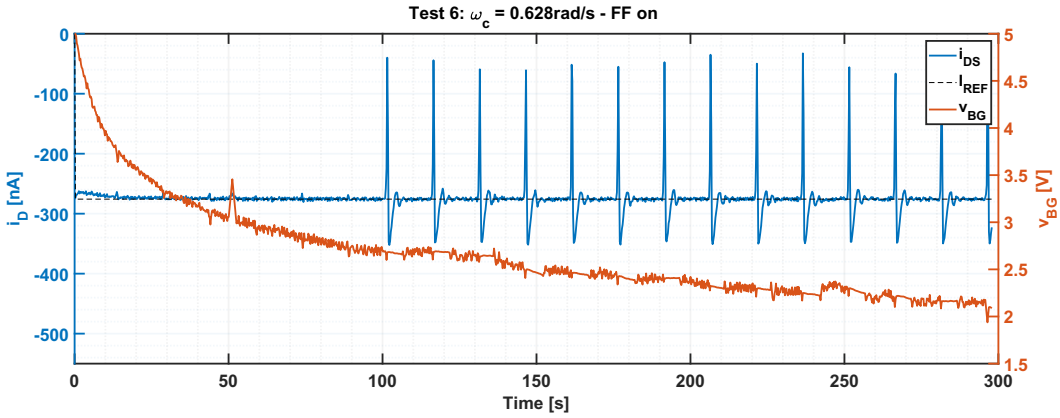

Figure 4.48: *Test AP 6: $\omega_c = 0.628 rad/s$ - Feedforward on.*

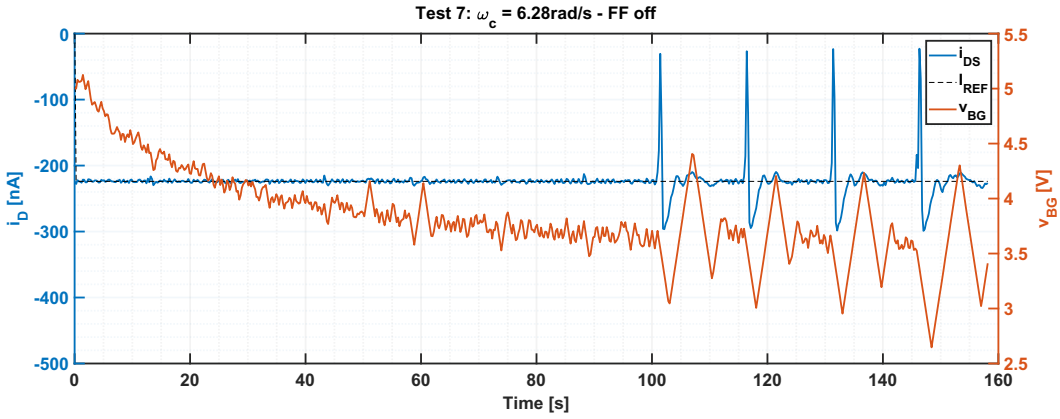

Figure 4.49: *Test AP 7: $\omega_c = 6.28 rad/s$ - Feedforward off.*

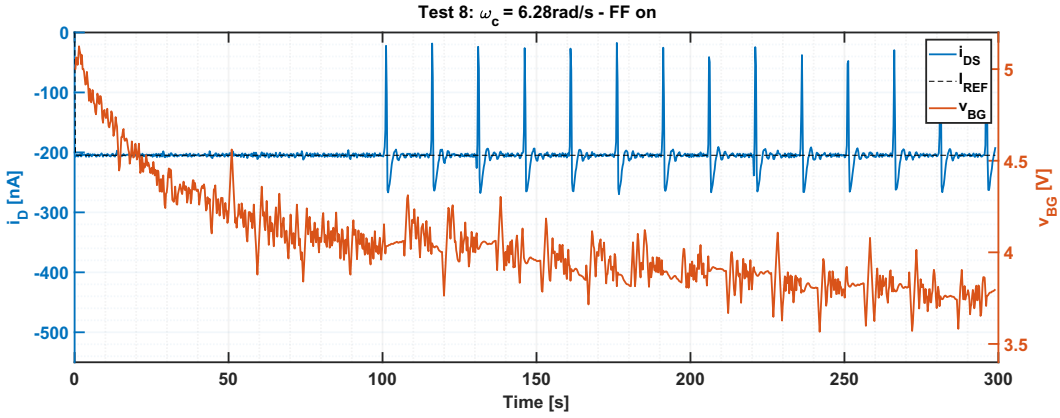

Figure 4.50: *Test AP 8: $\omega_c = 6.28 rad/s$ - Feedforward on.*

4.2.7 Long term measurements

One of the goal of this digital control is to achieve long term detections maintaining well-defined output signal and preserving the information about the sensed input, in this discussion represented by the cell action potential. In order to test this purpose, continuous measurements lasting more than 15 hours were performed. Results showed that the device can efficiently records the cell signal for more than 5 hours. Then, the control stop its action due to the v_{BG} saturation limits and the output signal gradually starts to be unable to track the reference signal. The action potentials become no more recognisable by their shape, but the instant of the activity can still be detected along all the measurement.

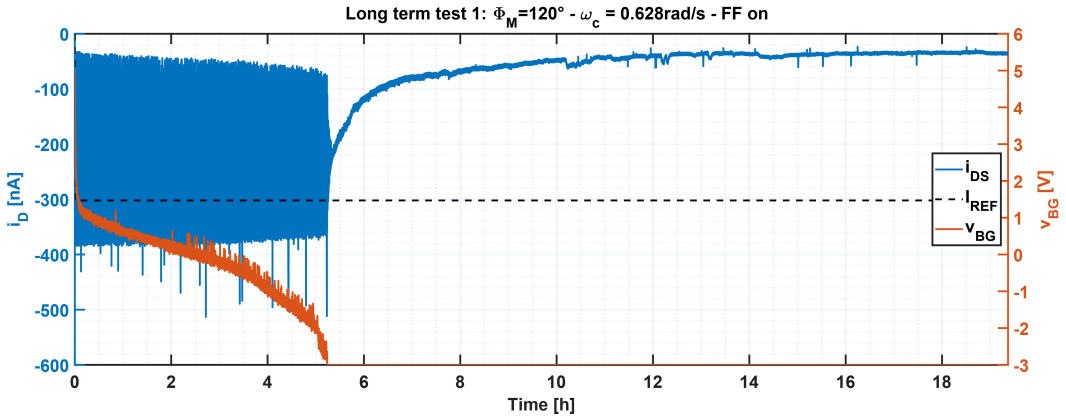

Figure 4.51: *Long term test 1.*

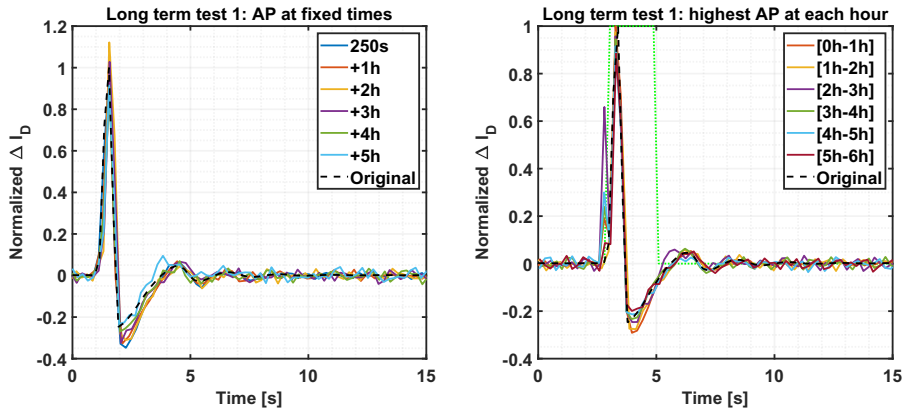

Figure 4.52: *Action potential sensing long term measurement.*

Fig.4.52 shows some relevant results regarding the first 6 hours. On the left, the first AP at $t = 250s$ is normalized w.r.t. its peak, then every APs at each hour are normalized w.r.t. the first one. On the right, are reported the highest action potentials for each time slot of one hour, normalized w.r.t. the first one. The original signal obtained from the simulations is normalized w.r.t. its peak. The shape of the action potential is well-preserved whitin the first 5 hours, except

for some cases in which the detection activated late (e.g. dotted green line in Fig.4.52). This kind of misdetection can be avoided reducing the sampling time or varying the detection threshold. The lowering of the digital control efficiency over time can be related also to the evaporation of de-ionized water solution, which acts as water gate. Different bias points and solutions can be tried to improve the durability of the recording.

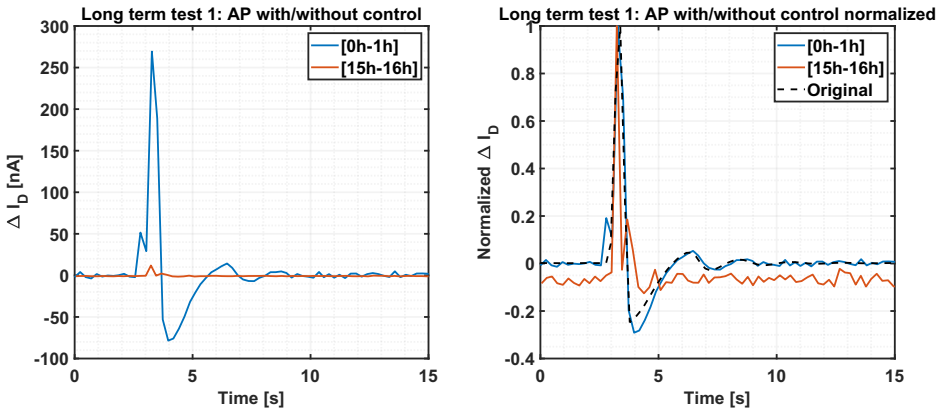

Figure 4.53: *Action potential sensing long term measurement: operative control - control in saturation.*

In Fig.4.53, there is a comparison between an action potential sensed during the first hour and one after 15 hours, when the digital control is stucked in saturation. The shape is no more preserved, however the peak is still detectable, even if the level of the current is so lowered

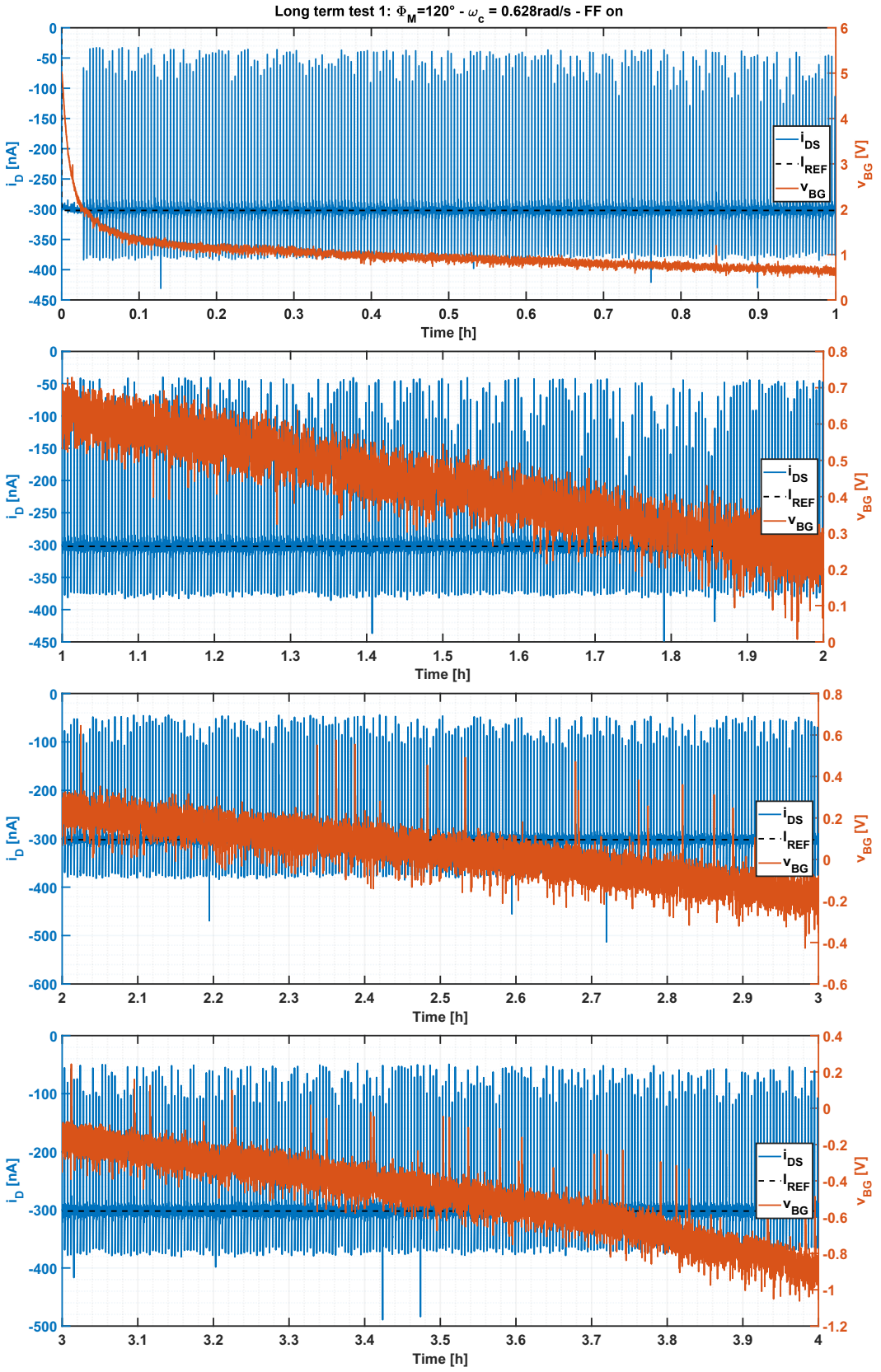

Figure 4.54: *Long term test 1 [0h-4h].*

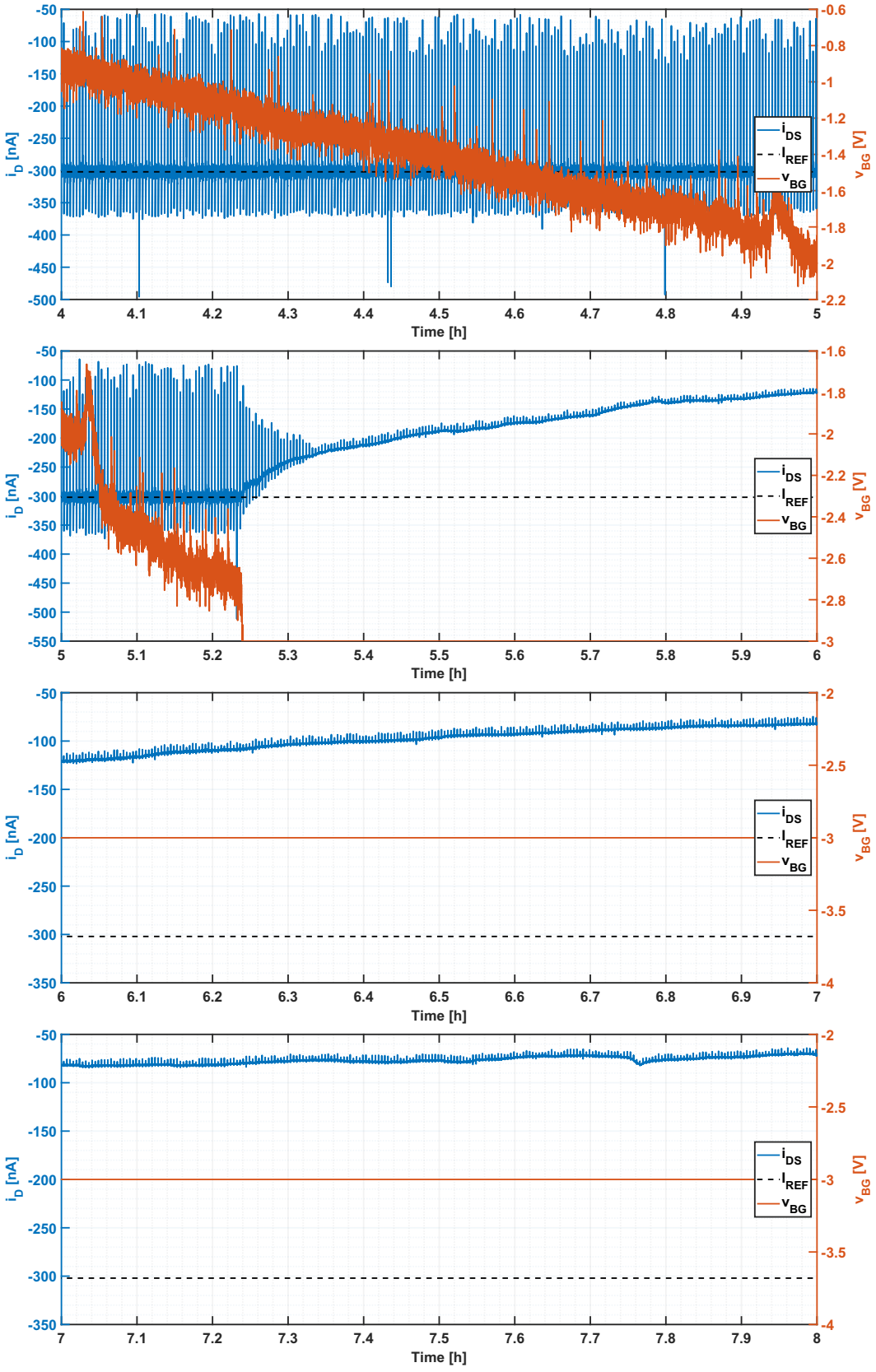

Figure 4.55: *Long term test 1 [4h-8h].*

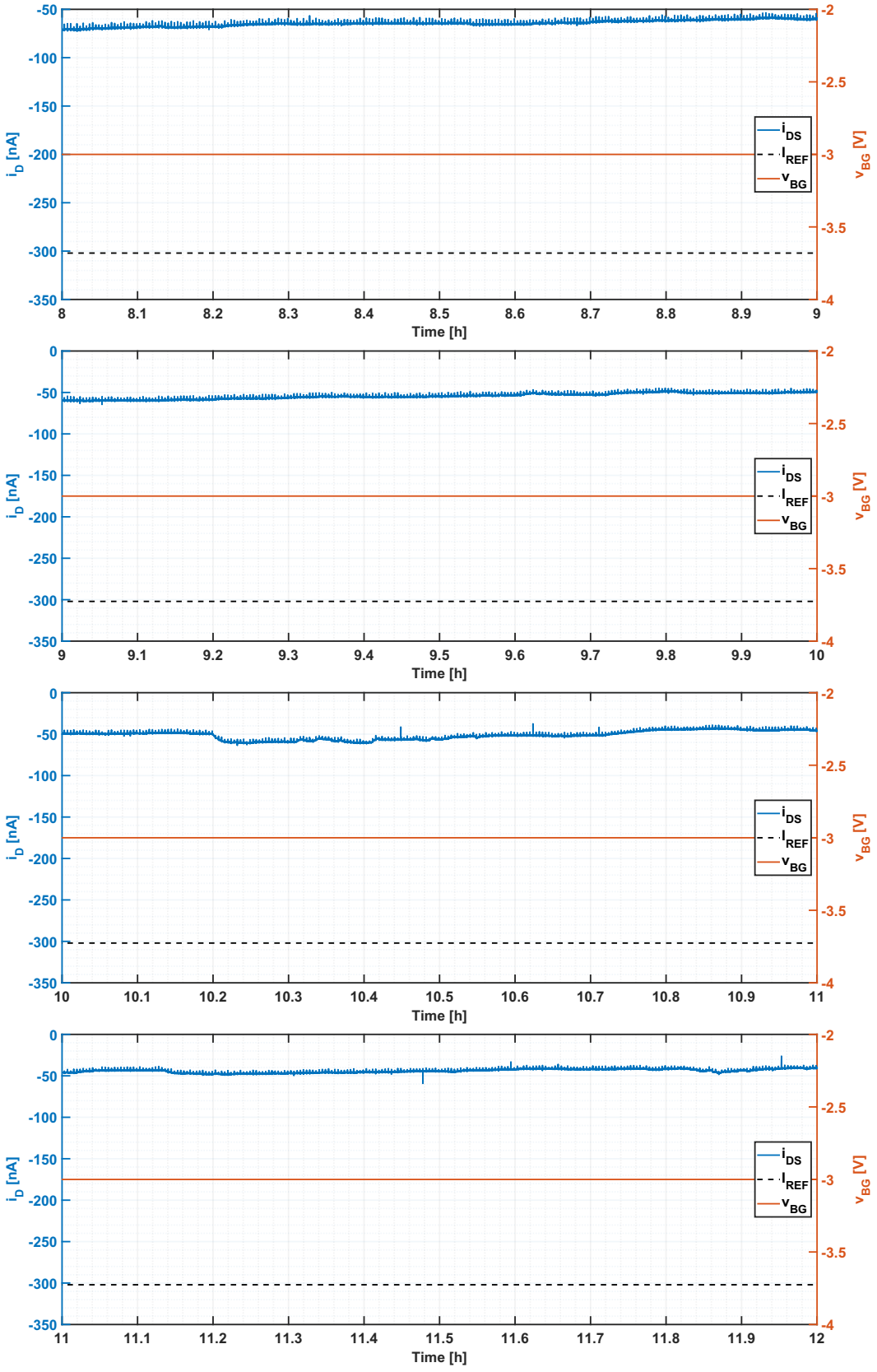

Figure 4.56: *Long term test 1 [8h-12h].*

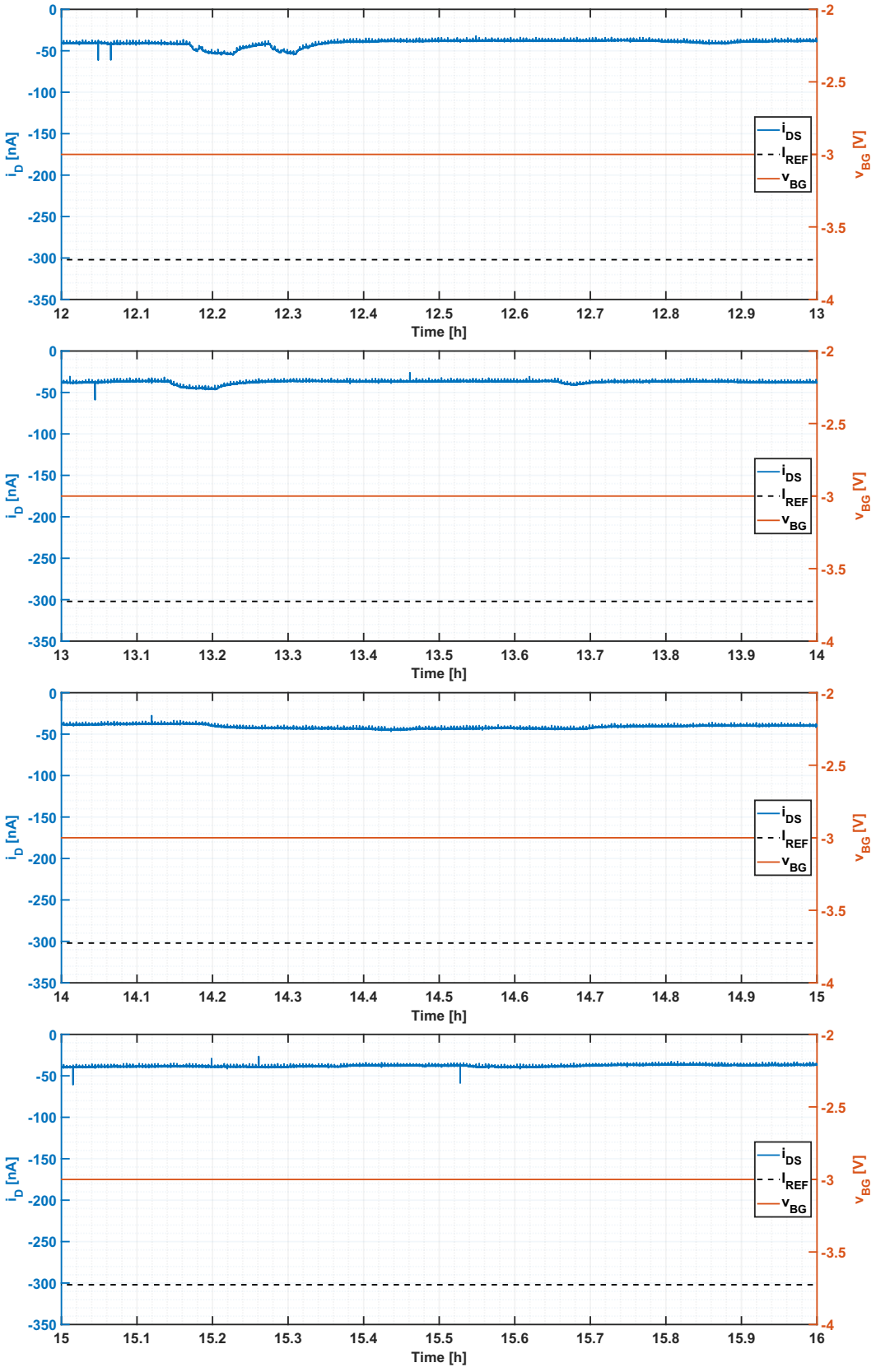

Figure 4.57: *Long term test 1 [12h-16h].*

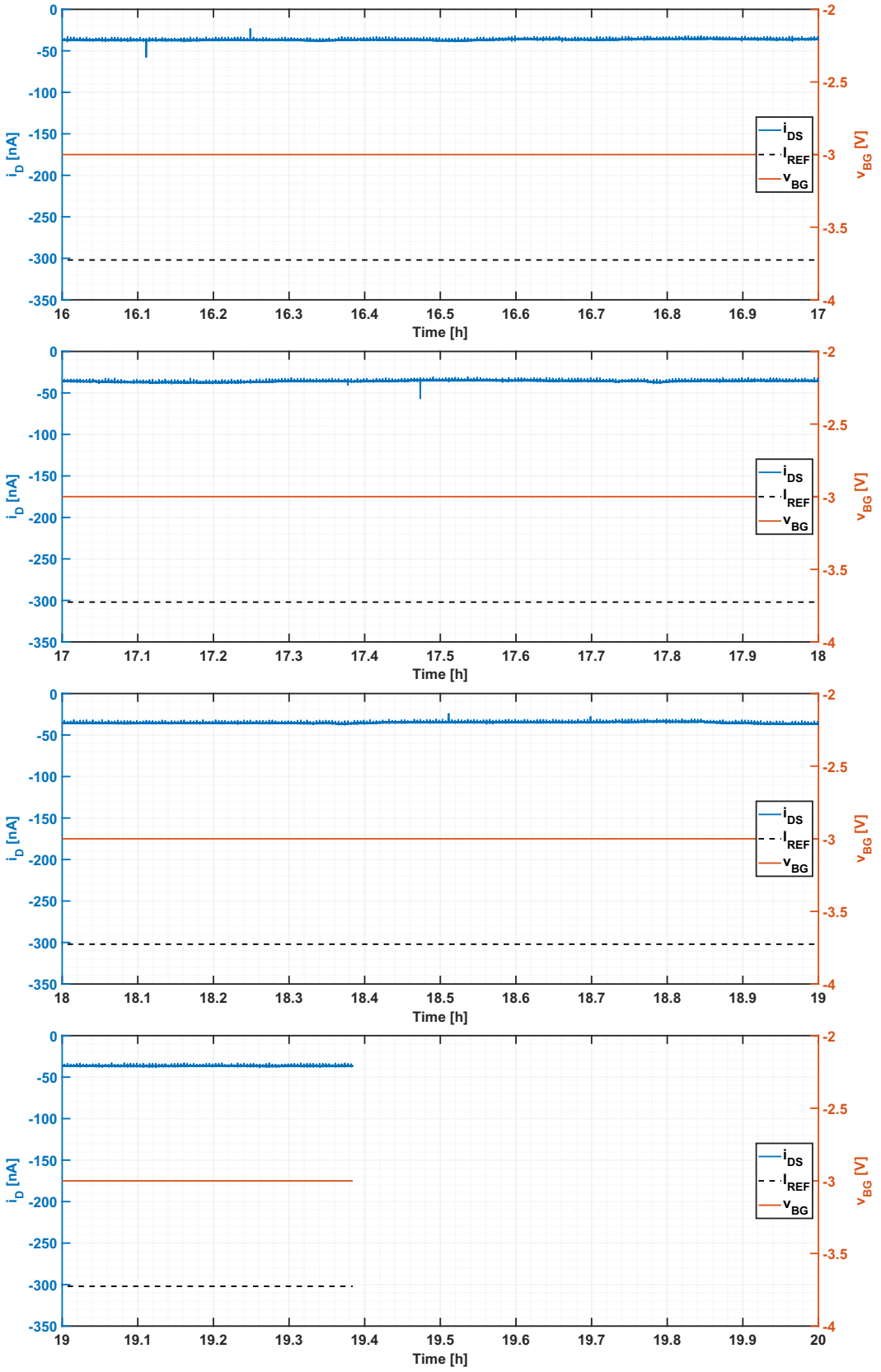

Figure 4.58: *Long term test 1 [16h-20h].*

Chapter 5

Conclusions

In this dissertation we developed a digital control system for dual-gated electrolyte-gated organic field-effect transistor based on PI control with action potential detection and feedforward action, in order to stabilize the device and achieve well-defined output signal (i.e. i_{DS}), preserving and recording the information about an hypothetical extracellular activity. We demonstrated how different configurations of the PI control can successfully remove the current drift, based on the appropriate choice of phase margin and crossing frequency. Specifically, four configurations of Φ_M have been tested: 62°, 90°, 120° and 150°. Experiments without the saturation limit on the derivative of back-gate potential showed almost perfect correspondency between measured data and simulations. With this limitation enabled, in order to prevent any damage to the device, better results have been obtained with $\Phi_M = 120°$. The autotuning method has proven to be effective and essential in order to obtain similar and comparable responses even when measurements were made on different devices and at different times. Three values of crossing frequency have been tried: $0.0628 rad/s$, $0.628 rad/s$ and $6.28 rad/s$. The third one showed better results in terms of settling time and reference tracking. The specific purpose of extracellular recording has been tested with the aid of an arbitrary waveform generator, to create an hypothetical action potential signal to be applied to the top-gate and sensed from the output current. $\omega_c = 0.628 rad/s$ proved to be a good trade-off between disturbance rejection and preservation of the cell signal, demonstrating that with an appropriate frequency analysis, the PI control results reliable itself. With higher crossing frequencies, the action potential detection and feedforward system becomes indispensable to obtain an accurate sensed signal. The detection can be refined with specific current variation thresholds and minimum and maximum detections times, according to the signal of interest. The feedforward action during the detections, based on a linear fit of the control variable trend, has proven effective for the short periods in which it is used. The action potentials recorded with this system

enabled showed no difference between each other at different ω_c. Long term measurements ensured an optimal action potential recording for more than 5 hours. After that, the instant of the peaks can still be detected for over 18 hours, but all the information about the shape is lost. Moreover, different coatings for cell seeding have been tried, in order to analyze their effect on the electrical properties of the devices. Poly-L-lysine showed a drastic loss of EGOFETs performance in terms of threshold voltage shift, as well as not encouraging results for cell seeding. Matrigel treatment did not affected electrical performance of the devices and ensured a good cell coverage of the samples. The coated devices stored in air with extracellular solution showed a field-effect behaviour for approximately one month, with a non monotonous decrease in performances.

5.1 Future perspectives

Several aspects can be further analyzed and tested to improve the performance of the digital control. In particular:

- build up a specific measurement and control set-up with microcontrollers, in order to strongly decrease the sampling time and improve the algorithm performance. This allows also to test the devices with actual living cells, now unfeasible due to the slowness of the instruments;
- implementation of a microfluidic set-up to avoid the evaporation of the liquid gate medium and ensuring the stability (e.g. constant concentration of salts) of the system during long term measurements;
- try different bias point and different electrolytes to find optimal performances;
- try a specifically designed analog or digital filter on the feedback of the PI control, to avoid undesired compensation of the cell signal;
- improve the feedforward action with a more complex predictive control.

Bibliography

[1] A. Poghossian, S. Ingebrandt, A. Offenhäusser, and M.J. Schöning. Field-effect devices for detecting cellular signals. *Seminars in Cell & Developmental Biology*, 20(1):41–48, 2009. ISSN 1084-9521. doi: 10.1016/j.semcdb.2009.01.014. URL https://www.sciencedirect.com/science/article/pii/S1084952109000184. A Special Edition on Biosensors and Development of Pigment Cells and Pigment Patterns.

[2] Muhammad Faisal, Aamer Saeed, Qamar Abbas, Mehar Kazi, Nadir Abbas, Akbar Ali, Dost Khan, and Pervaiz Channar. Thiophene-based molecular and polymeric semiconductors for organic field effect transistors and organic thin film transistors. *Journal of Materials Science: Materials in Electronics*, 29:1–36, 11 2018. doi: 10.1007/s10854-018-9936-9. URL https://doi.org/10.1007/s10854-018-9936-9.

[3] Chang-Hyun Kim, Yvan Bonnassieux, and Gilles Horowitz. Compact dc modeling of organic field-effect transistors: Review and perspectives. *IEEE Transactions on Electron Devices*, 61:278–287, 02 2014. doi: 10.1109/TED.2013.2281054. URL https://doi.org/10.1109/TED.2013.2281054.

[4] Yu Zhang, Jun Li, Rui Li, Dan-Tiberiu Sbircea, Alexander Giovannitti, Junling Xu, Huihua Xu, Guodong Zhou, Liming Bian, Iain McCulloch, and Ni Zhao. Liquid-solid dual-gate organic transistors with tunable threshold voltage for cell sensing. *ACS Applied Materials & Interfaces*, 9 (44):38687–38694, 2017. doi: 10.1021/acsami.7b09384. URL https://doi.org/10.1021/acsami.7b09384. PMID: 29039186.

[5] Loïg Kergoat, Benoit Piro, Magnus Berggren, Gilles Horowitz, and Chau Pham. Advances in organic transistor-based biosensors: From organic electrochemical transistors to electrolyte-gated organic field-effect transistors. *Analytical and bioanalytical chemistry*, 402:1813–26, 09 2011. doi: 10.1007/s00216-011-5363-y. URL https://doi.org/10.1007/s00216-011-5363-y.

[6] Denjung Wang, Vincent Noël, and Benoît Piro. Electrolytic gated organic field-effect transistors for application in biosensors-a review. *Electronics*, 5 (1), 2016. ISSN 2079-9292. doi: 10.3390/electronics5010009. URL https://www.mdpi.com/2079-9292/5/1/9.

[7] Maria Morga, Zbigniew Adamczyk, Sebastian Gödrich, Magdalena Owieja, and Georg Papastavrou. Monolayers of poly-l-lysine on mica electrokinetic characteristics. *Journal of Colloid and Interface Science*, 456:116–124, 2015. ISSN 0021-9797. doi: 10.1016/j.jcis.2015.05.044. URL https://doi.org/10.1016/j.jcis.2015.05.044.

[8] Naomi T. Kohen, Lauren E. Little, and Kevin E. Healy. Characterization of matrigel interfaces during defined human embryonic stem cell culture. *Biointerphases*, 4(4):69–79, 2009. doi: 10.1116/1.3274061. URL https://doi.org/10.1116/1.3274061.

[9] Peter A. Bobbert, Abhinav Sharma, Simon G. J. Mathijssen, Martijn Kemerink, and Dago M. de Leeuw. Operational stability of organic field-effect transistors. *Advanced Materials*, 24(9):1146–1158, 2012. doi: 10.1002/adma.201104580. URL https://onlinelibrary.wiley.com/doi/abs/10.1002/adma.201104580.

[10] Tobias Cramer, Beatrice Chelli, Mauro Murgia, Marianna Barbalinardo, Eva Bystrenova, Dago M. de Leeuw, and Fabio Biscarini. Organic ultrathin film transistors with a liquid gate for extracellular stimulation and recording of electric activity of stem cell-derived neuronal networks. *Phys. Chem. Chem. Phys.*, 15:3897–3905, 2013. doi: 10.1039/C3CP44251A. URL https://doi.org/10.1039/C3CP44251A.

[11] Peng Lin and Feng Yan. Organic thin-film transistors for chemical and biological sensing. *Advanced Materials*, 24(1):34–51, 2012. doi: 10.1002/adma.201103334. URL https://doi.org/10.1002/adma.201103334.

[12] Jonathan Rivnay, Róisín M. Owens, and George G. Malliaras. The rise of organic bioelectronics. *Chemistry of Materials*, 26(1):679–685, 2014. doi: 10.1021/cm4022003. URL https://doi.org/10.1021/cm4022003.

[13] Adrica Kyndiah, Francesca Leonardi, Carolina Tarantino, Tobias Cramer, Ruben Millan-Solsona, Elena Garreta, Núria Montserrat, Marta Mas-Torrent, and Gabriel Gomila. Bioelectronic recordings of cardiomyocytes with accumulation mode electrolyte gated organic field effect transistors. *Biosensors and Bioelectronics*, 150:111844, 2020. ISSN 0956-5663. doi: 10.1016/j.bios.2019.111844. URL https://doi.org/10.1016/j.bios.2019.111844.

[14] Loïg Kergoat, Lars Herlogsson, Daniele Braga, Benoit Piro, Chau Pham, Xavier Crispin, Magnus Berggren, and Gilles Horowitz. A water-gate organic field-effect transistor. *Advanced materials (Deerfield Beach, Fla.)*, 22: 2565–9, 06 2010. doi: 10.1002/adma.200904163. URL https://doi.org/10.1002/adma.200904163.

[15] T. Cramer, A. Kyndiah, M. Murgia, F. Leonardi, S. Casalini, and F. Biscarini. Double layer capacitance measured by organic field effect transistor operated in water. *Applied Physics Letters*, 100(14):143302, 2012. doi: 10.1063/1.3699218. URL https://doi.org/10.1063/1.3699218.

[16] D.A. Bernards and G.G. Malliaras. Steady-state and transient behavior of organic electrochemical transistors. *Advanced Functional Materials*, 17 (17):3538–3544, 2007. doi: 10.1002/adfm.200601239. URL https://doi.org/10.1002/adfm.200601239.

[17] J.P. Colinge. *Silicon-on-Insulator Technology: Materials to VLSI*. Springer, Boston, MA. doi: 10.1007/978-1-4419-9106-5. URL https://doi.org/10.1007/978-1-4419-9106-5.

[18] Deyu Tu, Lars Herlogsson, Loïg Kergoat, Xavier Crispin, Magnus Berggren, and Robert Forchheimer. A static model for electrolyte-gated organic field-effect transistors. *IEEE Transactions on Electron Devices*, 2011. doi: 10.1109/TED.2011.2162648. URL https://doi.org/10.1109/TED.2011.2162648.

[19] T. Cramer, A. Campana, F. Leonardi, S. Casalini, A. Kyndiah, M. Murgia, and F. Biscarini. Water-gated organic field effect transistors opportunities for biochemical sensing and extracellular signal transduction. *J. Mater. Chem. B*, 1:3728–3741, 2013. doi: 10.1039/C3TB20340A. URL http://doi.org/10.1039/C3TB20340A.

[20] Wei Tang, Yukun Huang, Lei Han, Ruili Liu, Yuezeng Su, Xiaojun Guo, and Feng Yan. Recent progress in printable organic field effect transistors. *J. Mater. Chem. C*, 7:790–808, 2019. doi: 10.1039/C8TC05485A. URL http://doi.org/10.1039/C8TC05485A.

[21] Loïg Kergoat, Lars Herlogsson, Benoit Piro, Minh Chau Pham, Gilles Horowitz, Xavier Crispin, and Magnus Berggren. Tuning the threshold voltage in electrolyte-gated organic field-effect transistors. *Proceedings of the National Academy of Sciences*, 109(22):8394–8399, 2012. doi: 10.1073/pnas.1120311109. URL https://www.pnas.org/doi/abs/10.1073/pnas.1120311109.

[22] Saima Hasan, Abbas Z. Kouzani, and M A Parvez Mahmud. Equivalent circuit modeling of a dual-gate graphene fet. *Electronics*, 10(1), 2021. ISSN 2079-9292. doi: 10.3390/electronics10010063. URL https://www.mdpi.com/2079-9292/10/1/63.

[23] Tommaso Salzillo, Francesco D'Amico, Nieves Montes, Raphael Pfattner, and Marta Mas-Torrent. Influence of polymer binder on the performance of dif-tes-adt based organic field effect transistor. *CrystEngComm*, 23: 1043–1051, 2021. doi: 10.1039/D0CE01467B. URL http://doi.org/10.1039/D0CE01467B.

[24] Shingo Iba, Tsuyoshi Sekitani, Yusaku Kato, Takao Someya, Hiroshi Kawaguchi, Makoto Takamiya, Takayasu Sakurai, and Shinichi Takagi. Control of threshold voltage of organic field-effect transistors with double-gate structures. *Applied Physics Letters*, 87(2):023509, 2005. doi: 10.1063/1.1995958. URL https://doi.org/10.1063/1.1995958.

[25] Q. Zhang, F. Leonardi, S. Casalini, I. Temiño, and M. Mas-Torrent. High performing solution-coated electrolyte-gated organic field-effect transistors for aqueous media operation. *Scientific Reports*, 2016. doi: 10.1038/srep39623. URL https://doi.org/10.1038/srep39623.

[26] Alberto Leva, Chris Cox, and Antonio Ruano. *Hands-on PID autotuning: a guide to better utilisation*. 01 2002.

[27] Sang-Hoon Kim. *Electric Motor Control - Chapter 2 - Control of direct current motors*. Elsevier, 2017. doi: 10.1016/B978-0-12-812138-2.00002-7. URL https://doi.org/10.1016/B978-0-12-812138-2.00002-7.

[28] T. Moir. *Feedback*. Springer, Cham. doi: 10.1007/978-3-030-34839-7. URL https://doi.org/10.1007/978-3-030-34839-7.

[29] Alessandra Galli, Nicolò Lago, Sarah Tonello, Mario Bortolozzi, Marco Buonomo, Morten Gram Pedersen, Andrea Cester, and Giada Giorgi. A morphological peak-detector for single-unit neural recording acquisition systems. *IEEE Transactions on Instrumentation and Measurement*, 71: 1–11, 2022. doi: 10.1109/TIM.2022.3157006. URL https://doi.org/10.1109/TIM.2022.3157006.

[30] Nurettin Acr, Ibrahim Oztura, Mehmet Kuntalp, Bari Baklan, and Cüneyt Güzeli. Automatic detection of epileptiform events in eeg by a three-stage procedure based on artificial neural networks. *IEEE transactions on biomedical engineering*, 52:30–40, 02 2005. doi: 10.1109/TBME.2004.839630. URL https://doi.org/10.1109/TBME.2004.839630.

[31] Nguyen Thi Dao, Linh-Trung Nguyen, Ly Nguyen, Duc-Tan Tran, Hoang-Anh Nguyen, and Boualem Boashash. A multistage system for automatic detection of epileptic spikes. *REV Journal on Electronics and Communications*, 8, 03 2018. doi: 10.21553/rev-jec.166. URL `https://doi.org/10.21553/rev-jec.166`.

[32] A. Cester. *Dispense di Elettronica Organica e Molecolare*.